Sputtering of Indium under polyatomic ion bombardment

Dissertation
for the degree
of Dr. rer. nat.

Presented to the
Department of Physics,
University of Duisburg-Essen

by
Andrey V. Samartsev
from Tashkent, Uzbekistan

October 2004

1. Referee: Prof. Dr. A. Wucher
2. Referee: Prof. Dr. M. Schleberger

Public defence held on: 21 December 2004

CONTENTS 4

INTRODUCTION

INTRODUCTION

If a beam of energetic ions irradiate a solid, several processes are initiated in the area of interaction. A fraction of ions could be backscattered from surface layers, others are slowed down in the solid and may be trapped or may diffuse to the surface or into the bulk. Atoms of the solid can be ejected from surface separately or as conglomerates. This process is called sputtering. During the ejection process, a fraction of these sputtered particles is getting charged. A sputter event initiated by a single bombarding particle is a priory statistical in nature. However, in experimental conditions, when bombarding with a great number of particles (ion beam) integral parameters are used. The key parameter characterising sputtering is the so-called "yield" Y_{tot}, i.e., the mean number of target atoms sputtered per impinging particle. Total sputtering yield Y_{tot} may be presented as the sum of partial yields Y_X for different projectiles X (atoms, molecules, and clusters) emitted during the sputtering, which is the average quantity of sputtered particles of certain type per impinging ion.

Sputtering phenomena of single-element metals can be described by elastic-collision cascades initiated by the incident particles in the surface layers. For multicomponent solids and non-metals and/or bombardment with ions which react chemically with the atoms of a solid sputtering is influenced by several additional processes. [Be81]

Sputtering was first discovered in electric gas discharges more than 150 years ago. Cathode material was observed to be deposited on the surrounding glass walls, thus the name cathode sputtering can be still found in the literature. Fifty years later the physical process of the sputtering through atomic bombardment was discussed [Ko02]

In the flux of sputtered particles, besides single atoms, multiatomic structures, so-called „clusters", are presented. Most early cluster-emission studies were performed on silver: Honig [Ho58] first observed dimer clusters in the mass spectrum of positive ions. Katakuse et al [Ka86] found Ag_n^+ clusters up to n = 200 (>20000 amu) from polycrystalline silver bombarded with 10 keV Xe^+.

In addition, strong oscillatory behaviour in the abundance distribution was observed for clusters up to Ag_{30}^+, the odd numbers being significantly more intense than the even ones. Referring to Dörnenburg et al. [Do61], Hortig and Müller gave an interpretation in terms of binding-electron parity. Because of spin–pairing of binding electrons, clusters with an even number of valence electrons posses an increased stability, which is enhanced both with respect to fragmentation and ionization. Therefore, clusters containing an even number of binding electrons show both an enhanced dissociation energy and larger ionization potential.

From a clean metal surface the majority of the particles leave the surface as neutral ones. Part of them is ionized in the emission process. These particles called secondary ions. Secondary ion emission phenomena characterized by a (partial) secondary ion yield $Y_X^{\pm}$ which is the mean number of certain ions X per projectile. Secondary ion yield $Y_X^{\pm}$ depends on the sputtering yield Y_X and ionization probability $\alpha^{\pm}$ which is, basically, efficiency of the ionization and determined as following ratio:

$$\alpha_X^{\pm} = \frac{Y_X^{\pm}}{Y_X}$$

where Y_X is a partial yield of particles.

Ionization probability is varying for different materials and different clusters [He99]. In order to measure the ionization probability it is necessary to know quantitative information about the flux of sputtered neutrals. For this purpose one can use different post-ionization techniques. At the beginning of Secondary Neutral Mass-spectrometry (SNMS) electron-impact ionization technique was used [Oe74], [Oe78], [Gn89]. SNMS with electron impact ionization may be divided into two experimental techniques: electron beam SNMS and electron gas SNMS. Electron beam SNMS was suffering mainly from two drawbacks: low ionization efficiency and background from residual gas ions. Better results were achieved using electron gas SNMS. In this technique postionization is performed by electron impact ionization in a dense and "hot" electron gas. In the respective SNMS-instruments, such an electron gas with electron temperatures T_e corresponding to about 10 eV is provided by the electron component of low pressure r.f. plasma maintained mainly in Argon by a specific electrodynamics resonance effect. The postionization probability for a neutral sputtered particle entering the postionization region with energies in the order of a few eV is as high as several 10^{-2}, i.e. by a few orders of magnitude above that achieved with electron beam arrangements used for the same purposes. In the experiments using SNMS with electron impact metallic clusters with nuclearity up to 4 were detected [Oe90].
Later on post-ionization technique utilizing intense laser beams was developed [Be84], [Yo87], [Pa88], [Co91], [Co93], [Co94], [Wu93a], [Wu93b] and [He98]. Using this SNMS technique relative cluster distributions and their kinetic energy spectra were determined. Advantage of the laser post-ionization is the significantly higher efficiency of ionization of sputtered particles and therefore very efficient use is made of the sputtered material. For quantitative measurements, one can introduce the useful yield Y_u as that fraction of the sputtered neutral particles which is actually detected as postionized ions. While electron gas and -beam postionization are typically characterized by Y_u values ranging from 10^{-9} (quadrupole instruments) to 10^{-7} (magnetic sector instrument), this value may be higher than 10^{-3} [Pe03].
Additional information about sputtering at microscopic level can be delivered by computer simulations described in chapter 2.2.
Besides experimental works there were theoretical investigations to describe the sputtering process. Several models have been proposed up to now.
Sputtering of atoms from a clean metal can be well described by so-called linear collision-cascade model [Si81a], while this model is insufficient to predict the abundance of large neutral clusters. There are several other models which can describe cluster yield in dependence on the cluster size for some experimental conditions [Li83], [Si81], [Ur88], [Ur81], Jo[71], Bi[78], [Bi80]. At present, there is no model among them which can realistically explain emission of the clusters for a variety primary ion – target combinations in a wide range of energies.
From experimental point of view, a new approach to this problem is a study of emission characteristics under bombardment by polyatomic projectiles.
While in some range of energies and masses of primary projectile and target atoms the sputtering process may be well described by linear collision cascade model, sputtering of the solid with a polyatomic projectile having the same velocity the sputtering yield may deviate from the sum of the yields of individual atoms. This effect is generally called non-additivity of the sputtering process. Non-additivity of the sputtering yield is related to the non-linearity of the sputtering process. Non-additivity nearly always manifests itself as enhanced yields.
For quantitative determination of the enhancement such parameters as factor of non-additivity (enhancement) can be introduced which is basically ratio of partial sputtering yields per atom in the polyatomic projectile and under single impinging atom.

Experimental result on non-additive enhancement of sputtering yield per atom in the impinging atom at the same velocity was received by Andersen and Bay [An73], [An74], [An75] and also by Thompson and Johar [Jo79], [Th79], [Th80]. In these works nonlinear effect of the sputtering was discovered. The sputtering yield produced by two atomic impinging particles was smaller in comparison with dimer bombardment at the same velocity.

When polyatomic ion penetrates the surface collision cascades produced by separate atoms are overlapping due to the fact that the lateral size of cascades is exceeding the distance between atoms in the primary ion. From computer simulation we know that the lateral size of a cascade is several nm and time of its evolution is of the order of picoseconds. To reach the condition of overlapping cascades produced by different impinging atoms using monoatomic ion bombardment one would have to use primary ion current density of the order of 1000 A/cm^2. Such high ion current density is practically hardly achievable.

The interesting question how the cascade overlapping under polyatomic ion bombardment changes the sputtering process compared to one produced by single atomic ion impact. Qualitative changes of the sputtering process occurring within volume affected by polyatomic ion impact should lead to non-additive changes in the sputtering yield, cluster abundance, and other parameters of sputtered particles compared to the atomic bombardment with the same velocity. Condition of the constant velocity is derived from the fact that for the measurements of non-additive effect in the sputtering process all experimental parameters must be equal for atomic and polyatomic ion bombardment except nuclearity of the projectile.

Most of the works related to the mass distribution of species sputtered by polyatomic ion impact were considering secondary ions [Th81], [Be98a], [Be98c]. Comparison of Ta_n^+ an Nb_n^+ cluster emission under atomic and polyatomic Au_m^- (m = 1-3) with a kinetic impact energy of 6 keV per constituent atom showed relatively high enhancement of the ionic yield for large cluster ions [Be98b], [Be00]. For example, enhancement for a cluster consisting of 10 atoms was at the value of two orders of magnitude.

But this data can be hardly interpreted for findings how the mechanism of cluster emission changes since for emission of secondary ions the complex process of ionization play a dominant role. Up to now, the ionization mechanism of sputtered clusters is not understood, and hence the secondary ion yields cannot be regarded as representative of partial sputtering yields.

Changes in the mass distribution and yield the sputtered of neutrals under polyatomic irradiation was investigated by Heinrich et al. who measured self-sputtering of silver under bombardment with Ag_m^+ (m=1÷3) projectiles[He00], [He02]. For production of primary ions Heinrich used self-built cluster ion source. In the ion source polyatomic projectiles were created using ablation process induced by bombarding the surface with an intense UV laser pulse. Relative intensity of the projectiles delivered by an ion source was by factors of 170, 29 and 12 for Ag_1^+, Ag_2^+ and Ag_3^+ respectively. It was possible to operate this ion source only in the pulsing mode.

Sputtered species from investigated surface were post-ionized prior to mass-spectrometry by means of single photon ionization. Obtained results show that the cluster abundance of sputtered neutral clusters was changing in dependence on the nuclearity of the projectile. In contrast to the results on emission of secondary ions under polyatomic impact [Be98b], [Be00], results of Heinrich et al. [He02] show that the nuclearity of the projectile seems to be of rather minor importance with respect to the abundance distribution of sputtered neutral silver clusters. Comparing, for instance, the relative signal of Ag_9 with that measured for sputtered Ag monomers, similar ratios of 0.003, 0.006 and 0.003 were found for mono-, di- and tri-atomic projectile bombardment. The temporal width of the

projectile ion pulses was depending on the ablation laser intensity, extracting voltage for projectiles and their mass. Largest duration of projectile ion pulse was less than 2 μs and due to the fact that minimal duration of the primary ion pulse in order to fill ionizing volume above investigated sample with sputtered species of all velocities is about 5 μs Heinrich had to take a sum of spectra measured at the different time delays (chapter 5.9)

Nonlinearity of the sputtering must manifest itself in the creation of „spikes". Sputtering from „spike" must first of all be reflected in the changes of the velocity distributions of sputtered neutrals. Unfortunately, using the ablation cluster ion source Heinrich could not measure velocity distributions. The first reason was that the dynamic range of the signal was not sufficient to measure velocity distributions and second one that it ultimately requires short projectile pulses with a temporal duration of about 100 ns, which could not be delivered with the cluster ion source operated in ablation mode.

The main purpose of this work is get new information about nonlinearity of the sputtering under polyatomic ion bombardment using time-of-flight neutral mass spectrometry.

It is very desirable to extend data about mass distribution of sputtered species for different materials.

To achieve better flexibility in the experiment using polyatomic ion bombardment in order to create primary projectiles another technique instead of ablation must be used. Ion source must be able to be operated in the continuous mode (DC current) and there must be possibility to produce projectiles of different elements and nuclearity.

For this purpose negative sputter ion source could be well suitable to approach the requirements stated above. Sputter negative ion source for SNMS experimental setup was developed.

Comparing the secondary ion yields with those of the corresponding neutrals, it is possible to determine ionization probabilities in dependence on the nuclearity of the projectile. There are is data of this kind measured up to now. On the other hand polyatomic ions began to be intensively used impinging projectiles in the routine SIMS surface analysis where the ionization factor is crucial [Gi00], and these measurements could by of interest for development of SIMS technique. Understanding of the ionization process is of great physical importance and additional experimental studies are very desirable.

1 Fundamentals of sputtering.

Sputtering is the process of destruction of solid state under irradiation by energetic ions leading to the emission of atomic, molecular and cluster particles. The main characteristic parameter of sputtering is the sputtering Y yield depends on the atomic number Z_1 of projectile, atomic number Z_2 of target atoms, impinging energy E_p, angle of impinging φ_0, bonding state of the target material.

At the moment there are more than 10 thousands publications devoted to the problem of sputtering. This data is summarized in a number reviews and manuscripts [Be81], [Be91].

Kelly [Ke84] has proposed a classification of different mechanisms of sputtering which could be characterized by the time of particle interaction. Single knock-on sputtering process occurs when atom from the first monolayers of the target getting momentum directed away from surface during few collisions is occurring at the times 10^{-14} sec. Collision cascades deeply in the bulk resulting in the sputtering of recoils can be evolving

up to the times 10^{-13}-10^{-12}. At the longer times up to 10^{-11} sec. collisional spikes are evolving. Spike is the region where a very dense collision cascade is propagating.
Single knockon mode of the sputtering is shown on fig. 1.1 a). Linear collision cascade of binary collisions is shown on fig. 1.1 b)

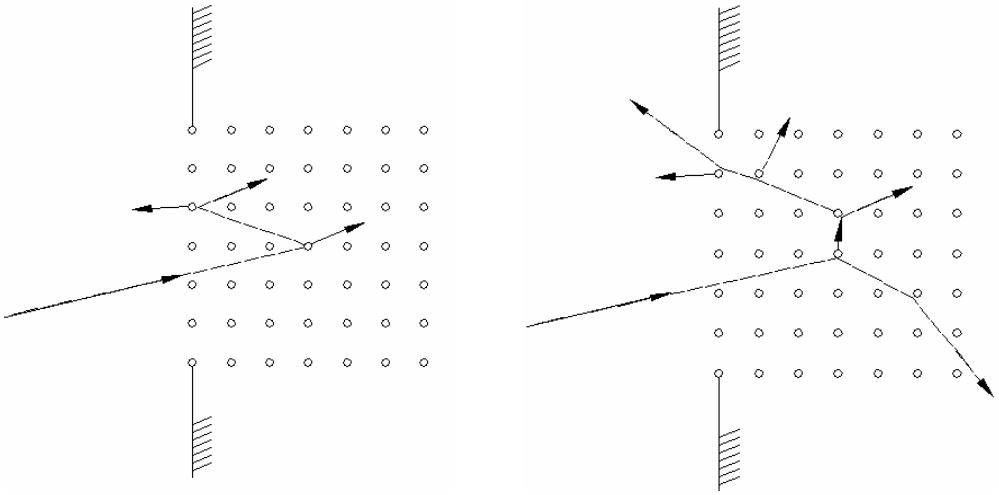

a) **b)**

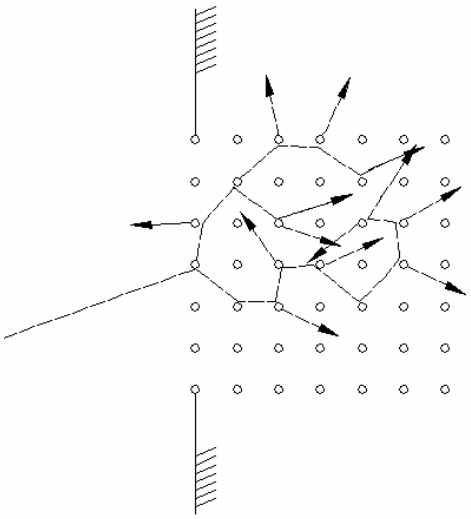

c)

Three sputtering modes of solid state by elastic collisions:

a) Single knockon mode
b) Linear collision cascade
c) Collisional spike

Fig. 1.1 Sputtering of solid state in different modes of energy deposition by elastic collisions (After [Be81]).

When energetic ion is penetrating the surface it makes collisions with atoms of the target. Some of these atoms, which are called „recoils“, get momentum and collide with other atoms of the target. Therefore, collision cascade is developing. Some of these recoils can get momentum directed away from surface. In addition to that, some of recoils moving in the bulk of the target can lose their energy and at some point stop. As result of these collisions vacancies or interstitial atoms (radiation defects) are created, also atoms can change their original order in the lattice (atomic mixing). Impinging ion can stop it the bulk and ion implantation is produced. Later, due to the erosion of the solid under sputtering this ion can be resputtered.

Sputtering is the complex process including multiatomic collisions (cascades), initiated by primary ion.
An atomic collision process involving two atomic particles (projectile and target) can be characterized by a cross section σ. Therefore, the average number of projectiles from primary beam undergoing the collisions is given by $Nx\sigma$, where x is a thickness of the target and N is the number density of atoms in the target. There are must be considered cross sections of elastic collisions in which kinetic energy is transferred from projectile to target atom and cross sections for electronic excitation and/or ionization.
Cross sections for elastic collisions are conveniently specified in terms of differential cross section

$$d\sigma(E,T) = \frac{d\sigma}{dT} dT$$

where E is the initial and T the transferred energy in a single collision.
For Rutherford scattering, i.e., for energies high enough so that scattering is determined by the Coulomb repulsion between the nuclei, one finds

$$d\sigma(E,T) = \pi \frac{M_1}{M_2} Z_1^2 Z_2^2 e^4 \frac{dT}{ET^2}$$

Where $Z_1 e$ and $Z_2 e$ are the nuclear charges of projectile and target atoms.
This cross section is valid only for $\varepsilon >> 1$, where

$$\varepsilon = \frac{M_2 E}{M_1 + M_2} * \frac{a}{Z_1 Z_2 e^2}$$

and $a \cong 0.885 a_0 \left(Z_1^{2/3} + Z_2^{2/3}\right)^{-1/2}$; $a_0 = 0.529\,\mathring{A}$ is the screening radius. Energy of projectile must be high enough so that the nuclei approach closer to each other than the screening radius a. For lower energies $\varepsilon \le 1$, the screening of the Coulomb interaction is essential and potential describing the scattering event becomes more complex.
In this regime, the cross section can be approximated by the expression

$$d\sigma(E,T) \cong C_m E^{-m} T^{-1-m} dT \qquad (1.1)$$

with

$$C_m = \frac{\pi}{2} \lambda_m a^2 \left(\frac{M_1}{M_2}\right)^m \left(\frac{2 Z_1 Z_2 e^2}{a}\right)^{2m}$$

λ_m being dimensionless function of the parameter m which varies slowly from $m = 1$ at high energies down to $m \approx 0$ at very low energies. Expression 1.1 is based on the so-called Thomas-Fermi model of atomic interaction with the potential of the form $V(r) \propto r^{1/m}$.
An important quantity in the study of the interactions of energetic ions with solids is the stopping power $S(E)$, a measure of the energy loss per unit distance traveled dx of the ion moving through the solid target of atomic number density N :

$$\frac{dE}{dx} = -NS(E)$$

The total stopping cross-section, $S(E)$, is usually split into two components, the nuclear stopping cross-section $S_n(E)$ — the elastic component and electronic stopping cross-section $S_e(N)$ mostly of inelastic energy loss.

The nuclear energy loss is treated independently of the electronic energy loss because at high velocities $(\varepsilon >> 1)$ the latter dominates the deceleration of the ion, while at lower energies S_n is the cross-section that is of interest in sputtering.

The nuclear stopping power S_n is the average energy transferred in elastic collisions when summed over all impact parameters.

$$S_n(E) = \int_0^\infty T \cdot d\sigma(E,T)$$

The nuclear stopping power then depends on the atomic model used to describe the interaction, and in particular on the form adopted for the screened Coulomb interaction.

$$S_n(E) = \frac{1}{1-m} C_m \gamma^{1-m} E^{1-2m} \qquad (1.2)$$

It is seen that $S_n(E)$ rises approximately proportional to E at low energies $(m \cong 0)$, approaches a plateau at intermediate energies $(m \cong 0.5)$ and falls of at higher energies $(0.5 < m \le 1)$.

This equation can be written in a more compact form

$$S_n(E) = 4\pi a Z_1 Z_2 e^2 \frac{M_1}{M_1 + M_2} s_n(\varepsilon) \qquad (1.3)$$

where $s_n(\varepsilon)$ is a universal function depending on the detailed form adopted for the screened Coulomb interaction. There are several forms of this function for different screening approximations [Be81].

The most authoritative theoretical study of sputtering was done in 1969 by Sigmund [Si69]. In this theoretical study, an integrodifferential equation was developed for the sputtering yield, based on an approximation to the solution of the linearized Boltzmann transport equation.

Sigmund based his theory on the fundamental assumptions that the (monoatomic) target medium be isotropic and homogeneous, so that the transport of particles can be described by Boltzmann's equation, and on an isotropic distribution of the particle velocities. The medium is assumed to be semi-infinite, with a planar surface. Along the way, Sigmund uses also assumption that the collisions are binary and dilute. For dilute cascades, i.e. where only a small fraction of atoms is moving, Boltzman transport equation can be linearized and analytical solution may be derived.

The main conclusion from the theory of linear cascades that sputtering is proportional to the energy deposited near the surface by incoming ion, so that his formula for backward sputtering is of the general form

$$Y_{lin}(E) = \Lambda F_D(E) \qquad (1.3)$$

where F_D is the density of deposited energy at the surface in units of $eV/\mathring{A}$, given by

$$F_D(E) = \alpha N S_n(E) \qquad (1.4)$$

Here α is a dimensionless, energy independent function of the mass ratio M_2/M_1 (masses of projectile and target atoms), the angle of incidence θ_0 and the primary energy of the ion E, S_n is determined as Eq. (1.3).
Parameter Λ is the constant containing specific material properties and determined as

$$\Lambda = \frac{\Gamma_m}{8(1-2m)} \frac{1}{N C_m U^{1-2m}} \qquad (1.5)$$

Where Γ_m is parameter depending on m, U is a planar surface barrier, N is the number density of atoms in the bulk, m and C_m are cross section parameters.
Equations (1.3)-(1.5) have undergone extensive experimental testing. Good agreement with experimental results was found (Fig. 1.2)

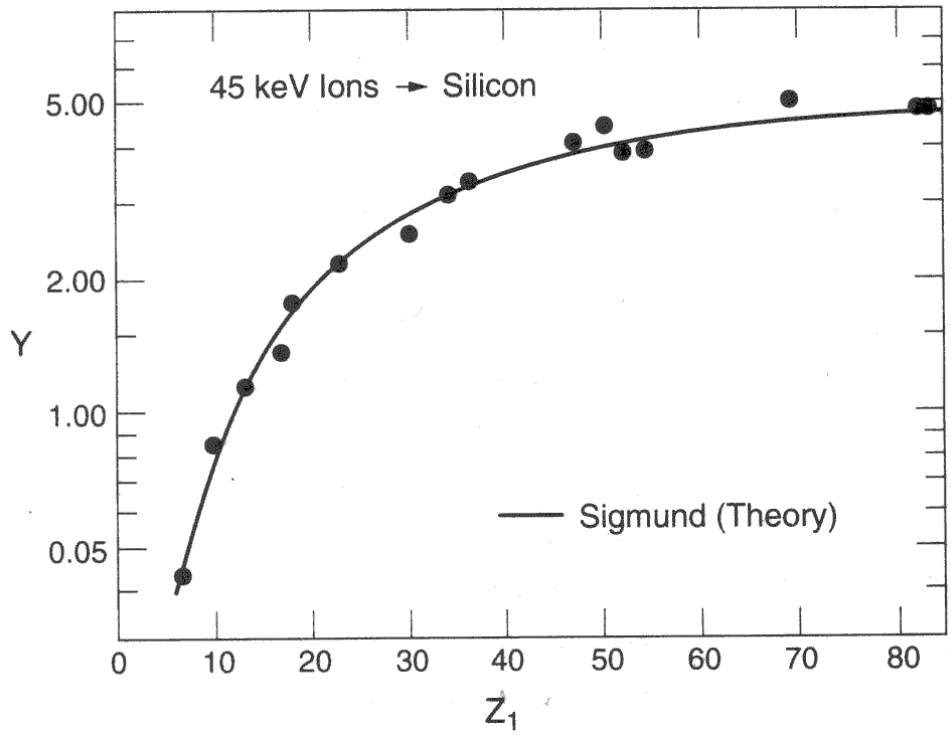

Fig1.2
Incident ion dependence of the Is sputtering yield at 45 keV energy. The solid line represents the calculations of Sigmund [Si81], and the data are from Andersen & Bay [An81]

When the planar binding model is used, sputtered atoms lose energy U_s in passing the binding barrier and, since this energy comes entirely from the velocity component normal to the target surface, refraction is occurring as well.
The energy and direction of sputtered atom are

$$E = E_0 - U_s$$

cosine of angle between the surface normal and atom's velocity μ is

$$\cos(\theta) = \sqrt{\frac{E_0 \mu_0^2 - U_s}{E_0 - U_s}}$$

Here subscript 0 denotes values before passing the barrier.
If the particle flux incident on the bombarding barrier is isotropic and follows an E_0^{-2} energy spectrum, the sputtered atoms are distributed as

$$\rho(E,\mu) \propto \cos(\theta) \cdot \frac{E}{(E+U_s)^3} \qquad (1.6)$$

Where U_s is the surface binding Energy. Equation (1.6) is the familiar Thompson model (Th68): it has maximum at $U_s/2$; the sputtered flux is isotropic (factor μ is just its projection onto the barrier).
Equation (1.6) was generalized by Sigmund (Si81). Sigmund retained the isotropic flux incident on the barrier, but replaced the energy dependence with the $E^{-2(1-m)}$ spectrum and got an equation

$$Y(\theta,E) \cdot d^2\Omega \cdot dE = \left[\frac{E}{(E+U_s)^{3-2m}} \right] \cdot \cos(\theta) \cdot d^2\Omega \cdot dE \qquad 1.7$$

Where E and θ are the ejection energy and angle against the surface.
Once the majority of atoms in a certain volume are set in motion sputtering mode transforms to the spike regime (fig.1.1c). The energy must dissipate in manner quite different from that which is found for linear collision cascades. While there is fairly general agreement on the qualitative criteria for the significance of spike effects in collision cascades, there is considerable uncertainty as to the mechanism of energy transport in a spike, as well as to the theoretical evaluation of sputtering yields under spike conditions.
One of the ideas in modeling of the sputtering from a spike – is the conception of thermal spike. In the models based on this idea there is considered evaporation of target material from a microscopically small region with a high local temperature due to individual ion impact. There is considerable uncertainty as to the mechanisms of the energy transport in a spike and to the theoretical evaluation of sputtering yields under spike conditions. Several thermal spike models of sputtering [Si75], [Cl80], [Cl81], [Sz82], [Ke90].
Well known thermal spike model of Sigmund-Clausen [Cl80] will be considered here shortly. The model is based on simple geometry of cylindrical spike of initial width $\left\langle \rho_0^2 \right\rangle^{1/2}$ intersecting the target surface at right angle. Inside the spike region is a dense gas

characterized by some temperature $T(\rho,t)$ depending on the time t and distance ρ from trajectory. Energy transport inside the spike is determined by the equation of heat conduction

$$\frac{dT}{dt} = \nabla \cdot [\kappa(T) \nabla T]$$

This can be readily solved for cylindrical symmetry.
Thermal diffusivity is taken as

$$\kappa = \frac{25}{48} \frac{1}{N \lambda_0 a^2} \left(\frac{kT}{\pi M} \right)^{1/2}$$

where N is the number density of target atoms, M their mass and k Boltzmann's constant; $\lambda_0 \cong 24$ and $a \cong 0.219$ $\overset{o}{\text{A}}$ are Born-Meyer constants.
With the normalization

$$\frac{3}{2} Nk \int d\rho^2 \cdot T(\rho,t) = F_D^{*\prime}$$

where F_D^* is the energy deposited per unit track length is found

$$T(\rho,t) = t^{-2/3} \left[A - \rho^2 / 12 \cdot \chi \cdot t^{2/3} \right]^2 \qquad (1.8)$$

for values of ρ where function in brackets is positive, and zero, otherwise. Here, $\chi = k \cdot T^{-1/2}$ and $A = \left(F_D^* / 6\pi\chi Nk \right)^{1/3}$
Evaluation of the sputtering yield

$$Y = \int_{t_0}^{\infty} dt \int_0^{\infty} \pi d\rho^2 \Phi(T(\rho,t)) \qquad (1.9)$$

For an ideal gas confined by a planar surface potential U, the evaporation rate at constant density is given by

$$\Phi(T) = N(kT / 2\pi M)^{1/2} \exp(-U / kT) \qquad (1.10)$$

as follows directly from Maxwell-Boltzmann law.
Inserting Eq. (1.10) and (1.8) into (1.9) and after integration yields an expression for the thermal sputtering yield:

$$Y_{th} = 0.0360 \left(\lambda_0 a^2 F_D^{*2} / U^2 \right) g(-U / kT_0) \qquad (1.11)$$

with a function $g(\xi) = (1 + \xi - \xi^2) \exp(-\xi) + \xi^3 \int_{\xi}^{\infty} dt \cdot e^{-t} / t$

Equation 1.11 can be compared with sputtering yield for linear cascade (1.3).
The following observation may be made:

(i) while Y_{lin} is proportional with the deposited energy F_D, Y_{th} varies more rapidly than proportional to $\left(F_D\right)^2$.

(ii) The relative significance of thermal and linear sputtering increases with increasing ratio of deposited energy and binding energy.

(iii) For bombardment with an n-atomic projectile, Y_{th} increases faster than n^2, while Y_{lin} is proportional to n at constant ion velocity.

Urbassek and Michl have proposed a gas flow model of sputtering from the spike [Ur86]. In this model it assumed that part of solid inside of the spike has received enough energy to bring it above critical point and gasified. In that gaseous state, the volume is free to flow into the vacuum. There is more detailed description of this model in chapter 10.3.
Single knock-on regime of the sputtering is mostly considered for the sputtering by light particles, when the scattering of primary ion near the target surface becomes quite probable fig. 1.1a). This mode is evidently part of the linear cascade regime but it is not well described by the conventional solution of the Boltzmann equation [Si69]. This is due assumption made in the theory that presence of the surface do not exert an important influence on the development of collision cascades.
In other cases, for instance, for alkali halide crystals other mechanisms like Coulomb interaction and electronic excitation may play dominant role in the sputtering.

2. Atomic and cluster emission during sputtering.

2.1 Experimental observation of the cluster emission

The emission of clusters from solid surfaces was discovered about 60 years ago [Ha42], [Ma43]. This was in an RF-spark between carbon electrodes, and hence clusters originated from sublimation. In the fifties, Honig [Ho53] continued this work and performed fundamental research on thermal emission from group IV elements. Later he [Ho58] ,Krohn [Kr62] and others turned to sputtering as a source of ions for mass-spectrometry, and their work must be considered as a first detection of the phenomenon of cluster sputtering. Of course, in these measurements only cluster ions were detected.
Later Woodyard and Cooper [Wo64] using post-ionization with electron beams found a surprisingly high fraction of sputtered clusters (dimers and trimers) in the flux of neutral particles. Models of sputtering process existing at the period of these investigations have been not able to explain large contribution of bound particles in sputtered flux.
Mass distributions of cluster ions were first reported by Blaise & Slodzian [Bl68] and Hortig & Müller [Ho69]. With the broad use of the SIMS analysis technique, such distributions became available for many elements and multicomponent targets. When assuming that charged and neutral distributions follow a similar behavior, all these results pointed towards an appreciable (20-30%, in some cases even more) bound particle flux. The picture changed somewhat when Gerhard & Oechsner [Oe75] published the first neutral-cluster intensity ratios, i.e., dimer-to-atom and trimer-to-atom ratios.

Unfortunately, unknown instrumental influences on cluster dissociation prevented an assessment of bound particle fluxes in the collision cascade regime.
With the development laser post-ionization technique still lower intensity ratios became accessible [Co91], [Wu93a].
Cluster size distribution for charged and neutral cluster is quite different. Fig. 2.1 shows cluster abundance distributions for a silver target, both for charged and neutral sputtered clusters. For both cases, a strong overall decay of the cluster abundance with the number n of atoms contained in the cluster can be observed In the case of ionized clusters mass distributions strong odd-even alternations are observed. This effect is best documented for monovalent elements and it is evident also for group III elements. It exists for both negative and positive cluster ions.
Even-odd alternations of charged clusters of monovalent elements are significantly less pronounced in the distributions of neutrals. Therefore, these alternations are related to the behavior of the ionization energy of these clusters. Another difference between ionized and neutral cluster abundance distribution is that neutral clusters show a stronger decay with atom number n than charged clusters in the range of low n values.

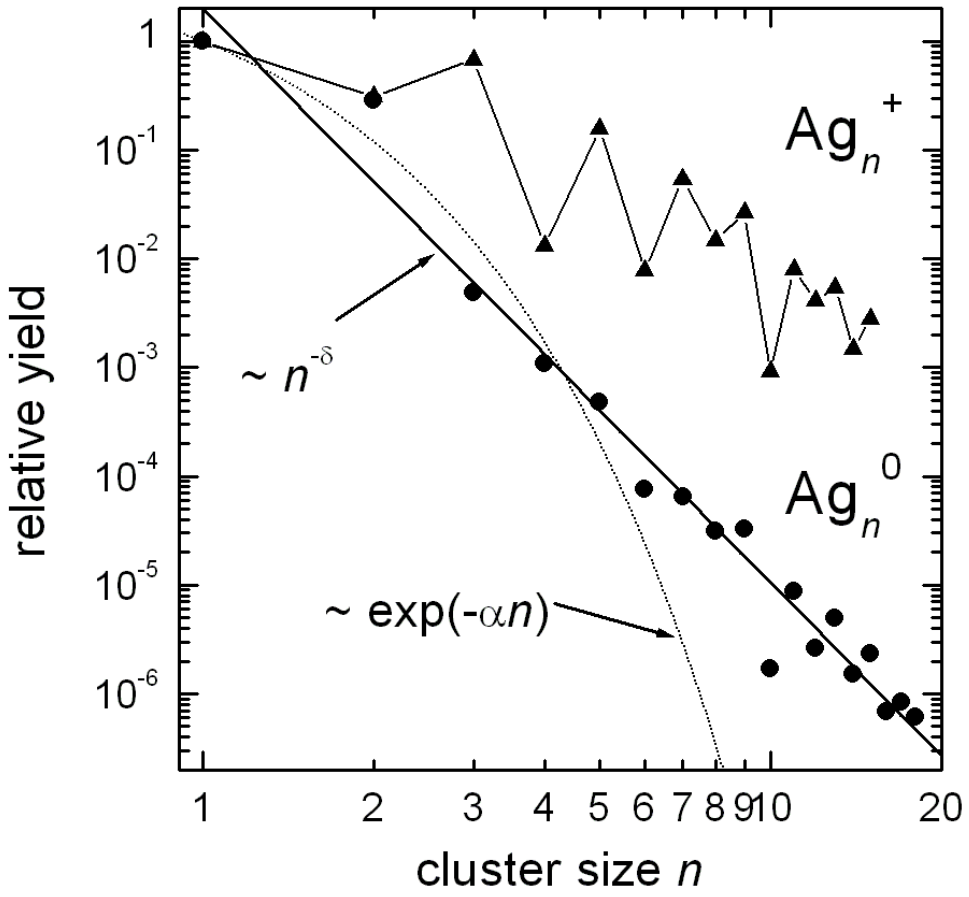

Fig. 2.1 Experimental data on sputtered Ag cluster abundance distributions of ionized clusters Ag_n^+ sputtered by 10 keV Xe^+ ions.[Ka86] and neutral cluster Ag_n sputtered by 5 keV Ar^+ ions [Wu93c]

The main observation in Fig. 2.1 is that the cluster yield distribution of sputtered neutrals closely follows a *power law* corresponding to $n^{-\delta}$ as a function of the cluster size n. This behavior has also been found for a number of other clusters (Al_n [Co93], [Wu93a] ,Cu_n [Co93], In_n [Co94], Nb_n and Ta_n [Wu96]) sputtered from the respective metallic surfaces and therefore seems to be a general feature of cluster emission in sputtering. Detailed

investigations reveal that the exponent δ strongly depends on the bombarded material [Co93], [Wu96] as well as on the bombarding conditions (such as energy and type of the primary ions [Wu93a], [Wu94a], [Co94]), while it is apparently independent of the crystallographic structure of the target material [Wu94b]. More specifically, it is found that δ is correlated with the total sputter yield Y_{tot} in a way which is depicted in Fig. 2.2. It is seen that large values of δ i. e. low relative contributions of large clusters, are connected to low values of Y_{tot} and vice versa. Kinetic energy spectra of cluster ions have been measured by many groups. Without exception, they show with increasing cluster size a faster decline of the high energy tail.

Implementation of laser postionization technique allowed to develop method of secondary ion probability measurement based on in situ determination of secondary ion and neutral particle densities above an ion bombarded surface [Wu94a]. Investigations [Wu99] show that ionization efficiency of clusters sputtered from different metal surfaces is cluster size dependent and varies for different metals. Measured ionization probability a^+ of sputtered Ag, Nb, Ta atoms was rather low and found to be below 10^{-3} which is in the good agreement with the common sense that the formation probability for atomic ions ejected from clean surface is generally low. For small clusters containing less than 10 atoms, the ionization probability is found to increase strongly with increasing nuclearity of sputtered cluster. This was observed for all studied metals and may be regarded as a general trend. For larger clusters containing more than 10 atoms, the ionization probability seems to saturate. Comparably low values of ionization probabilities (less than 10 percent) have been observed for large silver and germanium clusters in contrast to the data measured on Ta_n and Nb_n clusters. For tantalum and niobium ionization probabilities may be non-negligible even for small clusters containing as few as 4 (Ta) or 7 (Nb) atoms respectively.

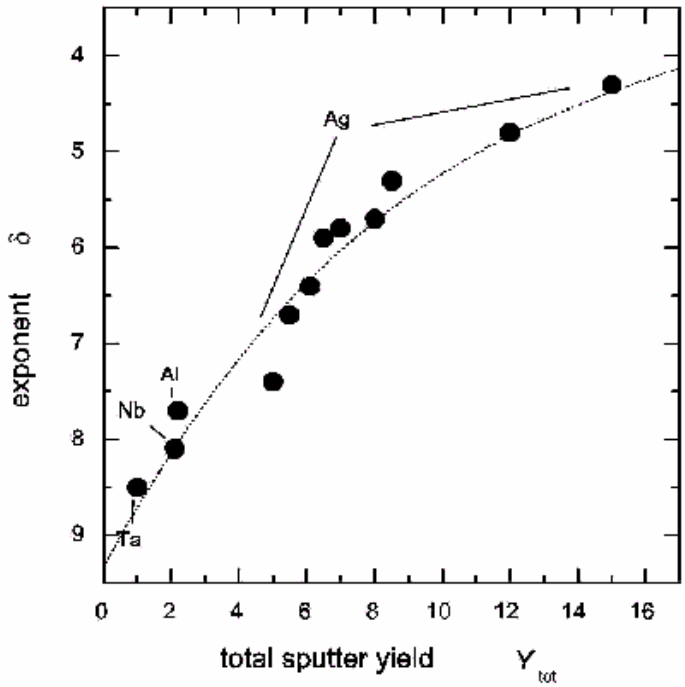

Fig. 2.2. Exponent of power law cluster yield distribution vs. total sputter yield [Wu93c]

When the surface of the solid is covered by (preformed) molecules in the sputtering measurements of their kinetic energy distributions shows E^{-2} like decay at high energies. This is strong evidence for the so-called single-collision emission mechanism, in which the molecule emission is induced by a single collision with a recoil particle of the

collision cascade. Under these conditions, the usual argumentation of collision cascade physics applies which predicts an E^{-2} tail of the kinetic energy distribution [Si81].
Concerning the cluster emission from elemental materials their kinetic energy distributions shows different behavior.
Experiments show that high energy tails of kinetic energy distributions of sputtered clusters are well fitted by power-law dependence. Kinetic-energy distributions of dimers sputtered from metals are steeper than the E^{-2} decay of the monoatomic distributions [Be76], [Br89] and [Co91]. The energy distribution of dimers appears to be better characterized by E^{-3} or E^{-4} decay. Wucher & Wahl [Wu95] showed for larger silver clusters with the number of atoms more than 4 atoms that this exponent remains practically constant around a value –4.
Sputtered clusters are not stable right after the ejection process. Collisional ejection leaves the agglomerates with a high amount of internal energy. This causes fragmentation during a time span of 10 μs or more after the clusters‘generation.
For metallic systems, cluster fragmentation has been studied at the Academy of Science in Tashkent by Dzhemilev et al [Dz96a], [Dz96b], [Dz96c], [Dz96d], [Dz97].
Due to the fragmentation mass distributions of clusters considered at early time after emission (≈10 ps) are different from distributions of clusters undergone decomposition during mass spectrometric analysis at the time of about few microseconds.
All these observations will be discussed in the frame of modern theories of cluster emission phenomena in sputtering in the chapter 2.4.

2.2 Computer simulation

There are several kinds of methods to simulate sputtering processes. Each having characteristic features which differentiate it from nominally similar ones.
Basically it is possible to identify four main categories.
First one is the method based on the integration of the classical equations of motion of a large number of particles simultaneously, commonly called molecular dynamics (MD) simulation.
Next are two kinds of methods based on the binary-collision approximation (BCA) to solve the equations of motion of projectiles which are assumed to interact with the target atoms one at a time. This is appropriate at high kinetic energies. The two types of BCA models are differentiated by the structure of solid target. In one group, as in the MD model, target has a definite structure. Besides conserving energy and momentum, such codes also conserve particles. The principle example of code for this model is MARLOWE. Second group of BCA codes utilize stochastic algorithm to determine the location of target atoms, to select impact parameters or scattering angles and so forth. In general these codes conserve energy and momentum in single collisions, but do not conserve the number of particles. The target is structures. There are no correlation between the positions of target atoms except those imposed by density of substance. The principal example of such programs is the family of TRIM codes.
And forth kind of methods are combining aspects of MD models with those of BCA models.
In following there is shortly described molecular dynamics (MD) code. The advantage of MD simulation that it allows to simulate cluster emission phenomena, what is in principle impossible using other methods.
The best known MD models for sputtering applications are those of D.E. Harrison, Jr. [Ha81]. The hallmark of the MD models used to simulate atomic-collision processes is

that they integrate the equations of motion of many atoms until the energy added in an initial disturbance is dissipated or until some other condition is met.
Various sorts of boundary conditions are used: periodic, dissipative, fixed, free, and so on. When the size of crystalline used in MD is large enough so that energy transfer through the boundary walls during simulation cycle do not influence on the output of calculations free boundary conditions may be used.
Two body interaction potentials were used originally, but several groups now use many-body potentials. Inelastic energy losses effect may be included. MD models are particularly effective in working out detailed mechanisms. The question still remains, however, about sizes of numerical crystallites required (events containment) and about the statistics of such calculations.
Pair potentials were used at the beginning of molecular dynamics. These potentials are effective in close encounters. The change in potential energy is determined almost entirely by the position of only two atoms, the other atoms of the target being merely spectators. In such encounters, a spherically-symmetrical, pairwise interaction potential is appropriate, essentially reflecting the atomic nature of the distribution of electrons about the nuclei. For some purposes, pair potential models are satisfactory and they are, moreover, more efficient computationally than more elaborate potentials. There are, however, many drawbacks.
Two main classes of many-body potentials have been developed for use in studies of transition metals and semiconductors. One class of many-body potential is based on a tight-binding (TB) analysis [Cy68]. Another class of many-body potential is based on the so-called embedded-atom method (EAM) [Da84].The main idea is to express the configuration energy of solid as the sum of two terms:

$$E_c = \frac{1}{2}\sum_{i \neq j} V_2\left(R_i, R_j\right) + \sum_i U\left[\sum_j g_2\left(R_i, R_j\right)\right] \qquad (2.1)$$

where the R_i are the positions of atoms, V_2 is a pair potential, g_2 is a pair function describing the local environment (for instance, electron density) of atom i in terms of the position of its neighbors, and U is a function describing how the energy of atom i depends on its environment. It is possible to go further and allow U to depend on three- or more-body environmental terms, thus introducing angular forces into the picture, and this is generally required for substances with strongly-directional covalent bonds.
Modern simulations employ many-body potentials, which are believed to be more realistic. Also in order to obtain a representative picture of the emission statistics, a large number of ion impact and cluster emission events, of the order 10^3 or more, must be simulated [Wu92]. Experimental data almost always represents an average over many impact/emission events and therefore for comparison of MD results with experimental data reliable statistics in calculations must be achieved.
Molecular-dynamic simulation allows getting valuable information about internal energies of sputtered clusters [Wu92b]. These investigations showed that significant fraction of sputtered metal dimers, trimers, and tetramers and virtually all sputtered multimers consisting of five or more atoms are unstable with respect to dissociation. Vast majority of such unstable clusters dissociate at the times about 10 ps. During this time particles travel only 100 angstrom away from the surface and therefore are not accessible to experiment. Therefore, during mass spectrometric analysis at the time scale of a few microseconds after emission only metastable fragments are detected.

2.3 Non-linearity in the sputtering

Non-linear effects in sputtering were postulated when Sigmund showed comparison between sputtering data and theoretical predictions [Si69]. While experimental yields from Ar irradiation of Cu, Ag and Au followed the theoretical predictions rather well, yields from Kr irradiation of Ag and Au showed a moderate enhancement around the yield maximum, while yields from Xe bombardment showed a moderate enhancement in Cu and a strong one (≈factor 2) in Ag and Au. It seems, however, that such enhancements of the yields under atomic bombardment are not found for low-yield (high-surface binding energy) materials [An81]. Enhancements are seen for high-yield materials if the stopping power is high (high Z_1; close to maximum in S_n) and recoil ranges are short (high Z_2). Hence, enhanced yields are seen for high energy deposition in the surface region.

The above statement is strongly corroborated by the systematic relative-yield measurements performed by Andersen & Bay [An73], [An75]. Their data are represented in fig.2.3. It is seen while the Sigmund theory predicts the Z_1 dependence of the yield at 45 keV well for silicon and nicely for copper, strong enhancements of heavy-ion yields relative to Ar sputtering is seen for silver and gold. The enhancements comprise in both cases a factor of 2.5 for the heavy projectiles.

Non-linear effects may also be defined from a theoretical viewpoint. The analytical theory of collisional sputtering ([Si69], [Si81]) is established through the solving of a Boltzmann transport equation describing the collision cascade. As an essential step in obtaining a solution of this equation, it has been linearized. Physically it means that moving atoms within the collision cascade are supposed to collide only with resting atoms, i.e., a moving atom will always loose and never gain energy through the collision. The solution of the linearized equation shows that the energy spectrum of the atoms set in motion within the cascade is approximately proportional to the inverse square of their starting energy. Hence, at sufficiently low recoil energy any atom within the cascade volume has been set in motion and the linearity assumption breaks down. If this breakdown occurs at an energy that is very low compared to energies characteristic for the sputtering process, e.g. the sublimation energy, no consequences are expected for the sputtering yield. The higher the energy density within the cascade, the higher breakdown energy. According to Eq. (1.4) energy density deposited in cascade volume is proportional to stopping power, therefore enhancement in the sputtering yield observed for the high yield materials with high stopping power is related to the nonlinearity of sputtering process in these cases.

Another way to enhance the energy density is through cluster bombardment. When polyatomic projectile impact the surface it disintegrates, and the kinetic energy of each individual constituent atom of projectile is deposited closely to each other in cascade volume. Or in other words, collisional cascades derived by each atom of projectile may interference.

Evidence of enhancement in the sputtering yield under heavy atomic ion bombardment prompted Andersen & Bay [An74] to attempt a direct experimental proof of the existence of non-linear effects. Silicon, silver and gold were bombarded with the dimers Cl_2, Se_2, and Te_2 and the corresponding monomers at the same energy per atom. Sputtering yield induced by diatomic projectile was compared with twice the yield produced by corresponding atomic one. In the case of linearity of the process these values would be equal and no enhancement must be expected. Experiment show that no significant enhancement was found for Cl_2 irradiation, but Se_2 yielded in all cases an enhancement, the larger the heavier the target. On fig. 2.3 are shown theoretical predictions from linear cascade theory with experimentally measured sputtering yields Si, Cu, Ag, and Au under bombarding with different ions with kinetic energy 45 keV [Be81]. Minor edition was

made for Ag sputtering with normalization of theoretical curve to be fitted for Ag sputtering by ions with low Z.

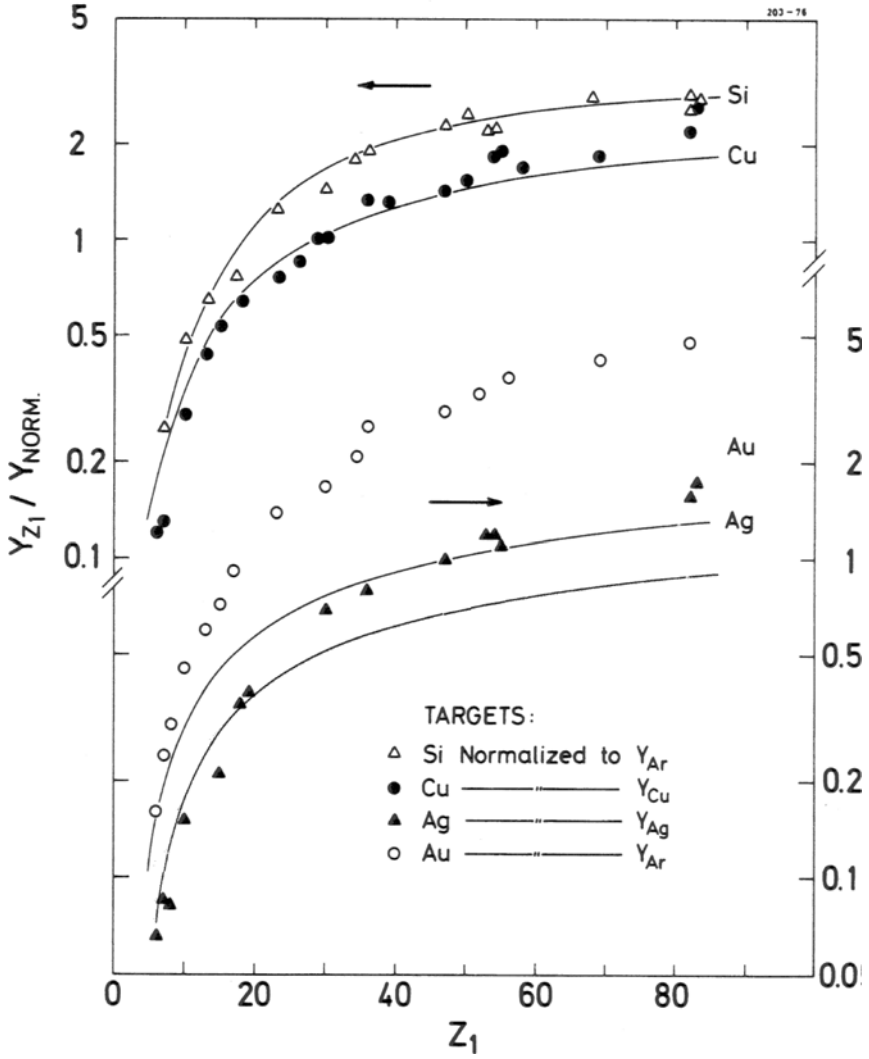

Fig. 2.3. Relative Si, Cu, Ag, and Au sputtering yields for 22 different ions at 45 keV. Data from Andersen & Bay [An73], [An75]. (After [Be81])

Johar & Thompson [Jo79] carried out a large systematic series of measurements of cluster effects. They bombarded Ag, Au and Pt with P, As, Sb and Bi monomers, dimers, and, for Sb, trimers over the energy range 10-250 keV. For Sb_3 enhancement factors as large as 10 of the sputtering yield per projectile atom were found.

More recently, new experimental data on the sputtering yield and cluster emission under bombardment with polyatomic projectiles have been obtained using new experimental possibilities.

Le Beyec et al. have performed experiments in a wide range of energies from keV to MeV per atom using gold clusters Au_m ($m = 1 \div 5$) produced by a liquid metal ion source [Le98a] to study sputtering process from gold target. Carbon clusters and C_{60} molecules were also produced at different velocities and used to bombard targets. Both secondary ion and total sputtering yields have been studied. It was shown that the emission of $\left(Au_n^-\right)$ (with $n < 5$) is several order of magnitude larger with Au_3 projectile than with Au_1 at 20 keV/atom. Insulating materials as CsI targets and organic targets were also bombarded by Au_m and molecular ions. The secondary ion emission of CsI clusters and of intact molecular ions were severely enhanced with cluster projectiles. The secondary ion yield

of molecules has been large under C_{60} ion bombardment in comparison with bombarding by atomic projectiles. It was shown that complex polyatomic ions are an excellent probe to analyze thin layers of molecules deposited on various substrates, as, for example, contaminant layers of organic compounds. Organic projectiles $73 \le m/z \le 1200$ were used at Orsay in event by event coincidence experiments [Le89b] and it was shown that non linear effect in secondary ion yield does not extend to large m values (m being the number of atoms in the projectile). In fact, above m around 20 the non linear effect was found to vanish and the secondary emission yield followed a linear dependence with m. Enhanced sputtering yield was also observed for neutral species. The total sputtering yield measurements of gold target bombarded by Au_m $(m = 1 \div 13)$ projectiles were performed in a large energy range from 20 keV to more than 2000 keV per atom [Le99]. The mass eroded from the sample was measured with a quartz microbalance. A sputtering yield as high as 1200 atoms per impact of Au_{11} was measured while a value of only 50 atoms was obtained for single Au projectiles at the same energy per atom (≈ 100 keV). The effect of the number of constituents in projectiles has been verified by comparing the emission yield of molecular ions produced by the impact of C_{60} and Au_n at the same velocity. At the bombarding energy of about 25 keV, the emission yield is more than 5 times larger with C_{60} than with Au_4 [Le99].

Practical use of polyatomic and molecular primary projectiles for routine SIMS and SNMS analysis have begun to be implemented.

Gillen has utilized Cesium sputter ion source on the magnetic sector SIMS instrument (Cameca IMS 4F). the Cesium sputter ion source has been used for depth profiling of 1 keV As implants in silicon comparing analyses with Cs^+ and CsC_6^- primary ions [Gi01]. In this example, a factor of ≈ 6 improvement in apparent decay length for the arsenic profile is observed with CsC_6^- ion beam. Comparison of yields obtained from amino acid films with C_1^- and C_8^- primary ions under identical conditions of current density, impact energy and incidence angle shows enhancement factors of up to 800. The yield enhancement at the kilo electron Volt impact energies used in commercial SIMS instruments appears to saturate between 8 and 10 constituents (for carbon containing clusters) [Gi01], [Be99a]. Under static SIMS conditions, the yield enhancement is analytically useful only if the corresponding damage cross-section does not increase in a similar fashion. Recent work has demonstrated that the damage cross-section does not increase as rapidly as the yield enhancement so that an improvement in the efficiency is obtained [Be99b].

The study of metal (Ta and Nb) and Si sputtering in form of charged clusters under atomic and polyatomic have been performed in Tashkent [Be00], [Sa00]. More detailed information about this study is provided in chapter 3.

Comparative study of SF_m (m=1÷6) with Cs projectiles has been performed in SIMS [De89] showing significant increase in the partial yields of molecular ions from surfaces covered by . The same study was performed for elemental samples when Si (100) surface was bombarded with SF_5^+ and SF^+ ions in comparison with Xe^+ [Ya98]. Results from this investigation indicate that the nuclearity of the bombarding ions significantly affects the ion cluster emission of Si_n^+. Abundance of cluster ions was increasing with number of atoms in projectile.

Most of the experimental data on the mass distributions of sputtered species sputtered under polyatomic ion bombardment was obtained for secondary ions.

Experimental study of mass distributions of self-sputtered Ag neutrals under polyatomic ion bombardment performed by Heinrich [He02] reveal that – in contrast to published

experiments on sputtered ionic species- the relative abundance of neutral clusters among the sputtered flux is not significantly enhanced with increasing projectile nuclearity. Relative yield of Ag cluster with nine atoms was similar under monomer and trimer ion bombardment with the same kinetic energy 7 keV/atom. This result is in contrast to the number of experimental data on ion sputtered clusters [Be00], [Ya98], [Mo03].
In addition to experimental investigation, molecular dynamic simulations [Li01], [Du04a] performed for a self sputtering of silver under mono- and polyatomic ion bombardment for a variety of kinetic energies of projectiles provide valuable information about nonlinearity of sputtering process. In the work [Li01] simulations were performed for Ag_m projectiles with $m = 1,2,3$ normally incident onto silver (111) surface with energy 2 keV per atom. Enhancement 19% for di- and 49% for triatomic projectiles is found. These factors are relatively less in comparison with experimental data [Le98a], but this difference may be due to the largely different impact energy of projectiles. The simulation reveal that the abundance of both nascent and final clusters within the sputtered flux is enhanced when polyatomic instead of monoatomic projectiles of the same impact velocity are used. The data suggests that the effect is the pronounced the larger the sputtered cluster. The magnitude of the enhancement appears to be larger upon switching from atomic to diatomic projectiles than upon switching from diatomic to triatomic projectiles. Simulation show that the kinetic energy distribution of sputtered atoms seems to be unchanged and do not show distinct difference. Therefore, the non-linear enhancement of sputtered yields explored was not accomplished by a collisional spike character of cascade in the energy range used in the simulation. Internal energy distributions of sputtered nascent clusters indicate that clusters produced under polyatomic ion bombardment are colder than those produced by monoatomic projectiles.
Duvenbeck has extended this simulation for projectile nuclearity and energy range of projectiles [Du04a]. The influence of the impact energy E_B on the sputter yield induced by an Ag_4 projectile in the range 0.5 to 8 keV have been investigated. The results clearly show two dependencies. In the range of low energies below 4 keV the data indicate a linear behavior, whereas for higher energies strong deviation from linearity is observed and show quadratic law. This result was interpreted in the terms of spike theory of Sigmund and Clausen [Cl80]. The linear yield contribution (Eq. 1.3) is assumed to be superimposed by an additional (thermal) spike contribution (Eq. 1.11) having quadratic dependence on the F_D - deposited energy.

2.4 Theoretical models of the cluster emission

The cluster emission process in sputtering has been frequently modeled by statistical combination approaches considering the atoms of the cluster-to-be to each receive energy in individual random collisions from the cascade produced by the ion impact of a single ion. If the momenta imparted to the atoms are sufficiently similar to that their relative kinetic energy does not exceed the dissociation energy of the cluster, and if the atoms are ejected close enough together in time, they will leave the near-surface region as a cluster. This mechanism can be called multiple collision model. The predicted kinetic energy distributions for the clusters formed by this mechanism show high energy tails that decrease much more steeply the larger the cluster [Sn87]. In addition, the cluster yields are predicted to be an exponential function of the number of atoms in the cluster [Wu95].
The corresponding single collision mechanism has also been proposed, in which one of the atoms of the cluster-to-be receives energy and other atoms are also ejected because

they are bound more tightly as a cluster than they are to the surface, and therefore, this mechanism is not suitable for emission of the clusters from clean metal surfaces. In addition, predicted energy distribution for this model shows a sharp cutoff at an energy dependent on the cluster dissociation energy [Ur87]. The dependence of the yield on the cluster size has not been calculated for this mechanism. These two mechanisms are collision based ones.

In addition to the collision based models several mechanism of the cluster emission have been proposed at the moment: (1)unimolecular decomposition of a vibrationally excited volume, (2) emission from thermally equilibrated volume, (3) emission due to a shock wave intersecting the surface, (4) correlated emission due to multiple collisions with the same recoil atom or with the primary ion.

(1) The model of Lin et al [Li83] treats the volume of the solid affected by the primary ion as a vibrationally excited region. The theory is based on the conversion of the vibrational energy to electronic and/or transnational energy during energetic ion impact on solid surface, in particular, non-conducting solids. Group of particles with vibrational energy is considered as isolated microcanonical system weakly coupled to the rest of the solid.

(2) Using molecular-dynamics computer simulation, Urbassek at el. [Ur96] performed a model study of the processes occurring after the sudden energization of a laterally infinite metallic slab. For small initial energy densities, only a small number of atoms evaporate from the metal. For high energy densities, the solid atomizes, and only small clusters are formed with an exponential cluster abundance distribution. In an intermediate regime, prolific cluster formation is observed with a polynomial decay of the abundance distribution. These results are discussed in the light of the critical point of the gas-liquid phase transition. Depending on whether chemical equilibrium is established and on the temperature with respect to the critical temperature when the system crosses the liquid-gas coexistence curve the predicted mass distribution can be exponential, power law with exponent of –7/3, or a combination of the 2. This model was used fairly successfully to fit mass distributions of Ar_n^+, N_n^+, Ni_n^+, and $Cs[CsI]_n^+$. Although not stated explicitly, the predicted cluster kinetic energy distribution would be thermal, i.e. exponential, in nature.

(3) The shock-wave model [Bi87] invokes non-linear conditions that result in the creation of a shock wave. This shock wave propagates to the surface and reflects from it. The stresses created result in the emission of (possibly large) clusters. These clusters have relatively little internal energy since they were ejected as a result of correlated motion. The predicted high energy tail of the kinetic energy distributions of the clusters is E^{-2} dependent. In addition, this model does predict a power-law dependence of the yield on the number of atoms in the cluster for large clusters. However, the predicted exponent is of the order of –2, quite different from larger negative exponents observed experimentally.

(4) The model of Joyes [Jo71] describes the atoms of clusters as being emitted from correlated collisions with the same recoil atom. Bitensky and Parilis [By78] also modeled correlated collisions with recoils, as well as with primary ion. In these models, a high energy particle strikes the cluster-to-be in such a fashion as to impart roughly the same momentum to each atom, for instance, at high impact parameter parallel to the molecular axis of a dimer. Collisions of this type result in stable high energy clusters because of the low relative kinetic energy of the atoms in the clusters. Bitensky and Parilis calculated, by molecular dynamics simulation, the energy distributions of Cu_2 created by this mechanism from Ar^+ sputtering of Cu(110) at 10 keV and 10^o (from surface normal) incidence [Bi80]. For dimers emitted within 15^o of normal, there were peaks in the distribution at the 10-20 eV bin and the 80-90 bin.

Correlated collision mechanisms, therefore, do produce significant amounts of high energy clusters. Another of Bitensky´ and Parilis´ simulations [Bi78], which included varying angle of incidence onto Cu(100), showed that as many as 30% of the dimers were formed by correlated collisions, rather than by random multiple collisions. It is therefore plausible that at least high energy dimers and trimers could be formed by this mechanism. Since the measured energy distributions are from polycrystalline Cu and thus represent an average over all incidence angles and crystal faces, prediction of the energy distribution, as well as the contribution of this mechanism to the total cluster sputtering yield is difficult. It should be noted that while the molecular dynamics simulations of cluster sputtering [Wu92a] do not show this to be a dominant mechanism, these calculations are for perfect surface and normal ion beam incidence, in most cases. The dependence of the mass distribution has not yet been predicted for these models, although Bitensky and Parilis state that this mechanism is not expected to be dominant for clusters larger than three atoms.

3 SIMS results for polyatomic ion bombardment

3.1 Introduction

In this chapter there are presented initial data on the secondary ion emission from Nb and Ta metal surfaces under atomic and polyatomic ion bombardment by Au_1^-, Au_2^-, Au_3^- with 6 keV per atom impinging energy are presented.
These measurements were performed by author after initial investigation by D. Mulajanov [Mu97]. He has investigated cluster ion emission from Ta sample under atomic and diatomic gold ion bombardment with 8 keV per atom kinetic energy of projectile.
At the moment of the starting of this work most of the data for emission of charged clusters from metal surfaces were obtained under atomic ion irradiation [Dz96], [Ka86]. During last decade with the development laser postionization techniques, new information for emission of neutral clusters under atomic ion bombardment was also obtained [Wu93a], [Co91].
The most important results may be summarized in the following.

- The unimolecular decay of sputtered cluster ions were found [En83], [Dz987].
- It is shown that the cluster ionization probabilities increase with the increasing of the number n of atoms in cluster [Wu94a].
- A power law dependence of neutral cluster yields $Y(n) \propto n^{-\sigma}$ on the number n, where exponent σ depends on mass m_1 and energy E_0 of a projectile, and on the mass m_2 of the target atom was established [Co91, Wu93, Co93,Wu96].

- The empirical relation of exponents and total sputtering yields was revealed for many combinations of „projectile-target“ [Co93].

In this work the cluster ion emission from metal surfaces under polyatomic ion impact was extended into the range of keV energies which are common for SIMS and SNMS surface analysis techniques.

3.2 Experimental

In this study, a secondary ion mass spectrometer developed from a commercial MI-1201 instrument produced by SELMI (Sumi, Ukraine) was used. This instrument utilizes magnetic sector mass analyzer. To study the cluster emission under polyatomic ion bombardment, this instrument was equipped with an Au_m^- negative ion source (m = 1-3) [Be92]. The experimental setup is shown in fig. 3.1. The apparatus consists of a negative ion source (1-5), a mass separator for the primary ion beam (8), a primary ion optical system (6,7,9 -11) for acceleration, formation and deflection of the primary ion beam, the target assembly (12), a secondary ion optical system (13, 14) and MI-1201 mass spectrometer (15,16).
For mass separation of the primary ions a stigmatic magnetic sector mass separator was used. The radius of the mean trajectory is 14 cm. The maximal value of the magnetic field was 1200 Gauss. Au_m^- ions of different m (1,2,3) had been separated at kinetic energy of 500 eV , determined by the voltage U_{tar} of the sputter target 4 relatively to the body of ion source, and the resolution of the mass separation under these conditions for monoatomic ions Au^- is about 6.
Typical values of the primary ion currents for atomic gold ions were 20 nA with the current density $1{,}5 \cdot 10^{-8} A/cm^2$. Parameters of polyatomic ions Au_2^- and Au_3^- were smaller by factor of 6-7.
Body of the ion source, including first electrode of immersion lens 10 (fig. 3.1) was floating and applied the voltage U_{acc} in the range from –3.5 to –15.5 kV. This voltage induced postaccelerating electrical field in the space of immersion lens 10.
During measurements, sample has been applied voltage U_{samp} of 2000 V.
Therefore, the total kinetic energy of impinging ions E_0 can be calculated by the following equation:

$$E_0 = e \cdot \left(U_{samp} - U_{tar} - U_{acc} \right)$$

where e is an elementary charge.
The impact angle of the primary ions was 45°. Ta and Nb samples were chosen due to their monoisotopic nature and high melting temperature. The temperature of Nb and Ta samples during the experiment was maintained at 1800°C and under vacuum conditions where the residual gas pressure did not exceed 1×10^{-7} mbar. Under these conditions the signals of TaO^+ and NbO^+ oxide molecules were dropping by three orders of magnitude with respect those measured at room temperature. The surface prepared in such a way was believed to be a “clean surface”.

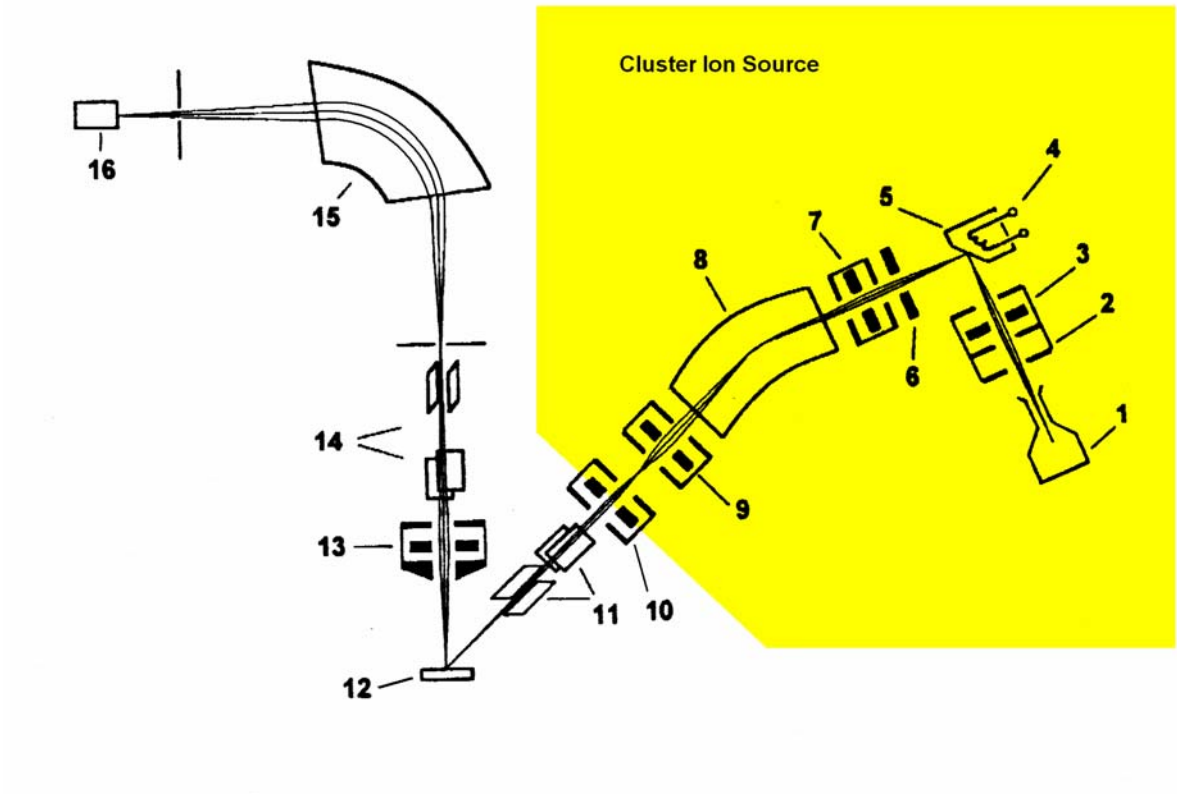

Fig. 3.1. Scheme of the experimental apparatus: 1 – the surface ionization Cs^+ ion source; 2 – accelerating electrode; 3 – einzel electrostatic lens; 4 – target heater; 5 – the Au target (gold foil); 6 – accelerating electrode; 7 – einzel lens; 8 – the stigmatic magnetic mass separator; 9– einzel electrostatic lenses; 10 – immersion lens; 11 – primary ion deflection system; 12 – Nb or Ta sample (foil); 13 – secondary ion lens; 14 – deflecting system; 15 – magnetic mass analyzer; 16 – detector (electron multiplier).

3.3 Mass spectra of secondary cluster ions

In fig. 3.2 and 3.3, mass spectra of Ta_n^+ and Nb_n^+ ion clusters sputtered by polyatomic projectiles are shown. All spectra were normalized to the signal of atomic ions.

The main feature of these mass spectra is as follows. Relative contributions of secondary cluster ions caused by polyatomic ion impact are much higher than those induced by atomic ion impact. The ratio between these yields increases rapidly with increasing cluster size reaching values more than two orders of magnitude for Ta_{10}^+ cluster ion.

In the range of small cluster ions with $n<4$ redistributions of peaks are observed under polyatomic sputtering.

These results demonstrate the effect of non-additivity of the formation of large cluster ions in sputtering of clean Nb and Ta by polyatomic gold ions with rather low incident energies $E_0 < 10$ keV/atom.

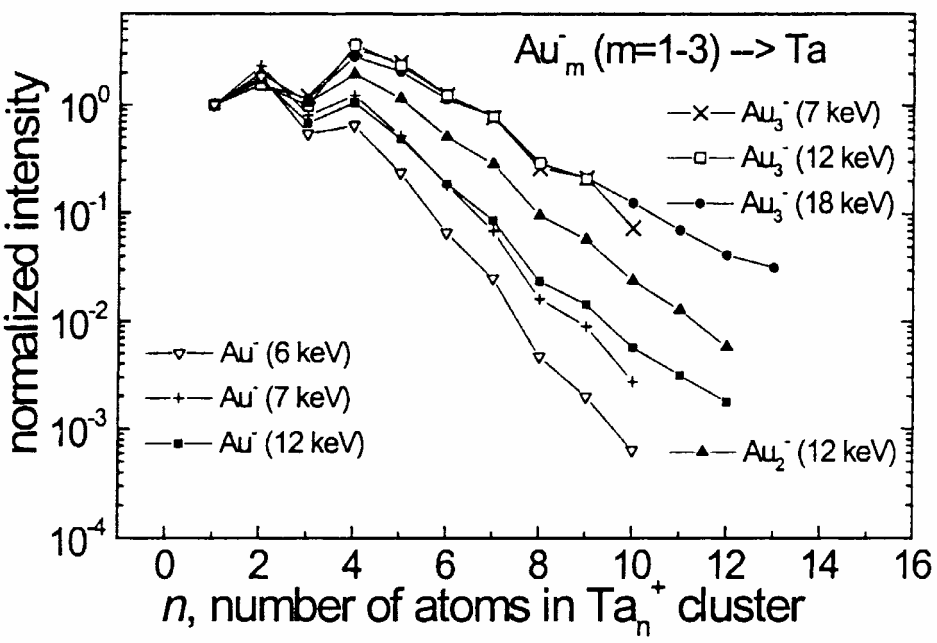

Fig. 3.2. Mass spectra of Ta_n^+ secondary ions sputtered by 6, 7, 12 keV Au^- and 7, 12, 18 keV Au_3^- primary ions.

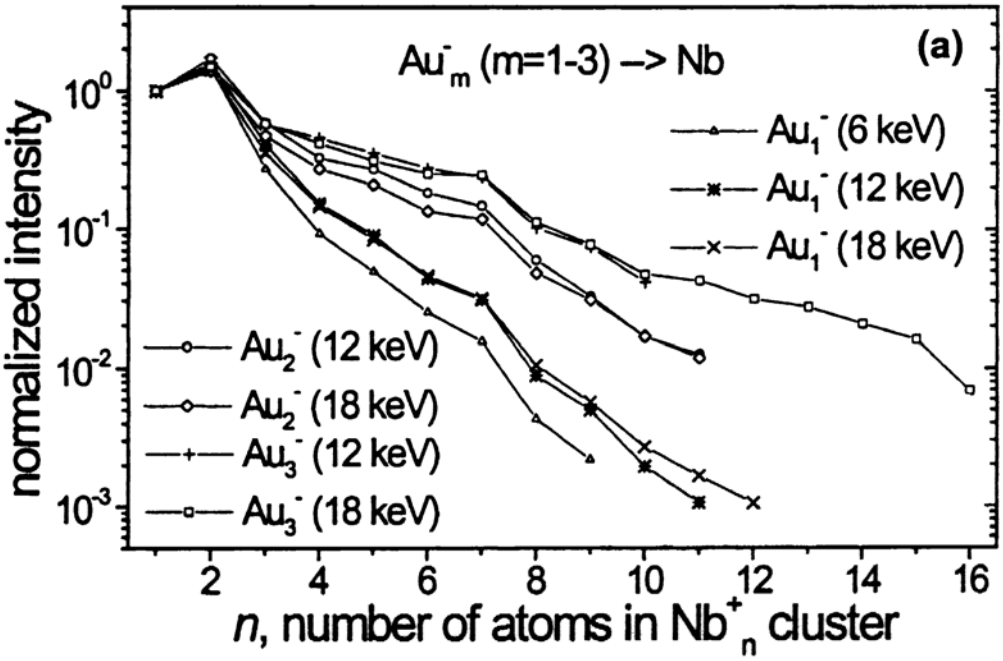

Fig. 3.3. Mass spectra of Nb_n^+ secondary ions sputtered by 6, 12, 18 keV Au^-, 12, 18 keV Au_2^- and 12, 18 keV Au_3^- primary ions.

As it was shown in the introduction, the secondary ion yield $Y_X^{\pm}$, sputtering yield Y_X and ionization probability $\alpha^{\pm}$ are related by the following expression

$$Y_X^{\pm} = \alpha_X^{\pm} \cdot Y_X \qquad (3.1)$$

The enhancement observed in fig. 3.2 and 3.3 can, in principle, be induced by enhancement of partial sputter yield Y_{X_n} of corresponding n-atomic clusters or by enhancement of the ionization probability $\alpha_{X_n}^{+}$ of these clusters (Ta_n or Nb_n).
First would reflect changes in the collision cascade dynamics under polyatomic ion bombardment leading to enhanced emission of clusters. Second would reflect changes in the electron exchange process between sputtered species and surface.

3.4 Kinetic energy distributions (KED).

The kinetic energy spectra $f(E)$ of Nb_n^+ ions (n = 1 – 11) sputtered by atomic and polyatomic Au_m^- projectiles (m = 1 – 3) with energy E_0 = 6 keV/atom have been measured.
The kinetic energy distributions $f(E)$ were obtained by a variation of sample accelerating voltage U_{samp} relative to 2000 V. Full width at half height (FWHH) of the energy window of the SIMS instrument was 5.5 eV. FWHH was determined by the measuring energy spectra of surface evaporated ions of alkali metals K and Na from hot surface of the sample.
In order measure the kinetic energy distributions of Nb_n^+ ions, the magnetic mass analyzer of the spectrometer was aligned to the maximum of the signal. After that the procedure of KED measurements by voltage variation on the sample has been performed. Therefore, values of most probable kinetic energy for all measured kinetic energy spectra are shifted to zero value.
Typical normalized dependencies $f(E)$ for Nb_n^+ ions (n=1, 2, 4, 7) are shown in fig. 3.4. For Nb_n^+ ions the extended energy „tails“ in negative range (relative to $e \cdot U_{samp}$ = 2000 eV) correspond to unimolecular fragmentation of parent ion into the fragment $Nb_n^+ \rightarrow Nb_{n-1}^+ + Nb$ within the acceleration zone of the mass spectrometer [Dz86]. Due to the fact that during fragmentation process the fragment Nb_{n-1}^+ conserves only part of kinetic energy of parent ion determined by mass ratio Nb_{n-1}/Nb_n, it has energy deficiency relative to the eU_{samp}. The magnitude of the deficiency depends on the time when fragmentation has occurred during acceleration of parent ion Nb_n^+ in the field zone between sample and extractor of spectrometer.
It was observed that relative contribution of the fragment ions in the energy spectra increases with the number n. Moreover, for dimer Nb_2^+ this contribution is much higher for polyatomic bombardment as compared to the atomic one: $Au^- \rightarrow Au_2^- \rightarrow Au_3^-$ at the energy of 6 keV per atom. Increased contribution of the fragment ions under polyatomic

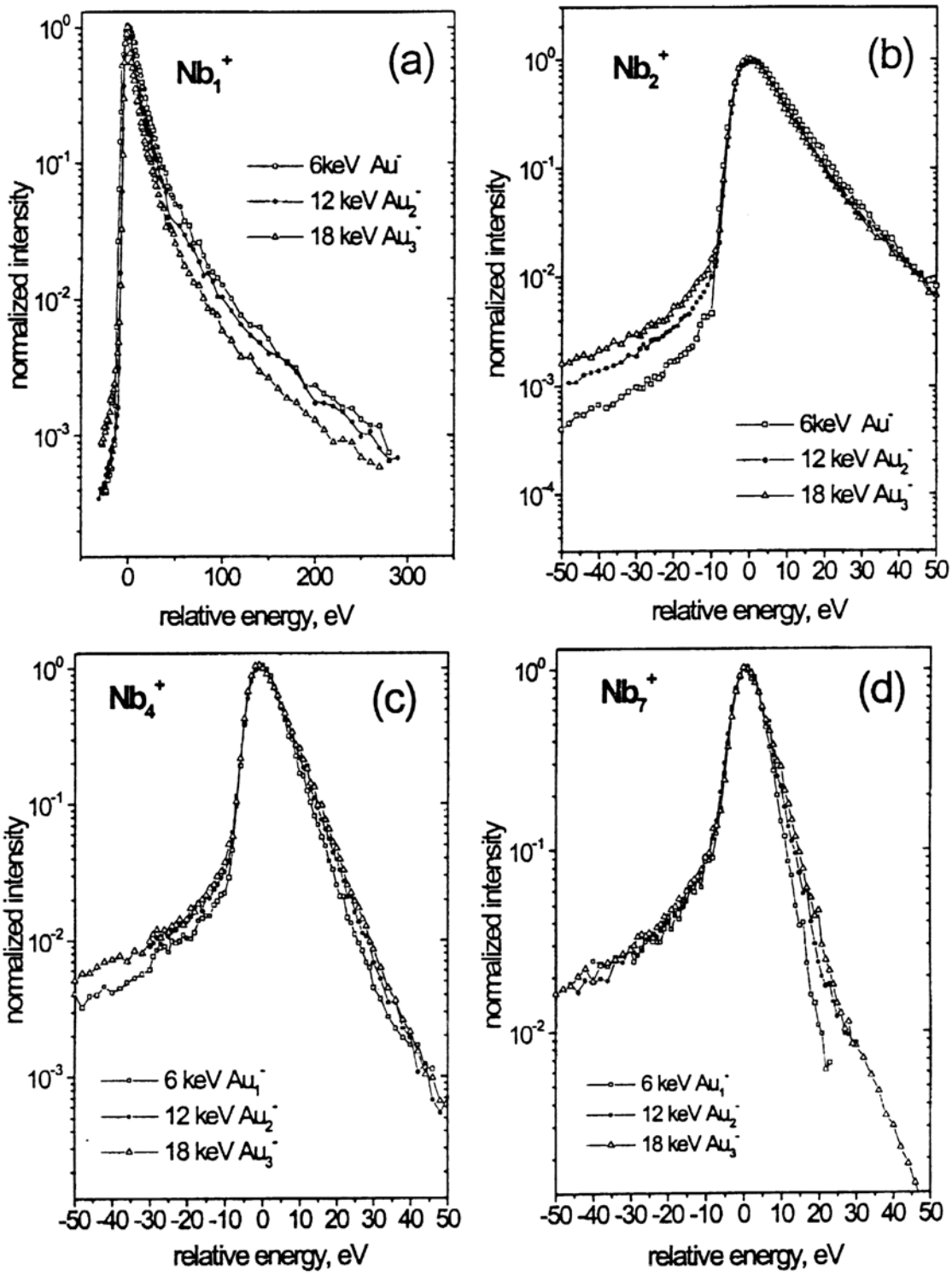

Fig. 3.4. Kinetic energy spectra of (a) Nb^+, (b) Nb_2^+, (c) Nb_4^+ and (d) Nb_7^+ secondary ions sputtered by atomic and polyatomic Au_m^- (m =1 – 3) primary ions with energy E_0=6 keV/atom.

ion bombardment is also seen for Nb_4^+ (with less extent), and for Nb_7^+ this effect nearly not observable. Increase of fragment ions may be explained by enhanced fragmentation of parent cluster ions which could be if the internal energy of these species is higher under polyatomic ion bombardment. Recent MD simulations [Li01] performed for silver self sputtering show that clusters sputtered under polyatomic irradiation have less internal energy (clusters are colder) in comparison with atomic bombardment.
On the other hand, higher contribution of fragment ion may be explained by increase of relative partial yields of parent-like cluster ions under polyatomic ion bombardment which is, actually, observed in the mass distributions (fig. 3.3).
The behavior of dependencies $f(E)$ in the high-energy range (relative to eU_{acc}) is very different for $n \le 2$ and $n \ge 3$. In the first case, the relative yields of Nb^+ ions with given kinetic energy E decrease during a transition from atomic ion bombardment to a polyatomic one: $Au^- \rightarrow Au_2^- \rightarrow Au_3^-$ at the energy 6 keV per atom and these results are in the good agreement with well-known data [Th81]. Energy distributions of dimer ions Nb_2^+ shows, practically, no change upon transition from monoatomic to triatomic projectiles. The relative yields of Nb_n^+ ions at $n \ge 3$ with given kinetic energy E increase during transition from atomic ion bombardment to polyatomic one. Thus, kinetic energies of large cluster ions ($n \ge 3$) sputtered under polyatomic ion bombardment are higher than those produced under atomic ion bombardment at the same energy per atom.

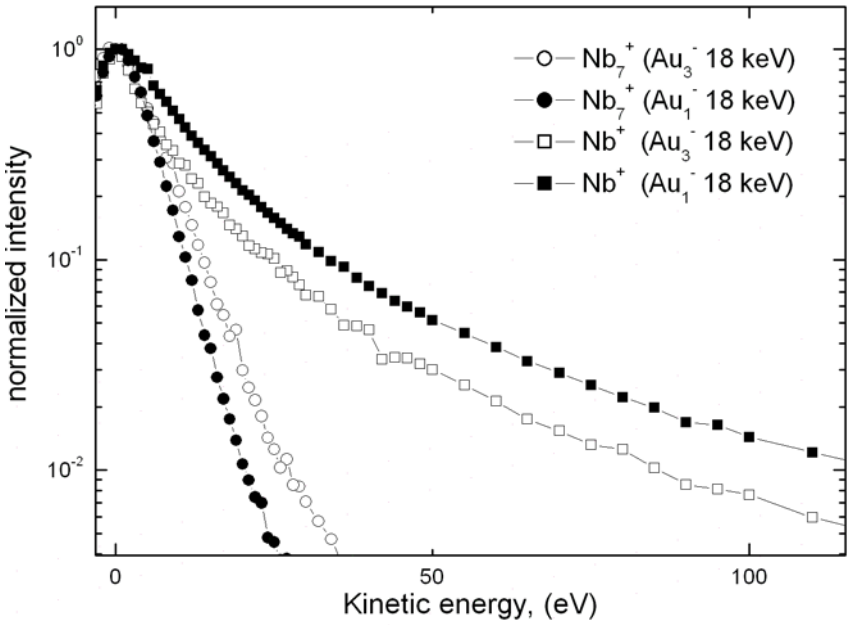

Fig. 3.5. Kinetic energy spectra of Nb^+ and Nb_7^+ secondary ions sputtered by atomic and polyatomic Au_m^- (m =1, 3) primary ions with total impinging energy E_0 = 18 keV.

In the fig. 3.5 kinetic energy distributions of Nb^+ and Nb_7^+ ions sputtered by atomic and polyatomic projectiles Au_m^- (m =1, 3) with energy E_0 = 18 keV are plotted together. It is clearly seen that energy distributions of sputtered monomer ions becomes narrower, i.e., falls off more steeply upon transition from monoatomic to polyatomic projectiles. Energy distributions of large clusters become broader upon transition from monoatomic to polyatomic projectiles. Since the energy window of the spectrometer is quite large (11

eV) it is difficult to make detailed analysis of the kinetic energy distributions of Nb^+ and Nb_7^+ in low energy range ($E < 10$ eV) on the basis of this data.

The tendency of Nb^+ monoatomic ions to become narrow may be explained by appearance low energy contribution in the yield of secondary ion under polyatomic ion bombardment.

Dependencies of kinetic energy distributions of atomic and cluster ions of tantalum are behaving in the same way.

Recent investigations of Morozov [Mo03] using the same experimental setup have been performed including similar target-projectile combinations with equal kinetic energy per atom in the projectile. Morozov has used different method to obtain data on the kinetic energy spectra of secondary ions. In contrast to voltage variation method he has used scanning of the magnetic field of analyzer. Though the energy window of instrument remain the same, this method allow to measure shifts of most probable kinetic energy distribution upon transition from atomic to polyatomic ion bombardment. With increasing number of atoms in the bombarding ions the kinetic energy distributions of secondary monoatomic ions become narrow and most probable kinetic energy move to low energetic region.

4 Conclusion

From literature and SIMS data the information about polyatomic projectile bombardment can be summarized in the following:

- Non-additive enhancement of total sputtering yield
- Enhancement of relative cluster ion yields
- Transformation of the kinetic energy distributions of atomic and polyatomic secondary ions

The features of secondary ion emission observed under polyatomic ion bombardment , as it has been stated above, can be affilated to either changes of collision mechanism of sputtering process or to the changes of the ionization process (due to the changes in the electronic excitation within collision cascade) of the sputtered species.
It is not possible to distinguish which process is influenced more under bombardment with polyatomic projectiles or complex changes in both of them occur.
Therefore, further investigation with possibility of detection of neutral sputtered species (laser postionization mass spectrometry) are required.

EXPERIMENT

5. Introduction

Investigation of species leaving the surface in a neutral state by means of mass spectral analysis leads to the necessity to use the postionization technique. In order to obtain quantitative information from the measured mass spectra it is important to achieve the ionization efficiency, or, in other words, the ionization process must be in saturation mode for all particles in the ionization volume. If postionization process is in the saturation this eliminates the influence of different cross-sections on the detection sensitivity of different species. High postionization efficiency, also, increase the sensitivity of measurements. Moreover, the postionization technique must be sufficiently soft to avoid significant fragmentation of sputtered species.

Laser based photoionization methods have recently evolved. This is the most sensitive method. In order to achieve high ionization efficiency the laser source must be pulsed. Because only in this mode necessary laser intensity may achieve necessary power density to drive the photoionization into saturation. This means laser postionisation ideally complements high-transmission ToF-SIMS instruments in which the desorption beam may be also pulsed to minimize the surface damage.

There are three basic mechanisms by which photon excitation can cause a neutral cluster/atom to ionize. The most elegant approach is Single Photon Ionization (SPI) whereby the absorption of one photon promotes an electron directly into the ionization continuum. For most atoms and molecules this requires photon energy of about 10 eV, in the vacuum ultraviolet (VUV) region of the spectrum. Photon sources emitting in this region are typically very low power and so are hard to achieve the efficient ionization. However there exist several mechanisms for generating relatively intense pulses of VUV photons (10^3 W/cm^2) by frequency-conversion of pulsed laser wavelengths.

A second mechanism for laser ionization is to use a multi-step method whereby a photon of the correct energy promotes an electron to a real intermediate electronic state within the neutral. Subsequent photon absorption(s) of the same or different energy then induce ionization. This is called Resonance-Enhanced Multiphoton Ionization (REMPI). To reach the ionization level the neutral that has absorbed one photon and exists in an electronically excited state must absorb subsequent photon(s) in a short time period before it can relax to the ground state or dissipate the electronic energy by undergoing processes such as fragmentation. This condition is met by irradiating the neutral with a high flux density of photons such as is obtained by a pulsed laser (typically more than 10^3 W/cm^2). If the laser power is too high the atom/molecule will continue to absorb photons once it has been ionized. This leads to fragmentation or multiply-charged ions.

The third method of laser postionization involves irradiating the neutral with photons of arbitrary wavelength at such a high photon flux density that multiphoton absorption occurs even though real intermediate electronic states are not resonantly excited. This is called Non-Resonant Multiphoton Ionization (NRMPI). As no intermediate electronic levels are populated the multiphoton absorption must occur on an ultrashort timescale (10^{-15} s) if ionization is to be achieved. This requires very high power laser pulses (>10^9 W/cm^2).

In experiment the laser beam at wavelength of 193 nm was chosen to provide photionization of sputtered species. The commercial Excimerlaser (Lambda Ohysik, LPX 120i) has been used, and it provides laser intensity up to 200 mJ for wavelength of 193 nm. In addition, at this wavelength laser irradiation at UV region and it eliminates the necessity to provide the deoxygenated volume between laser and vacuum chamber, which significantly simplifies the experimental procedure.
The investigated sample is polycrystalline Indium foil with 0.5 mm thickness. The indium was chosen as the sample for the following reasons:

- the post-ionization of sputtered neutral indium atoms and clusters is easily saturated using single-photon ionization at wavelength 193 nm [St02] .
- it is known that rare gas ion bombardment of an indium surface produces large amounts of In_n clusters [St02].

6. Experimental Setup

6.1 General description

The investigation of cluster emission from an indium surface under polyatomic ion bombardment has been performed using an ultra high vacuum apparatus for surface analysis by single photon ionization of sputtered species. The schematics of the setup are shown on the fig. 6.1. The experimental setup consists of the following main parts : time – of-flight (ToF) mass-spectrometer, cluster ion source, sample.
The primary ion column works on the basis of the same principle as that used for SIMS studies at Tashkent. More specifically, primary negative ion clusters are produced by means of sputtering of a negatively biased gold target by cesium positive ions. The cesium ions are created when vapor of cesium produced from dissociation of CsCl salt flows through a hot ionizer made of porous tungsten. The ionizer is heated to a temperature of about 1100 C^o. Due to the opposite charge the produced gold ion species are accelerated in the reverse direction as compared to the Cs ions impinging on the target. After acceleration, the gold ions are focused, mass selected, and directed to the analyzed sample. Mass separation of the projectile particles is performed by means of a Wien Filter. Detection and measurement of the primary ion current is performed using a Faraday cup mounted under the sample. A detailed description of the cluster ion gun is given in the following chapter.
For cleaning of the surface and alignment of the spectrometer, a second ion gun producing rare gas ions (duoplasmatron) is installed in the main chamber.
Both ion sources irradiate the sample under 45^o angle of incidence.
Sputtered neutral emitted species from the sample surface under monoatomic and polyatomic irradiation are postionized by an intense UV laser beam with a wavelength 193 nm.
Measured signal was corresponding to the number density of sputtered species in the laser ionization volume. Then post-ionized species are accelerated by applying to the sample high voltage pulse and analyzed in a ToF–MS of the reflectron type. After mass-separation they are detected by a chevron type microchannel plate – MCP2. For

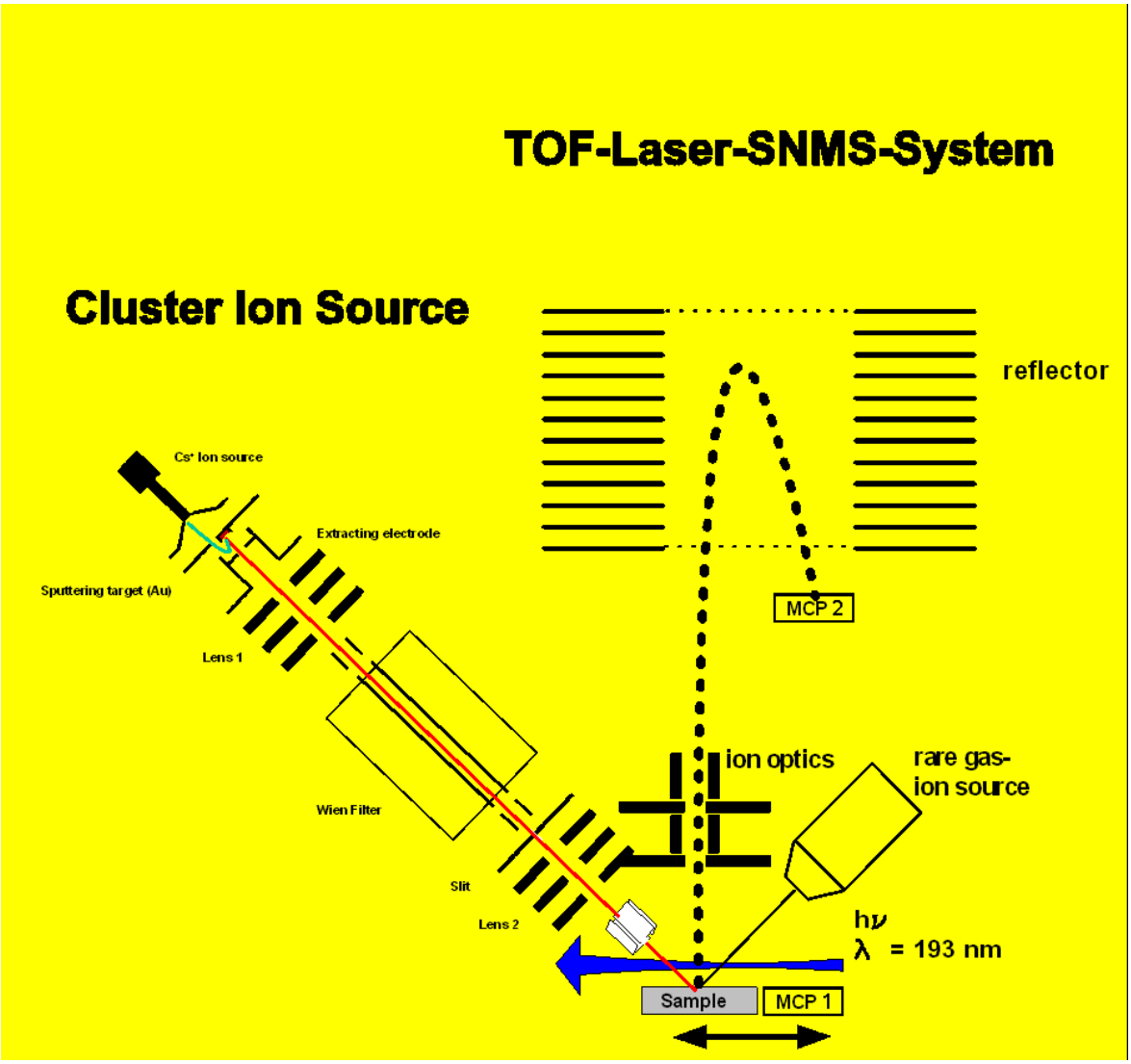

Fig 6.1. Experimental setup

acquisition of signal from MCP2 a high speed digital oscilloscope connected to PC is used.

Measurements using TOF-MS have the pulsing nature. All timing and pulse generation are managed by a digital delay/pulse generator. The more elaborate and detailed description of the timing in different modes of measurements like mass-spectra data acquisition and velocity distributions measurements are described in the chapter 7 devoted to methods of measurement procedures. Comparative measurements of the kinetic energy distributions and mass-spectra of sputtered Indium species sputtered by atomic and polyatomic ion bombardment were performed under the same experimental conditions.

For detection of a short pulses of primary ion beam and their syncronization in time with laser pulses an additional microchannel plate MCP1 was used. This MCP has been installed on the sample transfer and could be moved in the position of the sample.

Power density of laser beam, its position above the sample surface and focus was varied for different modes of the measurements (velocity distributions, mass-spectra).

6.2 Vacuum system

The main ultra high vacuum chamber housing the ToF experiment is constructed from two hemispherical parts with diameter 20 cm. There are several flanges of CF63, CF35 standard welded to the main chamber. Time-of-flight mass-spectrometer is verticaly connected to the middle upper part of the main chamber‘s sphere. There is a CF63 flange with Ca_2F entrance window for postionizing laser beam, a CF63 flange with a UV/VUV-Detector, a CF 100 flange with xyzΦ-Target-Manipulator welded perpendicular to each other and lying in a horizontal plane. CF63 and CF35 flanges for the cluster ion source and the rare gas ion gun, respectively, are welded under 45^o angle. There is a turbomolecular pump which is connected to the bottom part of the chamber. Using this turbopump (Leybold-Heraeus Turbovac 340 M, pumping speed 270 l/s) and a standard rotary vane pump (Leybold-Heraeus, Typ D16B) working as forepump, the residual gas pressure $5 \cdot 10^{-9}$ mbar rising to $2 \cdot 10^{-8}$ mbar during operation of the cluster ion source. When duoplasmatron is started, the pressure in the chamber increases up to $2 \cdot 10^{-7}$ mbar mainly from the atmosphere of the operating rare gas.

6.3 Cluster ion gun

6.3.1 Generation of the clusters

The mass spectrometric study of negative ion sputtering of some solids during bombardment by positive alkali metal ions has revealed that the presence of an alkali film which is deposited on the surface creates a favorable conditions for emission of negative ions [Ay69], [Kr62]. Alkali film may be deposited by the incident itself or from special evaporator.
This finding is widely used in secondary-ion mass spectrometry for sensitive detection of electronegative elements by detecting their negatively charged ions.
It was shown in those publications that during cesium ion bombardment of targets like Al, Zr, Si, Cu, CuBe, Ag, Au, Ni and graphite atomic and molecular negative ions are sputtered from target material have been observed. All these experimental results show cesium bombardment to lead to reduction of the surface work function which partially transforms the usually neutral atoms and multiple atom complexes (clusters) into a negative ion state.
In 1973 Middleton and Adams developed a new type of negative ion source in which negative ions are generated by sputtering of a solid surface with positive cesium ions [Mi73]. The sputter source has several advantages over its predecessors: (1) negative ions (elemental or molecular) can be formed from almost all elements and the ion species can be quickly changed, (2) the achievable ion currents are fairly high, (4) the efficiency of ionization is good, (5) emittance and energy spread are low.
In principle, a negative cluster ion source of the sputtering type consists of the following basic parts: a cesium surface ionization ion source, a sputtering target, ion optics for formation (separation) of the negative ion beam.
Surface ionization (SI) ion sources are very effective and widely used sources for atomic ions. The construction of a SI ion source is extremely simple. Basically there are two parts: a cesium reservoir and an ionizer. The ionizer is usually made from porous tungsten due to the high melting temperature and large value of the work function at this material.

In principle metallic cesium could be inserted into the reservoir if contained in a hermetic ampoule, which must be broken in vacuum. Cesium vapor is produced after heating reservoir to a temperature 600 ^{o}C. Working with metallic cesium is not very easy and, therefore, more frequently used binary compound of cesium with carbon, chloride, e.t.a. are more frequently used, which are dissociated at the high temperature and release Cesium atoms. Original studies carried out in the field of surface physics of alkali atoms on tungsten can be traced back to the definitive work by Langmuir [La33].
In the working conditions of a SI source there are three temperature ranges of heating could be discerned. In the low temperature range of the heating (up to T ≈ 600 ^{o}C), the salt breaks down and releases the cesium atoms that then diffuse through the porous tungsten emitter. At the emitter surface, there is a balance between the fast desorption rate and the slower replenishment rate from reservoir by diffusion. At this temperature the high concentration of cesium atoms on the emitter surface highly favors their existence as neutral particles which have a smaller surface affinity with the tungsten than Cesium ions. Therefore, a neutral particle diffusion dominated process is expected. At the mid-range of heating where a sufficient number of alkali atoms have been desorbed so that there starts to appear a significant ion population. The neutral atoms will continue through like in Knudsen-type flow (given that the mean free path of the atoms is much larger than the characteristic dimensions of the pores), being slowed down by the fact that the gas atoms do not elastically bounce off emitter internal surfaces but become adsorbed, spend some time on the surface and then become desorbed again. The ions, on the other hand, due to their binding force to the surface, are limited to slower diffusion speed, as their movement is through surface migration along the grain surfaces. A final stage of heating (T ≈ 1100 ^{o}C) the alkali content is sufficiently low to favor the existence of ions which move by surface diffusion. At this temperature of ionizer the source is fully operational and capable of its higher current yields.
One of the first versions of a negative sputter ion source was made by Middleton [Mi83]. This source has been used for many years for injection into tandem electrostatic accelerators for fundamental nuclear research. His design consists of a sputter target rod and a circular filament enclosed in a common chamber containing cesium vapor. Cesium vapor is introduced into the chamber by heating a cesium reservoir attached to the source body. Cesium is surface ionized on the filament surface and is attracted to the sputter target by a high negative bias.

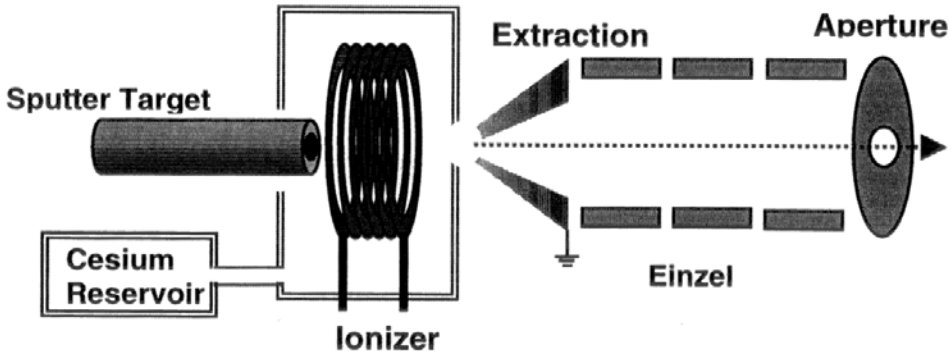

Fig 6.2. Schematic of the cesium Peabody Scientific sputter source.

This construction of the source delivers rather high values of the ion currents for a wide range of materials [Mi83].

A few years ago a model based on this development was built by Peabody Scientific (see fig 3.2).
The Peabody Scientific ion source is commercially available, but unfortunately it has been designed mainly for insertion into the ion column of a Cameca IMS4f SIMS instrument. One of the main drawbacks of this construction is a large cesium flow from the ion source in the operating mode. This leads to rapid contamination of the ion optics of the whole column. For separation of produced ions this ion source utilizes standard magnetic mass separator of the Cameca SIMS instrument included in the primary ion column of instrument. This design of the source also requires differential pumping.
An ion source which could be used in our experiment must have different parameters, suitable for TOF-SIMS/SNMS setup. The source must provide the possibility of separation of the produced ions. One of the main desired features of this source must be the possibility to produce DC currents, which was not allowed to do in our previous design of a cluster ion source based on laser ablation [He00]. In order to perform the desired experimental investigations the temporal width of the projectile ion pulses must be freely selectable within ≥ 100 ns and ≤ 10 μs time range (see chapter 7). Ultimately, it must be possible to get an DC beam for implementation of polyatomic ions produced by the source for sputter erosion in a depth profile. Moreover, as it was stated above negative sputter ion source provides the flexibility with respect to the projectile species (element). This is not the case for other types of ion sources which are able to produce polyatomic ion projectile, for instance, Liquid Metal Ion Gun (LMIG).
It must be also compact and easy to install on the setup.
Therefore, the initial task was to design and develop such an ion source.
During the project two versions of the ion source were designed and tested. In both cases the main criteria taken into account in the development were the simplicity of design, easy operation, and performance.
At the beginning, for production of primary cesium ions it was decided to use a cesium ion source similar to that which was used at Tashkent in our previous investigations [Be98a] of the cluster ion emission under polyatomic ion bombardment. The schematics of the SI source used in both designs are shown on the fig. 6.3.

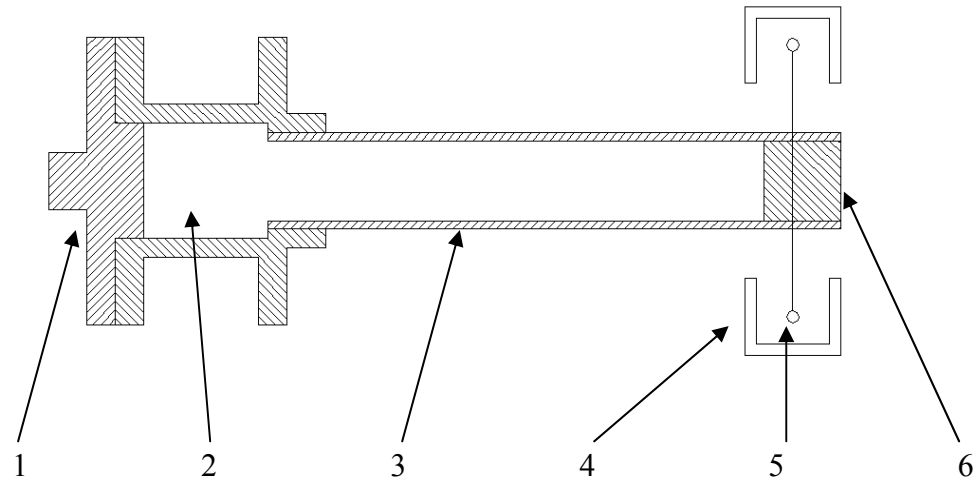

Fig.6.3. Surface ionization ion source:
1 - cover of the reservoir; 2 – reservoir with cesium compound; 3 – tube for Cs vapor transfer; 4 – reflector for electrons; 5 – tungsten wire emitting electrons; 6 – porous tungsten.

The choice of design of SI ion source was based on previous successful experience of working with it. It produces rather large (up to 200 μA) ion currents, and it is very stable

in the operation. The porous tungsten cylinder used in the ionizer was made from tungsten wire of 30 μm diameter which was cleaned in the sulfuric acid, pressed and spot welded to form a cylinder. After that it was fixed to the exit tube of the source. The body of reservoir and its cover were made from molybdenum. The tube connecting reservoir and ionizer is made from Tantalum. The tantalum tube is tightly inserted in the corps of the reservoir and spot welded to it. Cover of the reservoir is fixed to the main part by screws (not shown). For heating of the ionizer electron bombardment was used. Electrons are emitted from tungsten wire of 100 μm diameter and accelerated to the tube by a potential of 800-900 V applied between the filament and the Ta tube. For better efficiency additional reflectors for electrons are used.
In principle, it is also possible to use indirect heating of the ionizer by a tungsten or tantalum coil wrapped around insulating ceramic insulator mounted on the ionizing part of source. In this case the heating scheme is simpler since it is not necessary to supply additional voltage for electron bombardment.
During the projection of the first version of the negative ion source for TOF-SIMS/SNMS setup it was decided to use an ion optics where primary cesium ions would be reflected by the extracting electrode for negative sputtered ions by angle about 150 grad. Such approach was allowed to locate the cesium ion gun behind the sputter target. Schematics of the source is shown on the fig. 6.4.
In this design the cesium ion source was sitting on its own flange independent from other parts of the source. This arrangement allows reloading the cesium source and maintaining it without dismounting the whole source. Another advantage is that sputter target and first einzel lens for negative ions could be designed as single assembly and therefore could be easier to align to the main axis of the source.

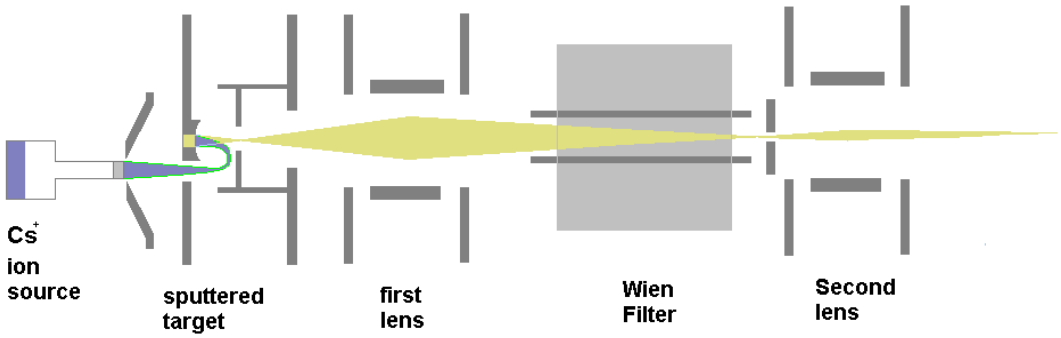

Fig. 6.4. Schematics of the first version of the source.

The design of the cesium ion source utilizes a quasi Pierce electrode for focusing the cesium beam. Cesium beam is passing through the hole on the plate holding the sputter target and is reflected by the extracting electrode having positive potential with respect to the cesium ion source. Negative ions sputtered from the target are confined and focused by a spherical electric field formed by the shape of the target. They are focused onto the first slit in the extracting electrode. This slit is the source for the first einzel lens (condenser) which is producing the image on the second slit at the exit of the Wien Filter used for mass separation. Ions of the desired mass having straight trajectory are passing through the second slit and are than focused by the second einzel lens (objective) and aligned by a set of deflection plates before they impinge onto the sample.

6.3.2 SIMION's simulations of the first version

The software package SIMION 3D 7.0 has been used to model the negative sputter ion source before it was developed and built. SIMION makes use of potential arrays that define the geometry and potentials of electrodes and magnetic poles. The potentials of points outside electrodes and poles are determined by solving the Laplace equation by finite difference methods. Refined arrays can then be projected as array instances *(3D Virtual Images)* into an ion optics workbench volume. Ions can be placed within the workbench volume with selectable initial velocity and their trajectories changed by the fields of the potential array instances they pass through are calculated.
For the simulations there are two types of potential arrays which can be used: 3 and 2 dimensional. 2D potential arrays are used where ion optics has an axial or planar symmetry. Arrays of both types were used in the simulations of the ion source.
Virtual ion optics components (called „instances") were assembled together on a SIMION workbench. Ion trajectories through each component were then calculated. Some components were identical, and corresponding potential arrays were used twice to save computer memory. There are 13 „instances" written and 11 unique potential arrays. In order to correctly define boundary of electric fields, areas where the cylindrical elements (lenses) were interacting with the planar elements (Wien Filter plates) were simulated using three dimensional (3D) potential arrays.
Initially, the emission part which consists of the cesium ion source, sputter target, extracting electrode of the sputter ion source was simulated. For this simulation 3D potential array was used, since this part is not axially symmetric. Energy distributions of ions of both types (evaporated and sputtered) were approximately taken into account. The 3D image of simulated part is shown on the fig 6.5.

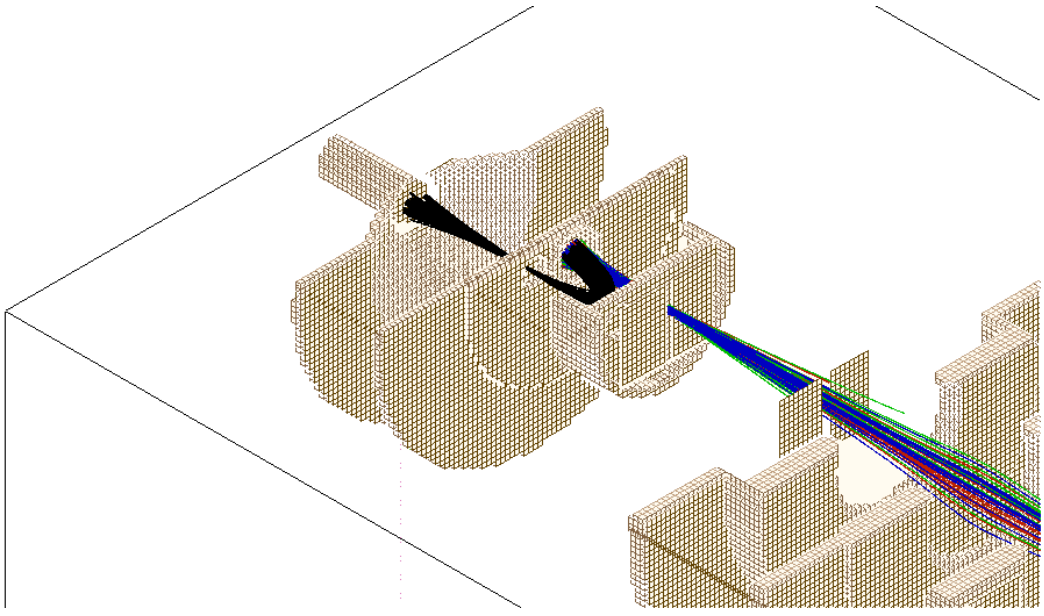

Fig.6.5. SIMION 3D 7.0 simulation of ion trajectories in the emissioning part of the source.

In fig 6.5 trajectories of cesium ions are shown as black lines and trajectories of the sputtered negative ions with different masses as color lines. It is clearly seen from the picture that cesium ion beam has the focus exactly at the position of the hole. Sputtered

ions have nearly the same trajectories. Au_m^- (m=1÷3) ions focused on the first slit and size of the beam at the focus is about 2 mm. Part of the beam is cut-off by this slit. Trajectories of sputtered ions are identical and independent on their masses at this part of ion source column. After first slit there are used additional diaphragm cutting the beam in order to make it paraxial for the first lens.
The position of the Cesium beam could be varied by changing the potential of the extracting electrode (fig 6.6).

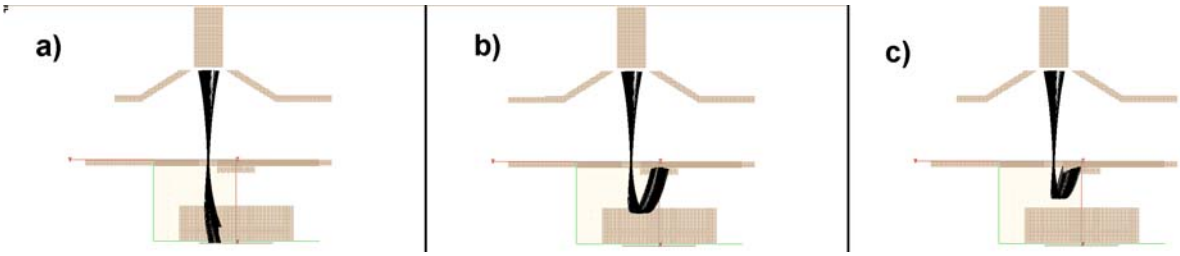

Fig. 6.6. Trajectories of the cesium beam at the different potential of the extracting electrode $U_{extr.}$;
a) $U_{extr} = 0$, b) U_{extr}=3 kV, c) U_{extr}= 7kV

The results of simulations shown on fig 3.6 were obtained for a potential of target U_{tar} = – 7kV and a grounded cesium source. From the picture it is clearly seen that the grounded extracting electrode does not reflect the cesium beam and when both potentials are equal the cesium beam is hitting only the edge of the sputter target. Optimal position of the cesium beam is obtained when the potential of the extracting electrode is 3 kV. This potential must be scaled with the potential of the sputter target and, therefore, a certain ratio between absolute values of U_{extr}/U_{tar} must be chosen for optimal ion current output from the source. These simulations are in the good agreement with the real optimal values of the voltages applied to the source during operation.
Simulation of the complete design is shown in fig.6.7.

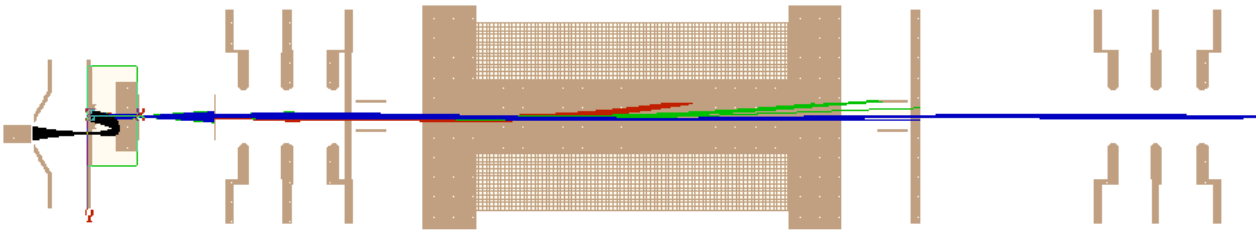

Fig. 6.7. SIMION 3D 7.0 workbench with all instances (potential arrays).

Negative species passed through slit are focused by the first einzel lens and directed to the Wien Filter for separation. The focus of the first einzel lens is at the slit at the exit of the Wien Filter.
On the picture is shown how ions with different masses multiple to 197 amu (gold) and having kinetic a energy 7 keV are separated in the Wien Filter. Red lines correspond to monoatomic gold, green to the gold dimer and blue for trimer of gold.
The magnetic field strength used in the simulations is 1 Tesla. The length of the Wien Filter is 10 cm. From the figure it is seen that all three types of ions are separated from each other by the filter.

Potential on the first lens is of the same polarity and about 70% of the potential on the sputter target.
SIMION is not a magnetic circuit program. Simulation of the magnetic field in the SIMION is simulated using a scalar magnetic potential.

6.3.3 First version of the ion gun

On the basis of SIMION calculations, the first version of the source was projected in the AutoCAD14 system and built. Gold foil was installed as the sputter target. Gold was chosen due to its monomisotopic nature, large atomic mass, and great efficiency of negative ionization under cesium bombardment.
During operation, a DC current of 6-7 A was passed through the tungsten wire for heating filament. It was emitting an electron current of 20 mA. It was emitting the current of electrons at the value about 20 mA. With an accelaration voltage between wire and bombarded ionizer of 900 V, the power delivered by electrons to ionizer was about 18 W. In addition, tungsten filament itself consumed power about 20 W.
.

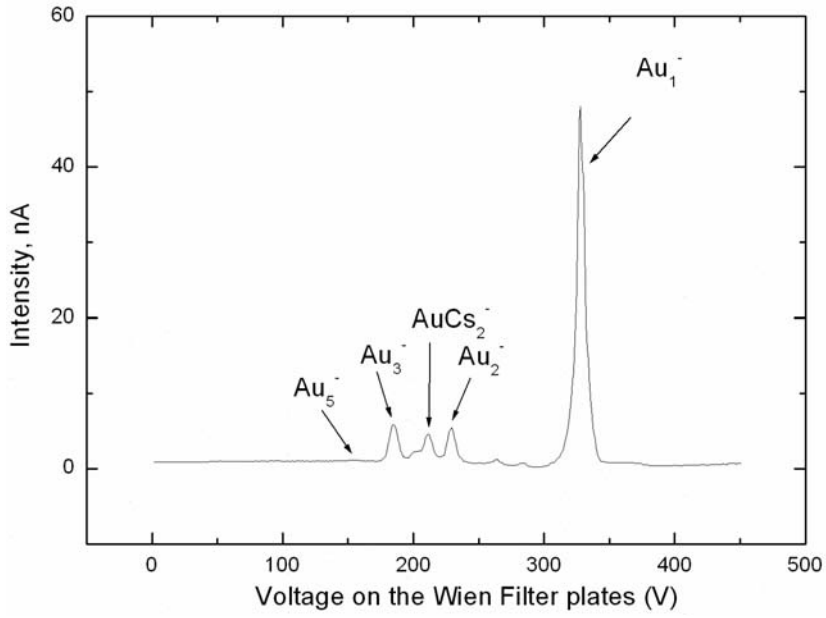

Fig. 6.8. Primary ions spectra.

All insulators were made from commercially available alumina oxide ceramic tubes.
Mass-spectra of produced gold ions in dependence on the Wien filter plates voltage is shown on the fig. 6.8.
Primary currents for monomer of gold at the value 50 nA were achieved at the current of Cs^+ ions of 65 μA. The intensity of gold dimer and gold trimer were at the order of magnitude lower.
It is interesting to note of presence in the spectra heterogeneous clusters containing gold and two cesium atoms. Such clusters may be of interest for surface analysis by SIMS technique. Bombarding by this this kind of particles allows using advantages of polyatomic ion sputtering simultaneously with delivering chemically reactive atoms of cesium and, therefore, increasing the efficiency of negative ion production.
One of the drawbacks of this construction was related to failure of sputter target insulators. This was the most critical part. During operation they must sustain high

voltage in the presence of corrosive cesium vapor. It was noticed that after few days of operation leak currents in the range of few μA were appearing slowly leading to the arcing. Some modifications were made in the cathode-lens assembly to solve the problem. Special shields were installed close to ceramic insulators from cesium vaporization, the length of the insulators was increased from 22 mm to 35 mm, but these efforts only prolonged the „life“ time of insulators. Another disadvantage was that for cleaning these insulators a dismounting of the whole ion gun was required.
From the SIMION simulations in fig. 6.5 it is seen that the diameter of the cesium beam is only two times smaller than the size of the target. Simulations show that in this design it was not possible to reduce the cesium beam spot size due to inhomogeneous field of the extractor where the reflection occurs. The real size of the cesium beam is nearly the same as it was predicted by SIMION. The size of the cesium beam was determined from sputter erosion of the target.
To increase the current density from the ion source it is desirable to reduce the size of the cesium ion beam on the sputter target. Which could be achieved only by implementation of new ion optical design.
The procedure of working with the ion source is beginning from applying all voltages to the source electrodes (sputter target, lenses, Wien Filter plates, deflection plates, etc). After that the current source for the tungsten wire is switched on at its minimum value. Increasing the current through the wire, the electron current for ionizer heating must appear. Warming up of ionizer is performed in two to three steps during 10 minutes until working parameters of heater are achieved (usually 20 mA of electron current).
For alignment of the source, the second slit at the exit of the Wien filter can be used. This slit is constructively isolated from body of the source and therefore the current onto it can be measured. After ion current on the slit is detected at some value of the voltages on the first lens and Wien filter plates, the next step is the optimization of the ion current on the sample. Optimization on the absolute value of the ion current on the sample is a rather complex procedure which can include iterative alignment of all ion optics together. This procedure must begin with alignment of the potential on the first lens together with voltage on the Wien filter. After that the second lens with deflection plates must be optimized. When the ion current is adjusted to its maximum value, current measured on the second slit must be less than the one on the sample. At this point playing with potentials on the Wien filter plates must show two peaks of the ion current of monomers on the slit. The local minimum in the middle corresponds to the maximum value of ion current on the sample. An additional alignment may be performed by the precise positioning of permanent magnets of the Wien filter in direction perpendicular to the axis of the source. Optimal position corresponding to the maximal value of ion current and highest resolution may be found when magnets are slightly displaced from middle. This may be explained in the way that inhomogeneous magnetic field may additionally focus the ion beam.
Another critical part of the design – is the alignment of the Cs ions source directly opposite to the hole in the sputter target plate.
During operation the ion source may by degassing, especially after reloading new cesium salt. Degassing is usually slowly increasing during operation and it is related to the warming chamber of the source. After one hour operation temperature of the ion source body closely to Cs source may be 60^{o}C and pressure may increase up to 2×10^{-7} mbar.

6.3.4 Permanent Magnets

Separation of different projectile ions in the source is performed by the Wien filter at their desired total impact energies. There was no commercially available Wien filter with required parameters. Therefore, a custom built Wien filter was used in the source.
Choice of a Wien filter as a separator for primary ions was made due to the following advantages. A Wien filter has rectilinear construction which simplifies the building of the ion column. Using strong permanent magnets it is possible to make compact Wien filter for separation of heavy ions at energies more than 10 keV. It is possible to separate ion beam of DC current. Wien filter is also called as velocity filter; it can be called as ExB filter.
In the Wien filter a magnetic field and a electrostatic field are placed orthogonal to each other and to the particles direction through the system. The magnetic field influences the particles with a force of $F = qvB_0$ and the electric field influence with $F = qE$. These forces are directed opposite to each other. To receive a beam that travels straight through the system the two equations are combined, which gives

$$v = \frac{E}{B_0} \qquad (6.1)$$

With this setup the velocity of the particles is chosen by the two parameters E and B_0. In the ion source produced clusters separated by the Wien filter have equal kinetic energy $e \cdot U_0$ with but with different masses M. From Eq. (6.1) one may get:

$$\frac{eU_0}{M} \approx 4.9 \times 10^3 \left(\frac{E}{B_0} \right)^2 \qquad (6.2)$$

where eU_0 in eV, M in amu, E in V/cm and B_0 in gauss are measured.
In Eq. (6.2) that at fixed U_0 and B_0 mass of the ions at straight trajectory have quadratic dependence on electrical field E of the Wien filter.
For ions with kinetic energy eU_0 and mass M effective radius in the homogenous magnetic field B_0 can be written as:

$$r = \frac{1.4395 x 10^2}{|B_0|} \left(\frac{MU_0}{e} \right)^{\frac{1}{2}} \qquad (6.3)$$

where r in cm;
Ratio of effective length to radius of the Wien filter determines its focusing and its resolution. Dispersion factor of Wien filter in the case of homogenous fields:

$$D = \frac{1}{2} \sin\left(\frac{L}{r_0} \right) \qquad (6.4)$$

where L is a length of the Wien filter

The perpendicular distance Δx of a dispersed beam from the axis in the image point is:

$$\Delta x = D_M \left(\frac{\Delta M}{M} \right) \qquad (6.5)$$

from last equation the resolution may be derived as:

$$\frac{M}{\Delta M} = \frac{D_M}{\Delta x} \qquad (6.6)$$

Here Δx must be some characteristic distance which must be determined by the slit width at the exit of the Wien filter and by beam spot size. One approach to improve the resolution is to increase dispersion factor (Eq. 6.4). Length of the Wien filter is limited constructively. Another way to improve the dispersion D in the range of masses and energies of ions produced by the source is to reduce r_0 and therefore to increase magnetic field.
Residual field strength of the strongest permanent magnet material is at a level of 1.3 Tesla (NdFeBr material). In most cases, the magnetic field strength made by these materials is a half of the residual filed.
Increase of the magnetic field is possible using the magnetic compression mechanism [Ku93].
Klaus Halbach invented a novel configuration using a Rare Earth Cobalt magnet material which he called REC magnet. In his magnetic circuit, the direction of the magnet is rotated along a circular ring. On the basis of this idea Kumada and others developed compact dipole magnet for medical accelerator with the field strength 4.45 Tesla.

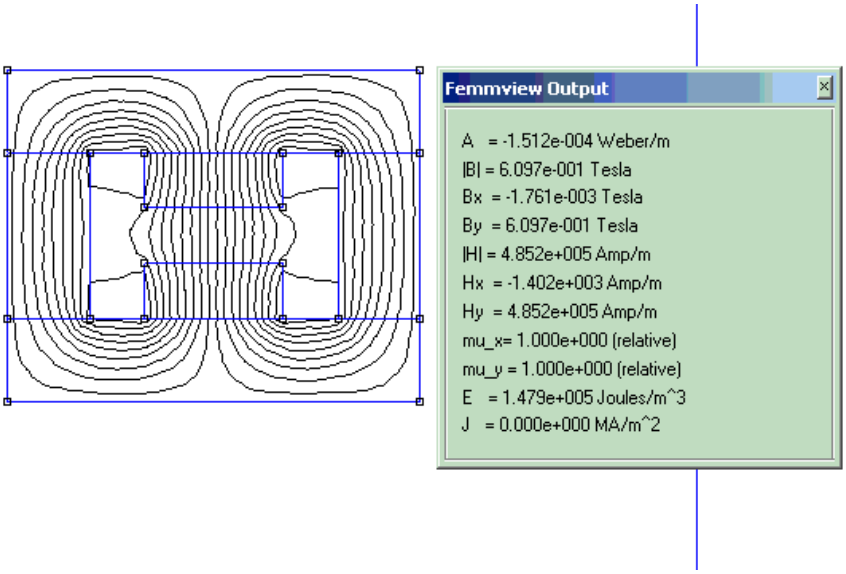

Fig 6.9 FEMM calculations of the magnetic field in the first design of permanent magnets

To project permanent magnets for the Wien Filter a suite of programs FEMM 3.1 was used. FEMM uses finite element analysis to solve Maxwell equations for the systems containing materials with different magnetic properties (permanent magnets, iron, air, etc). Program solves the problem in two dimensional case.
In the fig. 6.9 is shown „classical“ magnetic circuit solved by FEMM. Two permanent magnets with thickness 2 cm and perpendicular direction of magnetization are surrounded by circular iron conductor. In simulation NdFeBr permanent magnetic material was used.

From the picture it is seen that magnetic field with the value of 6 kGs in the space 2 cm is reachable using „classical“ scheme of magnetic circuit. 6 kGs is the half of residual magnetization of NdFeBr magnets. In order to increase magnetic field the idea of circular compression was used [Ku93]. In FEMM new design had been projected where 4 NdFeBr magnets with direction of magnetization of 30 degree are installed opposite each other and surrounded by iron conductor fig. 6.10.

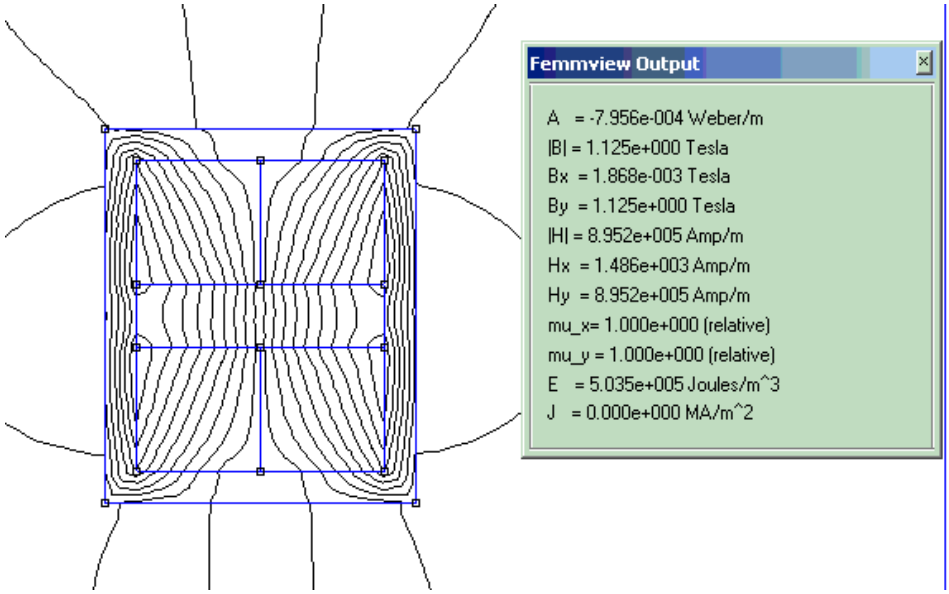

Fig 6.10 FEMM calculations of the magnetic field in the second design of permanent magnets

In the new design magnetic field 1.1 Tesla was predicted by FEMM. In reality field with strength about 1 Tesla was achieved. Permanent magnets were custom ordered at the EUROMAG firm. Implementation of the new magnets assembly allowed significantly improve resolution of mass filter in the source.

6.3.5 SIMION simulations of the second version

The above mentioned drawbacks in the first design of the ion source led to the necessity of improvements in the construction. The most critical part was the insulator for the sputter target and all possibilities to enforce this part in the first design were exhausted. Therefore some principal changes in the emission part of the source had to be made.
The new emissioning part of the source was projected implementing the following desired constructive features: the sputter target (cathode) must be easily changed and fixed without the necessity to dismount the whole ion source, the target assembly must contain several targets for fast and easy change them during operation, reliable shielding of the sputter target insulator from cesium vaporization, improved ion optics for the primary cesium ion beam allowing to reduce the diameter of the sputter spot on the cathode and therefore increase the density of produced ion beam.
The idea of the new ion optics is similar to the one developed by Middleton [Mi83]. In the new design the cesium ion source is placed in the front of the sputter target. SIMION simulations showed optimal focusing both for primary cesium and for sputtered negative ions is shown in fig 6.11.

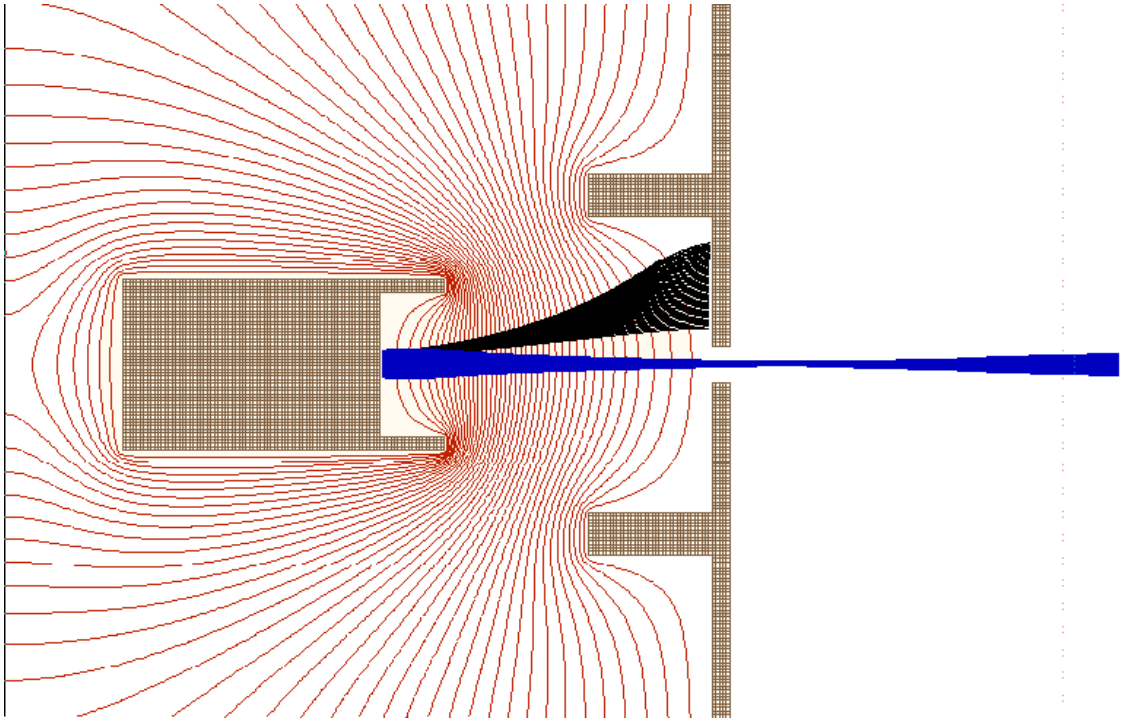

Fig. 6.11 SIMION 7.0 3D simulation of ion optics for the second version of ion source.

On the fig. 6.11 red lines are representing equipotential lines. Black lines are trajectories of cesium ions and blue ones are sputtered negative ions (mass 197 amu, initial energy spread ≈ 5 eV). The accelerating voltage is 10 kV.
Initial kinetic energy of produced ion leads to large focus spot of the beam in the crossover.

6.3.6 Second version of the source

In the new design there are three sputter targets installed on a rotating platform. The rotation is transferred through a feedthrough on the flange. With these modifications, it is possible rapidly to change the target and, hence the type of ions within seconds during operation.
The length of the cathode insulator is prolonged to 70 mm and shielded by a sheet metal screen from cesium. As a consequence, a several weeks of intensive exploitation did not produce any leak current across cathode insulator. In addition, operation and maintenance (reloading of cesium, changing targets, etc) of the sputter source is easier with the new design.
In the new design the same type of cesium ion source was used. The only difference is that the tantalum tube which is used as a vapor conductor of the Cs vapor was bent by 90 degrees. Moreover, the whole cesium source is closed in a stainless steel box to reduce contamination of the first lens insulators.
Innovative improvements were utilized in the design of the cesium ionizer. Due to the fact that the design of the cesium ion source is stricter in the space dimensions as compared to the first version, it was decided to refuse from heating by electron bombardment. The new ionizer is made from a thick tungsten wire (∅ 300 μ) with 5 cm length which is insulated by tiny ceramic tubes with outer diameter ∅.7 mm cut into 4 mm pieces. The tungsten wire is bent to form dense bunch which is insulated by ceramic tubes and then it is tightly installed in the place of porous tungsten material used in the previous design. Our

experience in the routine use has shown that the new design of ionizer does produce the same performance as the old construction and, moreover, has additional advantages like lower power consumption at the same produced cesium ion currents in combination with simpler power supply circuit, since it does not requires an additional HV power supply to accelerate electrons. During operation producing a cesium current of 100 μA, the ionizer was consuming a power of 5.4x4 = 21.6 W which is nearly a factor of two lower in comparison with the previous design. The higher efficiency can be explained by the fact that in the latest design the ionizer and heater were higher are combined more closely together. Therefore the working temperature of the ionizer can be maintained at greatly reduced electrical heating power. The only drawback in the current design of the ionizer is that its surface has a roughness of about 1 mm. However, simulations performed with SIMION proved that in the current design of the ion optics the influence of this roughness influence on the cesium ion trajectories is negligible.

Good performance of the ion source means the productions of the ion beam with the high value of the brightness having small solid angle extension. The only possibility to increase brightness of the beam is to reduce the area from which beam is issuing, or in other words to reduce the cross-section of the cesium beam at the sputter target, if the Cs^+ current and beam energy are not to be changed.

After operation of the source the erosion craters on the target show that the Cs^+ beam spot size on the target has the dimensions of 2.4 and 1.4 mm with area 3.3 mm^2 which is much lower in comparison with previous model of the source having sputter area ≈ 9 mm^2.

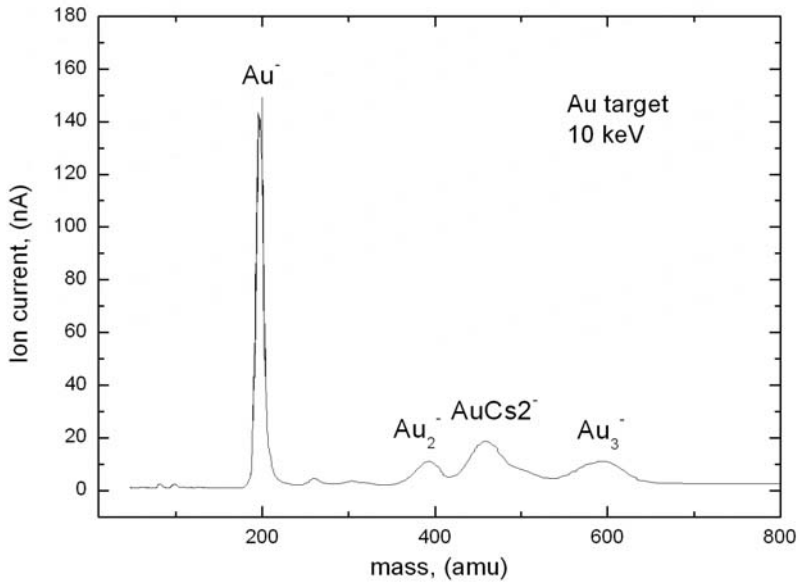

Fig. 6.12. Spectrum of Au_m^- ($m=1\div3$) negative ions.

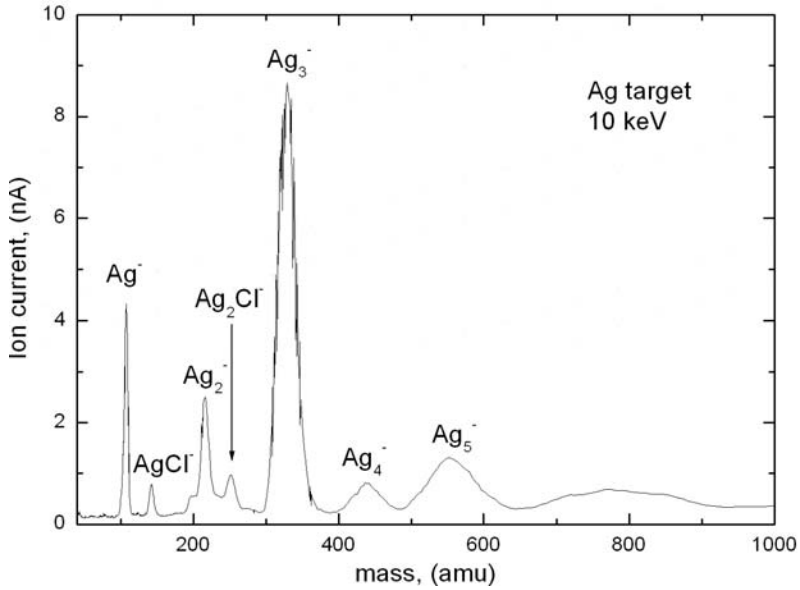

Fig. 6.13. Spectrum of Ag_m^- ($m=1\div5$) negative ions.

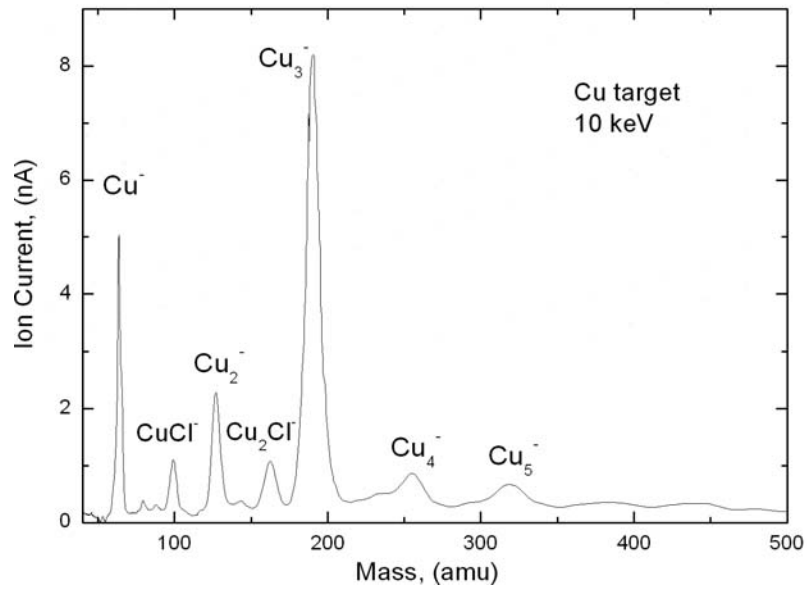

Fig. 6.14. Spectrum of Cu_m^- ($m=1\div5$) negative ions.

Like in the design of the first version of the source there are used two slits in the ion column. The first slit is placed at the crossover of the sputtered ions (fig. 6.11). This diaphragm determines the source size of the beam and it has a size of 0.4 mm. The second slit is placed at a distance 19 mm after the first one and has a size 3 mm. The second slit restricts the emittance of the beam to 0,2 $mm \cdot \pi \cdot rad$. These beam properties were required to achieve the following conditions. The first is to ensure that the first electrostatic (decelerating) lens is filled to less than 30% of its diameter (14 mm) in order to reduce its aberrations. The second is that source size of the beam must be less than 0.5 mm in order to be focused on the exit slit of the Wien filter. The current density achievable gold atomic ions at the sample is 15 μA/cm^2.

The ratio of the produced currents of gold atomic ions measured on the sample to the cesium ion current onto the gold target in the ion source was determined as more than 1/300 which is much better than the 1/1000 ratio measured with the first design .

In the target holder of the source three types of target (gold, silver, copper) have been loaded. In the fig. 6.12, 6.13 and 6.14 the spectra of gold, silver and copper negative ions produced at the Cs^+ current of 60 μA are shown. Like of gold projectiles copper and silver negative ions show strong odd-even alternations. The intensity of atomic ions in the case of copper and silver targets is significantly lower in comparison with gold target. Though the yields of triatomic projectiles are at the same order of magnitude, the intensity of silver and copper ions is 13 and 12 times less in comparison with the intensity of the gold atomic ions. Appearance of Ag and Cu heteroclusters containing chloride may be explained by Cl flooding from cesium ion source which uses CsCl salt.
These data can be compared to published data on secondary ion yields that have been measured under Cs^+ ion bombardment. As an example, the results of Storms obtained for a Cs impact energy 10.5 keV are depicted in fig. 6.15 [St77].

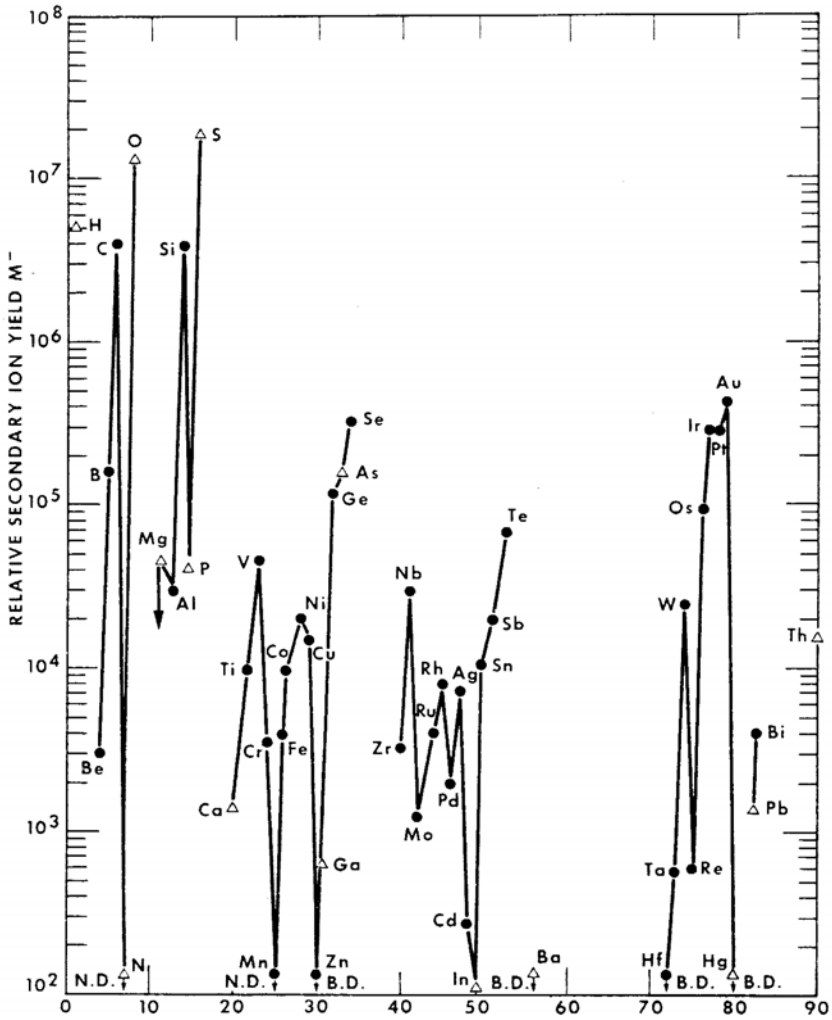

Fig.6.15. Relative negative yields for 16.5 keV Cs^+, ϕ=0°. From Storms et al. [St77.]

In their results the ratio between intensity of the gold and silver ions is two orders of magnitude.
On the other hand, the data sheet from Peabody scientific on their PS-120 Negative Sputter Ion Source which is reproduced in table 6.1 shows ratio between gold and silver ions of only factor 2. Between gold and copper ions this factor is about 3.

Ion Species	Beam Current (microamps)
H	200
Li	1
B	80
C	350
O	200
Al	10
Si	400
P	40
S	100
Cl	100
Fe	20
Ni	60
Cu	60
Ag	100
Cs	1
Pt	100
Au	225

Table. 6.1. Beam performance of the PS-120 Negative Sputter Ion Source from Peabody scientific at the primary ion current 8 mA.

In order to discuss the possible reason for this
In the works [No87] and [Lu78] there is proposed the model of ionization for negative ions in which it described by equation

$$\alpha^{+} \propto \exp\left(-\left(\varphi - A_e\right)/\varepsilon_n\right) \qquad (6.7)$$

where A_e is the electron affinity, φ the work function of the emitting surface, and ε_n - is a characteristic energy depending on the particular model description employed. Possible interpretations of ε_n may be include energies of local equilibrium (thermal) or non-equilibrium electronic excitation as well as quantum mechanical non-adiabatic passage, electron tunneling, etc.
From this equation its clear that a reduce of the work function φ , including one by means of alkali metal adsorption on the surface, must lead to a significant increase of negative ionization efficiency. In fact, this is the reason why cesium ions are often used as projectiles in practical surface analysis application using negative secondary ions.
The difference between results on the efficiency in the ionization of silver atoms in comparison with gold ones obtained by Storms and ratios produced from the ion source may be explained by different concentration of the cesium on the surface and , therefore, the value of the workfunction φ. The equilibrium concentration of the cesium on the metal surface in the case of cesium irradiation under high vacuum conditions depends on the sputtering rate of the metal. In the conditions of sputter negative ion source, in addition to that, the sputtered target may be strongly flooded by the neutral cesium evaporated from cesium source.
In the following an estimation of changes in the ionization probabilities of Ag and Cu atoms relative to Au atoms using equation (6.7) is performed.

In the dynamic equilibrium conditions of sputtering process the primary flux of Cs^+ ions in addition with flux of Cs neutrals is equal to the sputtered flux of Cs from uppermost layer of the surface:

$$j_p + j_{dep} = Y_{Cs} \cdot j_p = C_{Cs} \cdot Y_{tot} \cdot j_p \qquad (6.8)$$

here j_p flux of Cs^+ ions, j_{dep} flux of Cs neutrals, Y_{Cs} partial sputtering yield of Cs, C_{Cs} concentration of Cs on the surface, Y_{tot} total sputtering yield from the surface.

From Eq. (6.8) concentration of the cesium is derived as

$$C_{Cs} = \frac{1 + j_{dep} / j_p}{Y_{tot}} \qquad (6.9)$$

if we assume $j_{dep} << j_p$, Eq. (6.9) transforms to

$$C_{Cs} = \frac{1}{Y_{tot}} \qquad (6.10)$$

Sputtering yields Y_{tot} may be obtained from computer simulation using program SRIM. For 90^0 degrees incident angle with energy 10 keV sputtering by Cs projectiles SRIM predicts the following sputtering yields: 16.9, 9.5, 8.2 for Au, Ag and Cu respectively.

From Eq. (6.10) and dependence of the change of the work function $\Delta\varphi$ on the cesium concentration [St93] the following $\Delta\varphi$ for Au –0.55 eV, Ag –1 eV, and Cu –1.2 eV are obtained.

From [Be87] parameter ε_n is estimated to be 0.26, 0.25, 0.24 eV for Au, Ag, and Cu respectively.

where E_b is binding energy of the surface, *m* is atomic mass of ion.

From Eq. (6.7) and (6.11), using estimated data on $\Delta\varphi$ one can calculate ratio between the ionization probabilities in the case, for instance, of gold and silver cesium bombardment:

$$\frac{\alpha^-_{Au}}{\alpha^-_{Ag}} \cong \exp\left(-\frac{\left(\varphi_{Au} - \Delta\varphi_{Au} - A_{Au}\right)}{\varepsilon_n(Au)} + \frac{\left(\varphi_{Ag} - \Delta\varphi_{Ag} - A_{Ag}\right)}{\varepsilon_n(Ag)} \right) \qquad (6.12)$$

The following ratios: 11 for $\frac{\alpha^-_{Au}}{\alpha^-_{Ag}}$ and 3.3 for $\frac{\alpha^-_{Au}}{\alpha^-_{Cu}}$ have been obtained. For Ag target the obtained ratio is in the good agreement with experimental ratio measured from the source, though for Cu theory predicts ratio by factor about 3 higher.

In order to estimate how neutral cesium flooding from an Cs ion source may change an ion yields (rations), we can assume that Cs ion and neutral flows are equal. Using Eq. (6.9) and data from [St93] we the following $\Delta\varphi$ for Au –1.4. eV, Ag –2.2 eV, and Cu –2.4 eV are obtained. Evaluation of $\frac{\alpha^-_{Au}}{\alpha^-_{Ag}}$ and $\frac{\alpha^-_{Au}}{\alpha^-_{Cu}}$ in this case produce the 2.8 and 2.25 respectively. These ratios are in the good agreement with data from Peabody (Table 6.1). As it was described earlier, in their design of ion source sputter target is exposed to the strong flooding of Cs vapor (fig. 6.2).

Therefore, to improve the yields of negative ions is desirable to produce a high vapor pressure of Cs at the sputter target.

6.3.7 Comparison with other designs

The performance of the second model of the source designed in this work relative the ion source used in the initial SIMS measurement [Be92] described in chapter 3 has been significantly improved. In the current design at the comparable cesium beam current the current density of produced gold ions is 750 times higher with the increase of the total gold ion current of 7 times. In the design of the source used for the SIMS measurements, both extraction and incident sputtering by cesium ions was occurring at the angles 45°. Extraction of the produced negative ions was performed by a relatively weak field generated by extraction potential of only 500 V. This results in significant losses during the collection of the ions due to their angular and initial energy spread. All these problems are greatly improved in the current version of the source.
At the moment there are two existing, commercially available models of a negative sputter ion gun, both being specially designed as an addition for Cameca IMS-4f SIMS instruments.
The first design from Peabody Sci. (model PS-120) which has already been mentioned. This ion source is intended to replace duoplasmatron originally fitted to the instrument on a flange with implemented differential pumping. Due to its open construction, this source allows to generate a relatively high current of the sputtering cesium beam up to about 8 mA. According to the specifications an Au^- current of 225 μA can be generated, the efficiency of Au^- production under these conditions being around 3% Au^-/Cs^+. It is important to note that this value refers to the total extracted ion current without any mass filtering! In comparison, we obtain an efficiency of about 0.3% after mass separation.
The following parameters of the power supplies are required:

Target	15 kV	15.0 mA
Cesium Reservoir	110 V	2.5 A
Ionizer	18 V	36.0 A
Reservoir Tube	110 V	1.5 A

In total several hundreds Watts are consumed during the operation of this gun. The high thermal load connected with this power evidently leads to the necessity of a stage with differential pumping. In contrast, the improved version of the ionizer used in the second version consumes only 20 Watts at the cesium current of 100 μA leads only to a slight warming of the container of the source after several hours of operation. Though, higher values of primary ion beam currents are achieved (Table 6.1) in the source of Peabody Scientific. According to G.Gillen [Gi00] they observe beam diameters of over 1 inch at the input aperture to the primary mass filter of the SIMS instrument. Therefore, for instance, for gold primary ions according to table 6.1 they must have primary ion current density about 50 $\mu A/cm^2$.
Another design of the ion gun is made by S.Belykh et al [Be01a]. This design is based on the cone construction of R.Middleton [Mi77]. It utilizes the same construction of the cesium source as in our source and therefore they may use Cs^+ current up to 200 μA. The advantage of their design that it has axial symmetry. In this design, the crossover of the source is determined by the diameter of the hole in the cathode cone. Secondary negative ions sputtered inside the cone are extracted through the hole by a penetrating extraction

field. The strength of this field must be rather weak and , therefore, strong discrimination in the collection of secondary ions due to their initial sputter energy spread must be observed, especially for monoatomic ones. Constructively this source is also designed to replace a duoplasmatron on a Cameca instrument.
The achievable Cesium current in our design and that of S.F. Belykh & al. is fundamentally constrained by Child's law:

$$I \propto V^{3/2} \qquad (6.13)$$

where V is extracting voltage.
This restriction only applies when the space charge of Cs^+ became to be comparable with the electric field near the ionizer. For this reason, the Cs ions cannot be both intense and well focused. The fact that the Cs^+ ions originate from a space charge cloud rather than a well defined ionizer surface leads to blurring of the Cs^+ beam focus on the target (as compared to the SIMION simulations). To prove that ion current limited by the space charge dependence of the current on the cathode voltage was measured and shown on the fig. 6.16.

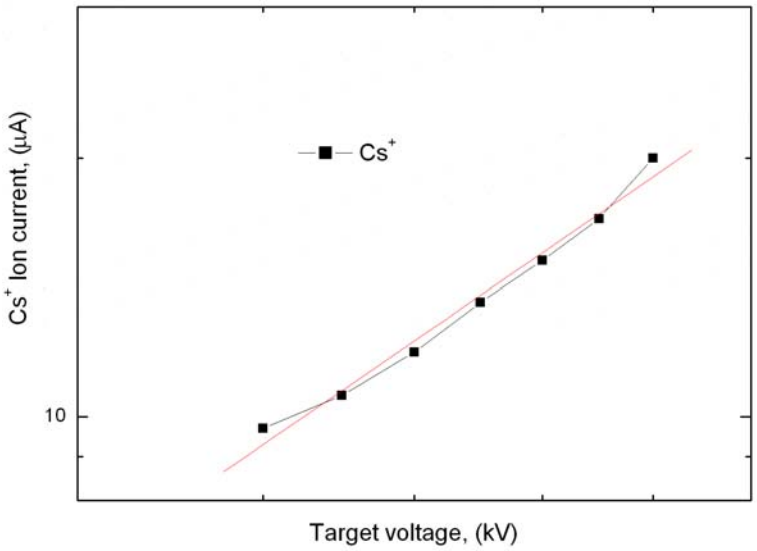

Fig. 6.16. Dependence of the Cesium ion current on the cathode voltage.

The graph is plotted in the double logarithmic scale and is curve is well fitted by the power law dependence with the exponent equal to 1.52.
To overcome this problem, further improvements in the design of the ionizer may be desirable. For instance, the implementation of the ionizer with larger area of the working surface and having axial symmetry must lead to better performance, since the higher values of the Cesium current may be produced at the fine focusing spot on the sputter target.

6.4 Duoplasmatron

During some of the experiments, a high current duoplasmatron ion source was used to clean the sample and for alignment of the ion column of mass spectrometer.

The ion source DUOXe-2000 HC (DUOXe in the following) is a cold cathode duoplasmatron ion source suitable for a variety of physical applications where the source is required to generate high current beams of ions, in particular of Xe^+.
The source features high brightness, high total extracted ion current, low gas load and low power consumption.
The source is powered by DUOXe controller, a solid state voltage converter with control features for operation with other system components.
During my term of usage of this source it has been modified to work in the pulsing mode with ion current pulse length between 10μs and affinity.

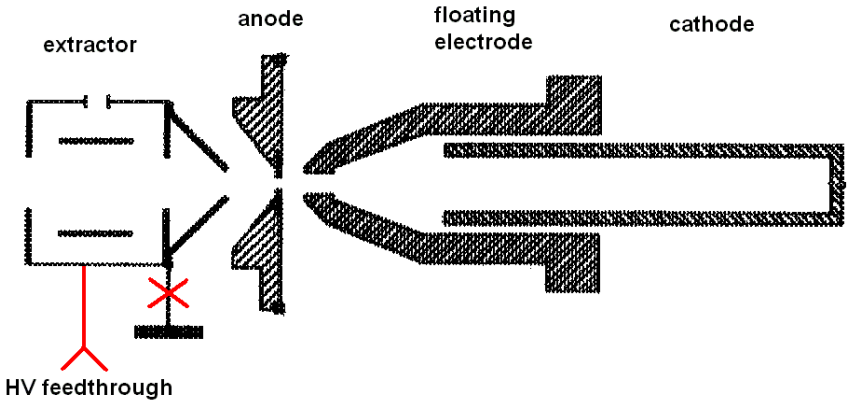

Fig.6.17. Schematics of duoplasmatron.

For that purpose, the extractor electrode located behind the plasma container was constructively disconnected from the ground potential and one additional high voltage feedthrough was added for applying potential to this electrode. In fig. 6.17 added feedthrough is shown as red wire. Pulsing of the extractor ion beam is realized using fast high voltage switch. The switch is able to connect the extractor to the ground and in this mode ions are accelerated and extracted into the space between anode and extractor. When the high voltage switch is disconnected, the extractor is floating and quickly charged to the potential of the anode, therefore, the ion current from source is shut off. The ability to work with duoplasmatron ion source in the pulsing mode was desirable since it produces large currents (≈100μA), which removes a lot of material from the sample. During alignment of mass spectrometer using this source it was operating in the pulsing mode.

6.5 Sample

A polycrystalline indium foil with purity of 99.95% was cleaned in isopropanol solute before installation into the high vacuum chamber as sample. Before measurements, the sample was cleaned by Xe^+ DC current ion bombardment with energy 6 keV and current density 100μA/cm^2 during few minutes.

6.6 UV-Lasersystem

For photoionization of investigated sputtered neutral species emerging from the sample surface, an ultraviolet laser beam generated commercial Excimerlaser (Lambda Physik,

LPX 120i) was used. The laser was operated at a wavelength of 193 nm corresponding to a photon energy of 6.4 eV. This energy is larger than the ionization energy of indium atoms (5.79 eV) and all indium clusters (St02) and, hence, suitable for non-resonant single photon ionization of all sputtered species. To transport the beam the laser beam was passing optical elements (diaphragms, lens) for beam shape formation and focusing before it was directed into the vacuum chamber. First of all the laser beam is cut-off by a rectangular aperture with dimensions 8x25mm. This aperture cut off about half of the outcoming power. It is used to limit geometrical dimensions of the beam in its diameter for the following lens. These diaphragms cut-off about half power of the outcoming power. After limiting aperture the beams passes through a variable attenuator driven by a stepping-motor controlled from PC. Before entering the UHV chamber through a CaF_2 window (transmission 65%), the beam is focused by a CaF_2 lens (∅50mm) with an effective focal length of 22 cm.
In the laser is implemented NovaTube^{TM} innovation. The essence of NovaTube^{TM} is the elimination of contamination effects through careful design and material optimization. All laser tube components are assembled in a clean-room. Optimized electrode materials combined with an improved preionization scheme lead to minimum erosion of the electrodes.
The active medium of an excimer laser is a mixture of rare gas, a halogen and a buffer gas. The gases are mixed in the laser itself.
In principle, it is possible to operate the LPX® at up to five different wavelengths (157, 193, 248 and 351 nm). There are the following mixtures for the different wavelengths: Ar, He, F_2 and Buffer (Ne) for 193nm; Kr, He, F_2 and Buffer (Ne) for 248 nm; Xe, He, HCl, H_2 and buffer (Ne) for 308 nm; Xe, He, F_2 and Buffer (Ne) for 351 nm; F_2, He and Buffer (He) for 157 nm.
The working principle of the laser is based on the formation of excited molecules such as ArF^*, KrF^* and F_2^* (so-called excimers) by means of a pulsed electrical discharge. It is important to note that in the case of ArF^*, KrF^* these molecules are not bound in their electronic ground states and therefore dissociate upon relaxation, thereby automatically generating the population inversion necessary for laser action.
As resonator mirrors MgF_2-windows are used. The output coupler is uncoated and has a reflectivity of 8%, and another window working as the back reflector is coated with aluminum. This broadband mirror is used instead of one with a dielectric coating in order to allow a rapid switching of the wavelength by simply changing the operating gas mixture. The duration of the extracted laser pulse is determined by the high voltage circuitry producing the electrical discharge and amount to about 20 ns. In all experiments a relatively low repetition rate of 10 Hz was used.
For 193 nm operation the laser was evacuated and then filled with 110 mbar of 5% Fluor in Helium gas mixture, 250 mbar Argon, and 2650 mbar of Ne. The discharge voltage used during laser operation was 24 kV.

6.7 Laser intensity for Ionization

Measured dependencies of indium monomer and dimer signals on the power density of laser irradiation are presented on the fig.6.18. The signal of In monomer is saturated if power density exceeds $5x10^6$ W/cm^2. Signal of In dimer overcomes through the maximum at energy density about $3x10^6$ W/cm^2. The decrease of signal at higher energies is related to the photo fragmentation of dimer [St02]. The power of laser irradiation was measured by JD500 pyroelectric Joulemeter.

Depending on the particular measurement, two different beam geometry were used.
To measure mass-spectra of sputtered species, the laser beam was operated in the defocused mode. For that purpose, the lens was moved axially to ensure that the focus of the beam was 3.5 cm after extraction point. In this case geometrical size of the beam cross section was 1.3×4.7 mm in directions along and perpendicular to the sample surface. The beam was positioned above the surface at the point where ion beam hit the surface. In this mode the ionization of sputtered species must be saturated (see chapter 7). The laser pulse energy was exceeding 20 mJ. In combination with the pulse duration about 20 ns, the peak power density of laser irradiation was more than 10^7 W/cm^2 . According to results measured by C. Staudt [St02] postionization with this power is saturated and, therefore, measured signal was characterizing the composition of the sputtered flux.

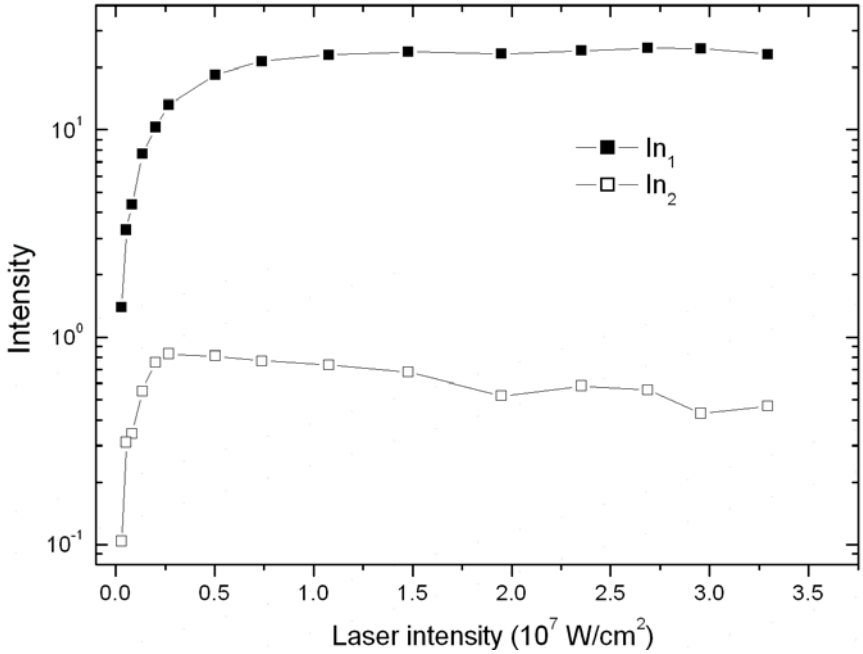

Fig. 6.18 Dependence of sputtered neutral indium monomer and dimer signal on laser intensity.

For measurements of the emission velocity or kinetic energy distributions of sputtered neutral particles, the laser beam was tightly focused in the ionization volume and had dimensions 0.3×0.5 mm. The position of the beam was 2 mm above the surface. The power of laser was reduced by the variable attenuator to that th signal still depended linearly on the laser power density ($\approx$1-2$\times 10^6$ W/cm^2). This was done since in this measurement the saturation of the postionization process must be avoided (see chapter 7).

6.8 Time-of-flight mass-spectrometer

A double–stage reflectron-type spectrometer has been used. The principal schematics of a time-of-flight (ToF) mass-spectrometer is shown in fig. 6.19.
The plume of neutral particles sputtered from the sample surface is intersected by a laser beam. Positively charged ions created in the interaction region are accelerated into the mass-spectrometer by an electric field, which is generated by applying a high positive potential to the sample by means of a fast high voltage switch. This way, the sample can be kept at ground potential during the primary ion pulse, and the extraction field is

switched on after the end of this pulse with a controlled delay. This technique is of particular importance in laser SNMS, since it allows the extraction to be fired after the ionizing laser, thereby eliminating the flight time resolution limit imposed by the temporal duration of the laser pulse.

In SIMS the most significant limitation to the mass resolution in a ToF analyzer is the well-known fact that secondary ions are emitted with some energy distribution. This energy is added to some nominal kinetic energy E_0 which ions of a given polarity receive in the electrostatic extraction section. For atomic ions the resulting energy spread may reach values of a few tens of eV.

The simplest form of the time-of-flight spectrometer has linear construction. In this device ions produced on the sample surface are accelerated by short electrostatic extraction section and enter field–free drift section of length L_0. In a linear ToF analyzer the initial energy distribution of ions of the same mass may cause a broadening of the ion packet as it travels from the sample to detector. The flight time difference between some reference ion (without initial energy) having a flight time t_0 and velocity v_0 after acceleration and another ion with some initial energy and having the flight time t may be described by the parameter τ:

$$\tau = v_0(t - t_0) = L_0(t - t_0)/t_0 \qquad (6.14)$$

If the initial energy ΔE is small enough and the ratio $\delta=\Delta E/E_0<<1$, in first order approximation the flight time error caused by the energy spread is:

$$(\tau/\delta)\delta = L_0(t - t_0)/t_0 = L_0\left[(1+\delta)^{-1/2} - 1\right] \approx -(L_0/2)\delta \qquad (6.15)$$

and

$$m/\Delta m = E_0/\Delta E \qquad (6.16)$$

The basic idea to improve the resolution is to make more energetic ions to fly longer trajectories than less energetic ones. The elegant solution is to use a reflectron which consists of drift regions with electrostatic mirrors. The ion mirror utilizes an electrostatic field to reflect secondary ions in order to provide positive time dispersion. A single stage reflectron is able to improve the resolution by compensating the energy spread to first order.

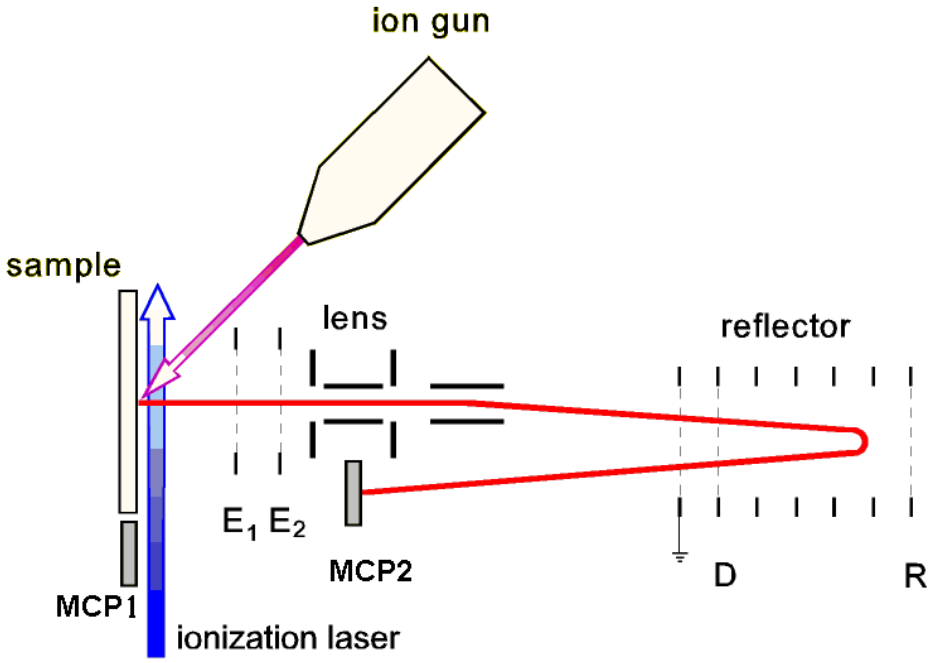

Fig. 6.19 Basic experimental setup for time-of-flight laser postionization SNMS.

In the two stage reflectron for secondary ions second order time focusing may be achieved. The two- stage ion mirror system consists of two drift sections and the mirror itself. The mirror consists of a strong homogenous deceleration field U_D followed by weaker mirror field region U_R.

In contrast to ToF-SIMS, the postionized particles are not created at a constant electrostatic starting potential. Instead, the starting coordinate along the extraction axis exhibits a distribution, the width of which corresponds to that of ionizing laser beam. Therefore the time dispersion conditions of the ToF spectrometer must in laser SNMS mode be optimized with respect to the starting position in the extraction region and the initial kinetic energy of sputtered species. Since it is not possible to achieve flight time focusing with respect to both conditions simultaneously [Wu01], a reasonable compromise must be found. In many cases, the first requirement is much more stringent than the latter one. Practically, the spectrometer will therefore be largely operated under first or second order space focusing conditions.

The postionized neutral particles present in the ionizing volume were extracted towards the first extraction grid (E_1) and thus accelerated to energy of approximately 1600 eV. In principle, the ion extraction optics was designed to allow a two-step extraction scheme involving two subsequent accelerating fields. In the course of the present work, however, this option was not used and both extraction grids (E_2 and E_1) were kept at the same potential.

The deceleration (D) and reflection (R) grids were operated at potentials +570 V and +1900 V respectively in the case of measurements of mass distributions of sputtered species. These values of the potentials were optimized in order to establish optimum time focusing conditions for the extracted photo-ions.

6.9 Detection of sputtered species

The detection of postionized neutral particles was performed by means of a chevron stack of two microchannel plates (MCP2) positioned at a distance of 100μm from each other and operated at the gain voltage of 2000 V.

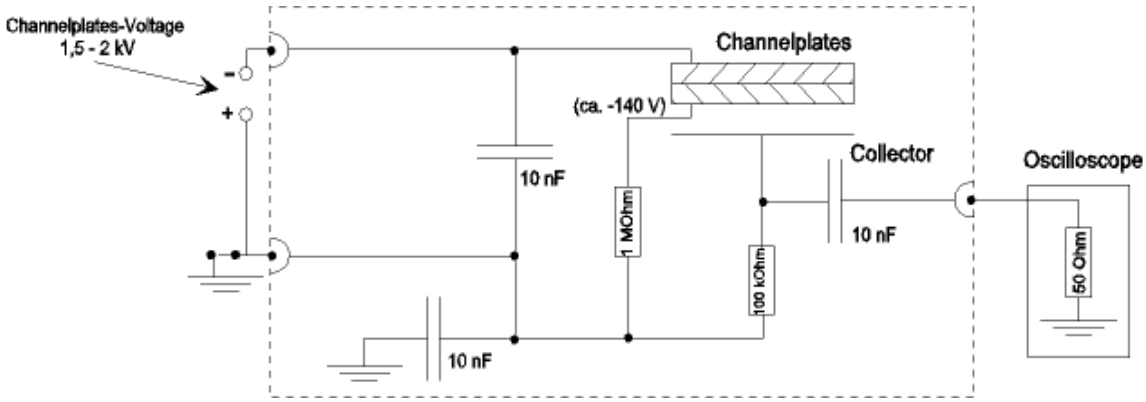

Fig. 6.20 Schematics of Chevron microchannel plate (MCP2) circuit without postaccelaration.

A microchannel plate is a secondary electron multiplier consisting of an array of millions of glass capillaries with an internal diameter from around 10 to 20 microns, fused into the form of a thin disk less than 1mm thick. The wall of each channel is secondary electron emissive, each end of the walls is covered with a metal thin film which acts as an electrode and gain voltage is applied between both ends of the capillary. An electric field is thus created in the direction of the channel axis. After a wall-electron collision, secondary electrons are accelerated by this field and travel along the parabolic trajectories determined by their initial ejection velocity. As a result of repeated secondary electron emissions from the walls, the electron current increases exponentially as the output end of the channel is approached.

At the end of second MCP a collector for the electrons is installed which is made from stainless steel. The distance between that collector and the MCP is 1 mm.

The principal schematics of the MCP stack circuitry is shown in fig. 6.20. In this operation mode there is no additional postacceleration for the detected ions before they reach the MCP front surface. To create a potential of 140 V between the output end of the MCP2 and the collector a 1MΩ resistor is connected with MCP stack. The voltage drop of about 140 V occurs due to the bias current of about 140 μA through the MCP stack. With an electron collector being at the ground potential, and taking into account that postionized ions are created slightly above the surface, the singly charged photo ions strike the MCP surface with a total kinetic energy about 3100 eV. The current produced by the MCP was converted to a voltage by a 50 Ω transition resistor. Time-of-flight spectra were recorded with a LeCroy 9450 transient digitizer and transferred in digital form to a PC for storage and further processing.

In measurements two modes of MCP detector used. First one is analog mode and the second one is digital pulse counting mode.

In the analog mode of detection charge produced by MCP on its collector directly digitized by LeCroy 9450 transient digitizer. This mode is used for detection of monomer and small clusters.

In a pulse counting mode the output of MCP was coupled into a discriminator. In this mode, each output pulse exceeding a discrimination threshold (about 1 mV) was

converted into a standard transistor-transistor logic pulse of 5 V height and 20 ns width. The resulting spectrum was an averaged sum of thousand cycles the same digitizer. Digital mode was used for detection of large clusters.
Cascades of electrons in MCP produced by an individual ions have certain duration about 1 ns. Duration of the time focused pike in the time-of-flight spectrum is about 10 ns. The digital detection mode principally may be used when electron cascades produced by individual ions of the same mass do not overlap in time significantly. Therefore, this detection mode must be operated when there only one ion of certain mass income on the MCP per cycle.

7 Methodology of the measurements

7.1 Time synchronization

The working principle of time-of-flight technique is based on the precise timing sequence of the different pulses. This is most critical part of this technique.
The most important parameters in the SNMS ToF measurement are the duration t_p of the primary ion pulse and the time delay t_d between primary and ionizing laser pulse. In the SNMS technique t_p has no influence on the resolution of the ToF spectrometer in contrast to the SIMS ToF where this quantity may determine the resolution of instrument. Duration times t_p and t_d In SNMS could be varied for different types of measurements (acquisition of mass spectra data, kinetic energy distributions) [Wu01].
The timing sequence of the ToF measurements in the experiment was driven by a digital pulse generator (Stanford Research Systems DG 535). The experiment was triggered by the internal trigger of this unit running at a repetition rate of 10 Hz. The delays of the four others outputs A, B, C, D are programmed relative to the timebase T_0. Two of them, A and B, provide the start and end for the ion pulsing. C and D were used as delay outputs to pulse the potential on the sample (C) and firing laser (D). For generation of a short pulse on the target a home built device forming a TTL pulse with variable duration triggered by the C output pulse was used. The output C was also used for synchronization of LeCroy 9450 oscilloscope used as digitizer. As it was mentioned earlier, LeCroy 9450 oscilloscope is driven from a PC. The connection between Pc and scope is realized through GPIB IEEE 488.2 interface. After it has received the command from computer the oscilloscope perform the acquisition and averaging of time-of-flight spectrum from MCP. During acquisition of data PC waits until the flag of finishing is set by oscilloscope. After that, time-of-flight spectrum (number data of columns: time and intensity) is transferred to PC.
For mass-spectra measurements the ion source was a long pulse of 9 ms and, therefore, quasi-DC primary ion current was sputtering sample. In this mode initially laser was firing and ionizing the plume of sputtered species from the sample. Due to the fact that before laser pulse sample was continuously sputtered (more than 5 μs before) there are particles with all range of kinetic energies present in the ionizing volume. With short

delay (≈30ns) after laser pulse the extraction voltage pulse (1470 V) is applied to the sample. Duration of the extraction pulse is about 4 μs.
Typical values of time delays on the programmed outputs of the time generator in the case of mass spectra measurements are displayed below:

A = B – 5 μs or A = B – 9 ms the intensity of the signal in both cases was the same
B = C – 0.3 μs
C = T_0 + 9.1 ms
D = C – 1.95 μs

For the determination of kinetic energy distributions of sputtered species short primary ion pulses are necessary for sample sputtering. In this kind of experiment only particles with desired emission velocity must be present in the ionizing volume. Due to the fact that the duration of the pulse is not zero and the spatial width of the laser is not ideally small, in reality particles in some velocity range are detected. Actually, a compromise must be made between the duration of the primary ion pulse, the intensity of the signal, and velocity resolution of the measurement. Primary ion pulse duration of 200 ns was therefore used in the measurements.
The initial task before the measurements of kinetic energy distributions was to precisely synchronize the primary ion pulse with the laser pulse or, in other words, to determine the delay settings on the timing generator which ensure that the time delay between the middle of the ion pulse and laser pulse t_d is zero. The choice of center or start of the ion pulse for syncronization with laser may influence the measurement of velocities of "fast" species (having the velocity ≥ 10000 m/s) The ion gun was pulsed using pulse output AB which provides a positive TTL pulse for the interval between the time set for channel A and channel B.

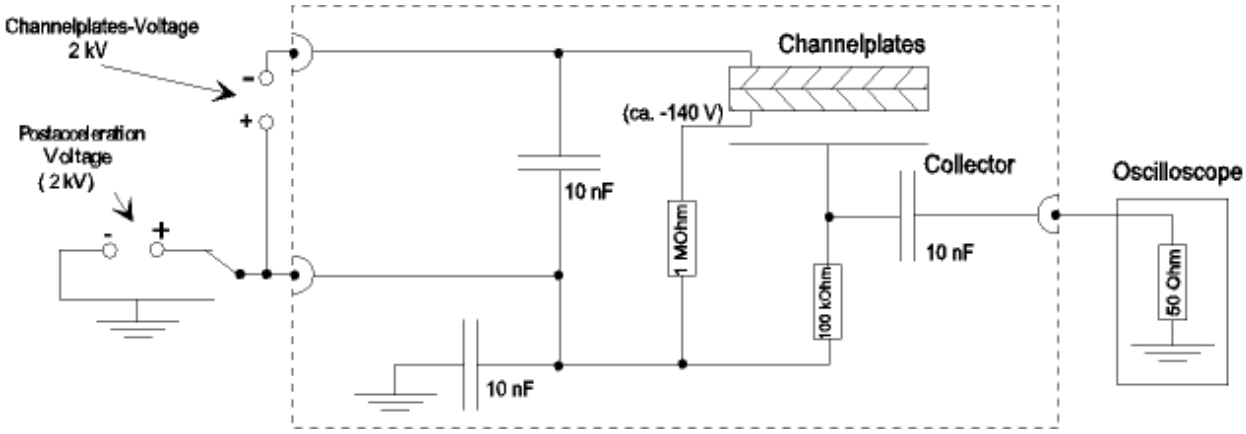

Fig. 7.1 Schematics of Chevron microchannel plate (MCP1) circuit with postaccelaration.

To synchronize ion and laser pulses, another chevron stack of two microchannel plates (MCP1) was used. The type of this detector is similar to MCP2. MCP1 was constructively installed to the sample holder such that the front surface of the first microchannel plate in the chevron stack was positioned at the same level as the sample. The electrical schematics of MCP1 connection are shown in fig. 7.1.
The setup allows applying an additional potential to the MCP front for postacceleration of the detected ions. The gain voltage of floating high voltage power supply producing 2 kV

voltage applied between the front of the first and the rear of the second microchannel plates through 1 MΩ resistor. The whole circuit including HV power supply for the MCPs floated at voltage potential relative to ground provided by a second HV power supply. The two HV power supplies used in this setup produced the same voltage but were connected in opposite polarity. Therefore the potential of the front surface of MCP1 was kept at nearly ground potential. This is a necessary condition for precise synchronization since that the MCP1 surface and the sample have the same (ground) potential and primary ions fly the same trajectories in both cases. During synchronization MCP1 was geometrically positioned in place of the sample using xyz-manipulator. The signal produced by MCP1 was recorded with the same LeCroy 9450 oscilloscope as used for MCP2.

Laser UV irradiation had significant response on the MCP1 in the form of very narrow peak with duration about 20 ns.

The oscilloscope capture of the signal from MCP1 is displayed in fig. 7.2. In particular, the peaks of gold monomer ions at 5 keV kinetic energy and the laser peak are shown.

There is time delay of about 0.95 μs between ion and laser pulse in fig. 7.2. Settings for output B on the time delay generator were: B = C – 3.35 μs. Varying the time delay of the B output on the time delay generator relative to the C and D output it is possible to „move“ the ion peak and synchronize it with the laser peak. Pulse from the time delay generator was applied to a high voltage switch which was pulsing the positive potential on the one of Wien filter plates of the ion source. Pulsing voltage was changed in the range between –200 V and potential used to pass the ions of required mass.

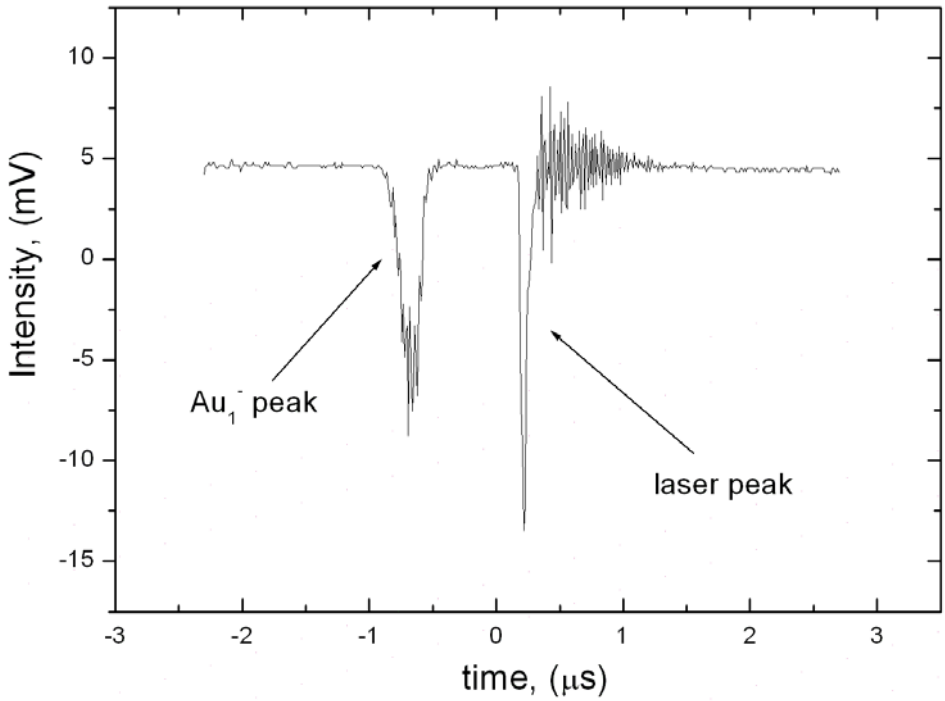

Fig. 7.2 Oscilloscope capture of ion and laser pulses from MCP1.

Settings for A and B pulse outputs on the time delay generator depend on the mass and energy of the ions, because these settings are determined, basically, by their velocity. Below there are shown settings of AB pulse outputs to produce ion pulse with duration of 200 ns and synchronized with laser beam for gold monomer, dimer and trimer with a kinetic energy of 5 keV:

Monomer: A = B – 1.8 μs

B = C – 2.6 μs

Dimer: A = B – 2.35 μs
B = C – 3.6 μs

Trimer: A = B – 2.77 μs
B = C – 4.5 μs

When projectiles have the kinetic energy of 10 keV the setting are following:

Monomer: A = B – 1.25 μs
B = C – 1.9 μs

Dimer: A = B – 1.7 μs
B = C – 2.6 μs

Trimer: A = B – 2.05 μs
B = C – 3.2 μs

From these values it is seen that HV pulse applied to the Wien filter plates is much longer than 200 ns. Moreover this time is increasing with the mass of ion. This is related to the time primary ions fly in the space between Wien filter plates, because delay between A and B outputs t_{AB} must be , basically, the sum of three parameters:

$$t_{AB} = t_p + t_f + t_{\Delta F}$$

where t_p - ion pulse duration (200 ns), t_f - time ions fly in the Wien filter space, $t_{\Delta F}$ - duration of HV pulse front. Characteristic time $t_{\Delta F}$ may be found in technical data sheet for high voltage switch and it is approximately about 100 ns. Taking the length of the Wien filter to be 100 mm, we will find that gold monomer ion with 5 keV energy require $t_f = 1.43$ μs to this distance. Therefore we get the time delay $t_{AB} = 0.2 + 1.43 + 0.1 = 1.73$ μs. This in the agreement with experimental values within 5% error. Similar evaluations may be made for other masses and energies.

Time delay between B and C outputs also becomes larger with the mass due to the fact that ions with larger mass have lower velocity and ion pulse ate the exit of the Wien Filter must be formed earlier. Distance between sample and Wien filter is approximately 18-20 cm. For gold monoatomic projectile with 5 keV kinetic energy time delay for B output is 2.6 μs. It may be easily evaluated that the particle with such mass and energy passes during this time passes the distance of about 18 cm. Using time delay for gold diatomic projectile with 10 keV kinetic energy one may evaluate the same distance.

Time delay between laser and extraction pulses could be estimated from fig. 7.2. the high frequency glitching produced by HV switch follows after narrow laser pulse with delay about 100 ns. This time delay always remains unchanged.

7.2 Method

In this chapter basic principles of measurements in the laser SNMS technique are described employed in the present work are described. Initially the experimental parameters which influence on the measured signal must be described in this chapter.
In the laser SNMS a pulsed ionization volume is employed. Space parameters of ionization volume are determined by laser beam dimensions along and perpendicular to the sample surface. Those species in the flux of sputtered neutrals, which intersects an ionization volume (laser beam) in time and space position, are postionized. Due to the fact that the laser pulse has certain duration, the number of neutral particles which are postionized may be divided into two contributions. First contribution is the number of particles which are present within ionization volume at the time laser fire. This contribution is proportional to the number density of sputtered particles within the ionization volume, and can be termed "density contribution" [Wu01]. Second contribution includes those particles that are localized outside ionization volume at the time laser is fired, but which enter this volume during laser pulse. This number is proportional to the flux of sputtered particles across the ionization volume and can be termed "flux contribution".
How the postionization process depends on the laser power is described in chapter 8 in more detail.
ToF spectrometer, in general, performs time focusing of certain mass within some energy range (window) around nominal the one. On the other hand, the entrance energy of postionized sputtered neutral particles depends on the distance above the surface where the ionization took place. Therefore, the particles within some interval perpendicular to the sample surface are detected. Lateral acceptance of the ToF spectrometer is also restricted. The lateral dimensions of the extraction volume (in direction parallel to the surface) are mainly restricted by the geometrical size of the aperture in the extraction electrode accelerating the photoions into the ToF spectrometer. In principle, the dimensions of extraction volume can be measured by translating the tightly focused laser beam in directions along and perpendicular to the surface normal and registering the detected photoion signal as a function of focus position. On the instrument employed here, experiments of this kind have been performed by Dr. M. Wahl [Wa95], revealing an extension of 1 mm in all three dimensions. This knowledge is of particular importance in experiments where the saturation behavior of the photoionization process is studied.
Due to the fact that laser beam in its cross section have spatial distribution of the intensity, in the case when the beam laser beam cross section is smaller that dimension of extraction volume than the effective ionization volume may depend on the laser intensity. Effective ionization volume in this case will expand with increase of laser intensity due to increasing signal contribution from the "tails" in the beam spatial intensity distribution.
In the experiment, during acquisition of mass spectra of sputtered neutrals the laser beam was defocused such that the extraction volume of the mass spectrometer is entirely contained within effective ionization volume. Moreover, laser postionization was operated in saturated mode (all neutral particles present within extraction volume during laser is fired are postionized). Due to the fact that the cross section dimensions of laser beam ≥ 1 mm transport of particles into and out of the ionization volume during laser pulse can be neglected. Therefore, in this case measured signal corresponds to the number density of sputtered neutral particles.
For detection of secondary ions, the ionization laser is simply switched off, while all other parameters (ion bombardment, acceleration voltage, ToF spectrometer settings, etc)

remain unchanged. In particular, the extraction field must be switched on after termination of primary ion pulse. Therefore, the space above the sample is field-free and secondary ions propagate in the same way as their neutral counterparts. Under these conditions the extraction region from which ions are accepted and detected by the spectrometer are the same for secondary ions and postionized neutrals. Generation of the ToF spectrum remains valid, and the instrument therefore detects sharp flight time peaks of those secondary ions which are present within extraction volume at the switching time of the extraction field. It should be noted that the width of the time peaks of secondary ions measured in this way is independent of the primary ion pulse length and one can therefore utilize long pulses of primary ions ensuring that ionization volume is completely filled with sputtered particles (ions and neutrals) of all emission velocities. Under these conditions, the measured ion signals are representative of the number density of secondary ions within the ionization volume (instead of the flux as in usual ToF-SIMS spectra) and, as such, are directly comparable to the respective post-ionized neutral signals. Moreover, since the instrument cannot distinguish between post-ionized neutrals and secondary ions present within extraction volume the transmission and detection efficiency for both species are identical.

In experiments devoted to the determination of the kinetic energy distributions of the sputtered atoms and clusters, focused laser beam positioned at distance of 2 mm above the sample. The kinetic energy of the sputtered neutral particles can be selected by the time delay between the primary ion pulse and the firing time of the ionization laser. The conversion of the flight time distributions into energy spectra requires a detailed analysis of the recorded spectra. A theoretical description of this conversion is given in [Wu93c].

Due to the small dimensions of the ionization volume the flux density in this case may not be neglected. Then two contributions must be considered. It is shown that for sufficiently short primary ion and laser pulses τ and Δt and a small ionizing volume extension distributions Δr the signal S of a postionized sputtered neutral particle measured at a time t and distance r from the surface is given by

$$S \propto f(v)\frac{v}{r}\left[\Delta r + v\Delta t\right].$$

Here $v = r/t$ denotes the velocity selected by the particular choice of t, and $f(v)$ represents the flux velocity distribution of sputtered particles. Hence, the signals are converted to flux energy distributions by

$$f(E) \propto \frac{S(t)}{mv^2\tau\left[\Delta r + v\Delta t\right]} \propto \frac{S(t)\cdot t^2}{\left[\Delta r + v\Delta t\right]}$$

It is important to note that the second term in the denominator of last equation only occurs if the photoionization process is driven into deep saturation for the species under investigation [Wu93c]. Interpretation of data in this case is significantly complicated, because it is necessary to know exact duration of laser pulse etc. Therefore, during measurements of the kinetic energy distributions it is desirable to use the postionization in unsaturated mode.

7.3 Measurements procedure

In the following the measurements procedure is described:

- When laser pulse ionized plume of the sputtered particles from In-sample there was applied high voltage pulse from switch to the sample in order to extract postionized ions for analysis in the spectrometer. In addition to the postionized ions there were secondary ions in the extraction volume. Secondary ion mass spectra were measured in order to prove that secondary ions did not contribute significantly in the mass distributions of postionized neutrals.
- Every mass-spectrum in the digital mode was measured 1000 times.
- For determination of secondary ion formation probabilities laser postionization was operated in saturated mode and laser beam was defocused such that the effective ionization volume is entirely determined by the sensitive volume of the mass spectrometer.
- Mass-spectra of residual gas were measured. These spectra contain atomic and molecular postionized ions of residual gas being present in the sensitive volume of the spectrometer at the time the ionization laser fires.
- In the measurement of kinetic energy distributions the intensity of laser was attenuated to provide unsaturated postionization of indium monomer.
- During the measurement of kinetic energy distributions laser postionization have been operated in the focused mode. In this case the distance between the ionization volume and sample surface was determined by translating the sample from the analysis position towards the laser beam until the laser hit the sample surface.

8 Photoionization

When atoms and clusters sputtered from a solid state surface interact with UV laser irradiation they may ionize or, incase of cluster, fragment. To describe the interaction of VUV photons with sputtered clusters in a simple theoretical model the following different processes must be considered:

- Ionization of a neutral cluster
- Fragmentation of a neutral cluster after absorption of photons.
- Fragmentation of ionized clusters by the absorption of additional photons

For process induced by absorption of one single photon, the corresponding rates are given by

$$R_{I,F_0,F_i} = \frac{P_L}{h\nu}\sigma_{I,F_0,F_i} \qquad (8.1)$$

where σ_I, σ_{F_0} and σ_{F_i} denote the cross sections for ionization, neutral and ionic fragmentation, respectively, P_L is the laser power density, $h\nu$ is the photon energy. For simplicity we assume that the temporal laser pulse profile has rectangular form and, hence, P_L is constant throughout the laser pulse duration Δt. Then, the rate equations describing the number density of neutrals and ions n_0 and n_i within the volume of interaction between laser and sputtered particles read

$$\dot{n}_0 = -R_I n_0(t) - R_{F_0} n_0(t) \qquad (8.2)$$

$$\dot{n}_i = +R_I n_0(t) - R_{F_i} n_i(t). \qquad (8.3)$$

With the boundary conditions $n_0(t=0) = n_0$ and $n_i(t=0) = 0$, the set of equations 8.2 can be easily solved yielding

$$n_0(t) = n_0 \exp\left(-\frac{(\sigma_I + \sigma_{F_0})t}{h\nu} P_L\right), \qquad (8.3)$$

and

$$n_i(t) = p_0 \frac{\sigma_I}{\sigma_I + \sigma_{F_0} + \sigma_{F_i}} \times \left[1 - \exp\left(-\frac{(\sigma_I + \sigma_{F_0} + \sigma_{F_i})t}{h\nu}\right)\right] \times \exp\left(-\frac{\sigma_{F_i} t}{h\nu} P_L\right) \qquad (8.4)$$

The number of nonfragmented photoions crated within the interaction volume ΔV during the laser pulse of duration Δt, and hence the signal measured at a specific laser power density P_L, is proportional to

$$S(P_L) \propto n_i(t) \Delta V \qquad (8.5)$$

From given dependencies of the photoion signal (8.3 and 8.4) detected for a particular cluster a limiting case can be considered. If no fragmentation occurs, i.e. $\sigma_{F_{0,i}} << \sigma_I$, the usual saturation behavior of a single photon ionization process according to

$$S(P_L) \propto p_0 \left[1 - \exp\left(-\sigma_i \frac{\Delta t}{h\nu} P_L\right)\right] \qquad (8.6)$$

is observed.
Experimental measurements of signal dependencies in a wide range of laser power density were performed by Staudt [St02].
From power dependencies of the signals of indium monomer and dimer in fig. 6.18 it is seen that, at low laser Power density P_L the signal rises with increasing P_L as is expected for a single photon absorption process. For monomer, when signal approaches about $5 \cdot 10^6$ W/cm^2, the signal levels off due to the saturation of ionization process. For sputtered dimer, the saturation is achieved at lower power density of about $2.5 \cdot 10^6$ W/cm^2. A further increase of P_L leads to an increasing amount of photon induced fragmentation and the signal therefore decrease. Power dependence of the signal, in this case must be described by last exponential term in Eq. (8.4).

RESULTS

In this chapter experimental results are presented. There are three main parts. The first one deals with the mass distribution of neutral particles sputtered from a polycrystalline indium surface by mono and polyatomic gold ions with different kinetic energies. As parameters, the number of atoms in the impinging Au_m^- ion, i.e. the projectile "nuclearity" $m = 1 \div 5$, and the total kinetic energy of the projectile (5-10 keV) is varied. The goal of these experiments is to determine the influence of the projectile nuclearity m on absolute total and partial sputtering yields and, in particular, to investigate the question whether the relative contribution of clusters in the sputtered flux is enhanced under polyatomic ion bombardment. Changes in the total sputtering yield of atoms and clusters per projectile atom under mono and diatomic ion bombardment at the same velocity are shown.
In the second part, kinetic energy distributions (KED) of indium monomers sputtered by gold mono-, di-, and triatomic projectile ions with kinetic energies of 5 and 10 keV are presented and discussed. Experimental KED data is qualitatively compared with theories of the sputtering process under "spike" – conditions.
The third part describes the experiments determining the ionization probability of sputtered Indium monomer and its variation as a function of the projectile nuclearity. These data contain valuable information on the electronic excitation processes induced by the projectile impact and their variation for different projectiles.

9 Time-of-flight mass spectra

9.1 Sputtered Postionized Indium clusters

The signal from MCP2, is detected as a function of time after the projectile ion pulse by a digital oscilloscope. The resulting trace is stored in the computer where it is converted from a time-of-flight spectrum to a mass spectrum using the dependence $t \propto \sqrt{m}$. An important question in this conversion concerns the time zero marking the start of the flight time measurements of the detected ions. In our experiment, time zero corresponds to the starting of extraction HV pulse on the sample. In practice, in the software "MASSMAIN", which manage the acquisition of data from oscilloscope, it is possible to perform a mass calibration according to $m = a \cdot (t - t_0)^2$ function with fitting parameters a and t_0 for each acquired ToF spectrum.

Fig. 9.1 shows the resulting mass-spectra of neutral indium atoms and clusters sputtered under polyatomic ion bombardment with 10 keV kinetic energy, which were postionized by UV laser irradiation with wavelength 193 nm and power density of $5 \cdot 10^7$ W/cm^2.

It is seen that the signal of In monomers is most intensive in comparison with the cluster peaks and, moreover, the intensity of the signal corresponding to sputtered In_n clusters is strongly decreasing with increasing number n of constituent atoms. In every panel (a,b,c) of fig. 9.1 two spectra of the clusters measured in different regimes are displayed. The relatively large signals of monomers and dimers of indium were measured directly from MCP in the analog detection mode. The signals of larger clusters were detected in the digital mode of single ions counting (chapter 6.9). Two kinds of mass spectra were connected together at the indium trimer signal because the intensity of this peak was still large enough to be measured directly in the analog mode and, on the other hand, was small enough to be detected in the digital mode without saturating the ion count scheme. Every digital spectrum is statistically averaged over 1000 single "shots", i.e. projectile ions and laser pulses and the resulting measured ToF spectra. Spectra measured in the analog mode had been averaged over 100 of single ToF spectra. From the spectra it is seen that the resolution of the spectrometer for atomic indium particles is m/Δm ≈ 200. The appeared different noise levels in the spectra measured in the two modes are related to different detection sensitivities.

The spectra shown in fig. 9.1 were not normalized to the per primary ion current. Note that, although the primary ion current for di- and triatomic gold polyatomic projectiles is about one order of magnitude smaller than that of monoatomic projectiles (fig. 6.8), the absolute signal of sputtered indium large clusters sputtered under polyatomic ion bombardment is higher. In all spectra, in addition to the peaks of pure indium clusters there are heteronuclear clusters $In_n Au$ of indium and gold. It is interesting to note that for heteroclusters in contrast to indium clusters odd-even alternations are observed.

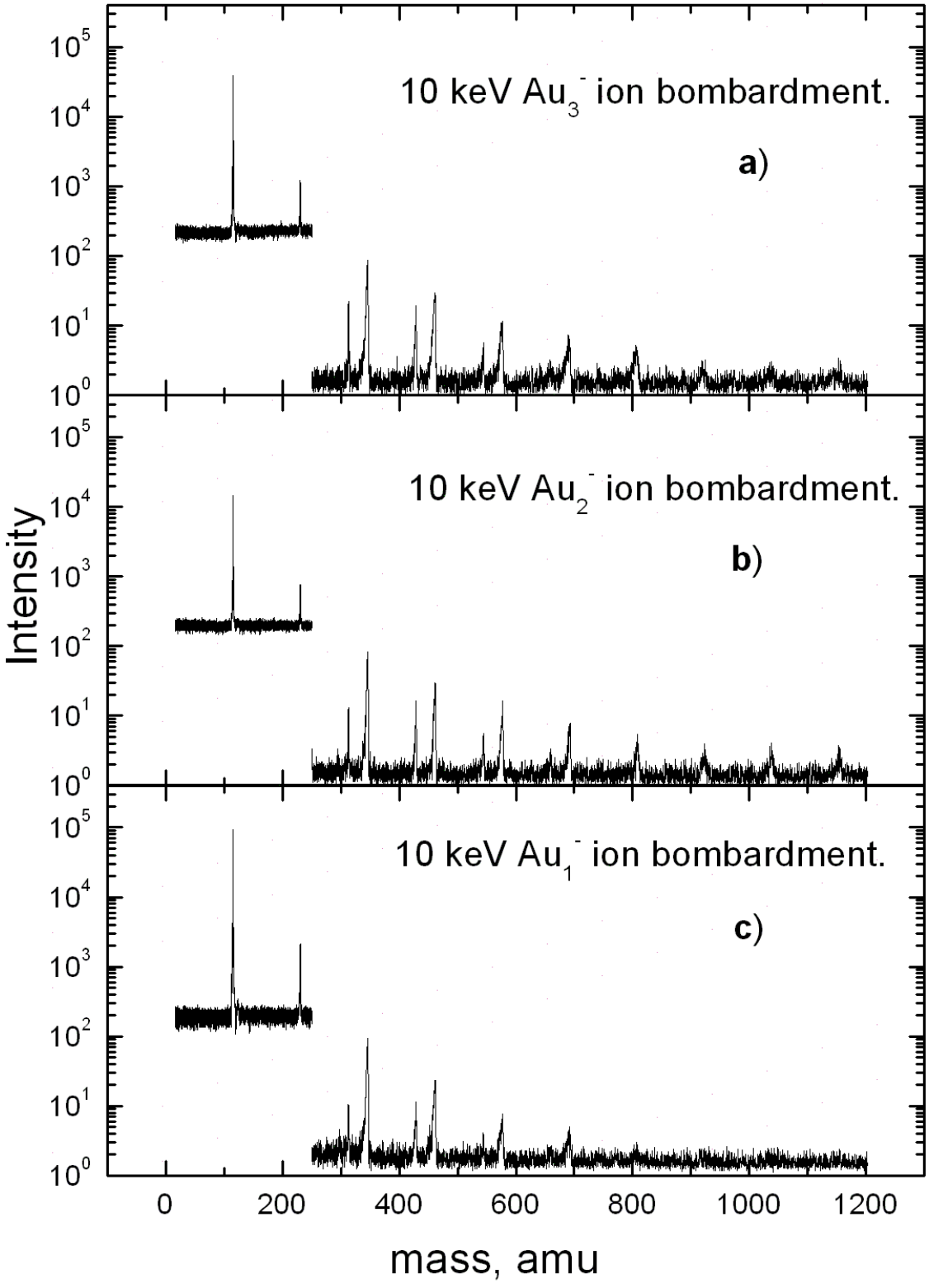

Fig. 9.1. Time-of-flight spectra of sputtered In-clusters under polyatomic ion bombardment with 10 keV kinetic energy per projectile. Postionization: 193 nm, $5 \cdot 10^7$ W/cm^2.

The real partial sputtering yields of sputtered indium clusters could in principle be underestimated by the relative signal displayed in fig. 9.1 due to the following factors:

- The photofragmentation of the clusters during postionization. Therefore, relative yields obtained from saturated signals represents lower limits to the actual cluster yields.
- Detection of large indium clusters is less effective due to the velocity dependence of the secondary electron yield. All indium cluster detected on the MCP were having equal kinetic energy therefore clusters with higher mass had been slower. Detection efficiency for large clusters in that case is lower. Detailed investigation of the detection efficiency by chevron MCP detector of large indium clusters in dependence on the cluster size is performed by Staudt.[St02]. These measurements show that relative detection efficiency of indium cluster ions In_n with $n \leq 10$ at the impact kinetic energy 3.7 keV changes insignificantly and nearly constant. Moreover, this parameter is important for qualitative determination of mass distribution of sputtered species. Since in this study, comparative investigation of sputtering process under atomic and polyatomic ion bombardment is aimed. The correction of measured signal to the detection efficiency has not been made.

9.2 Residual gas spectrum

The mass spectra displayed in fig. 9.1 consist of the signals of sputtered neutrals and, in addition, of secondary ions and residual gas particles postionized by the laser. A discrimination between these signals in the mass spectrum itself is not possible, therefore in order to estimate the contributions of secondary ions and residual gas signals to the measured spectra it is necessary to measure them separately.
Residual gas spectra were measured without ion bombardment of the sample under otherwise the same experimental conditions (position, timing and intensity of the laser beam, voltages etc). The spectrum of the residual gas at a total pressure of about $\approx 10^{-7}$ mbar in sample chamber and a laser intensity of $5 \cdot 10^7$ W/cm^2 is shown in fig. 9.2. The spectrum was measured in the digital detection mode. The fact that there is no indium signal in the spectra induces that ablation of the sample by ionization laser is negligible. Mostly the spectrum consists of light masses of carbon and its chemical compounds. In the spectra displayed in fig. 9.1, the residual gas peaks have been subtracted.

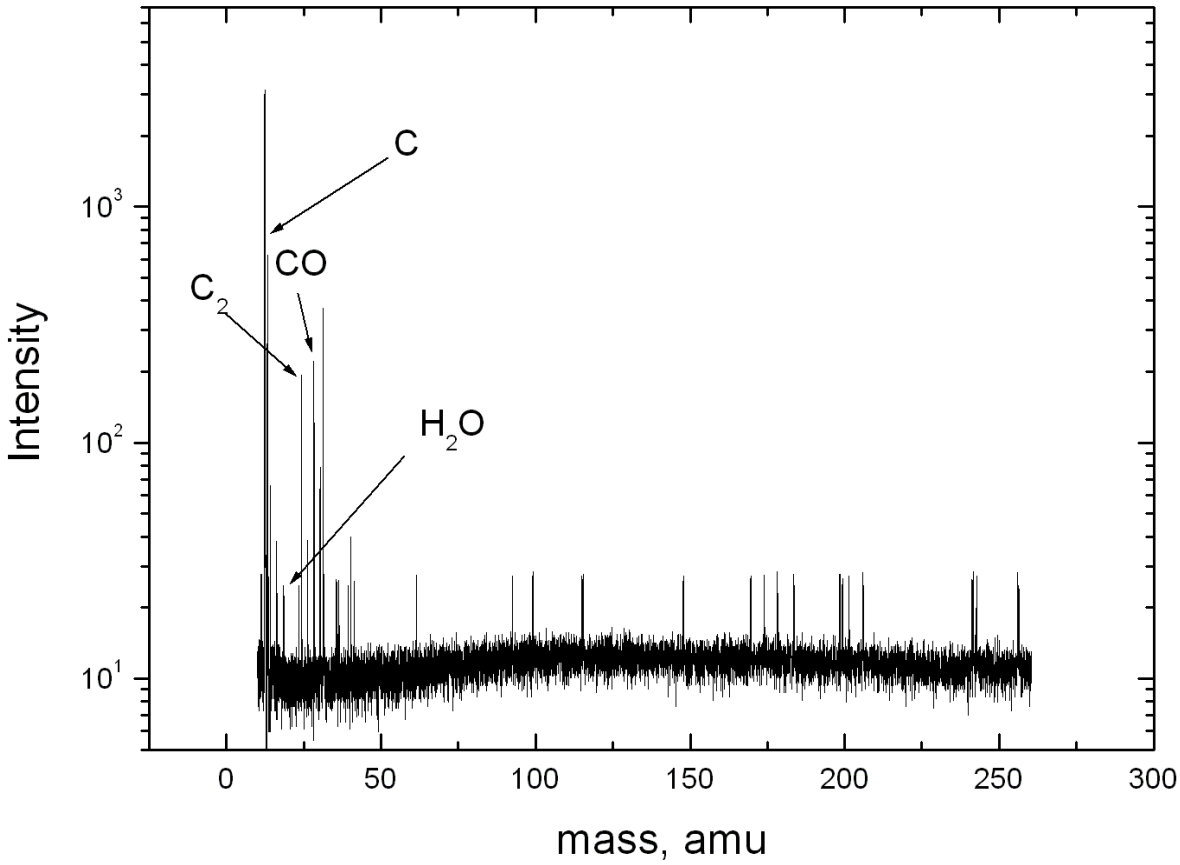

Fig. 9.2. Spectra of postionized species of the residual gas in the vacuum chamber.

9.3 SIMS spectra

Mass spectra of secondary ions sputtered under identical experimental conditions as for sputtered neutrals are shown in fig. 9.3. The acquisition of SIMS spectra was performed in the digital detection mode and each spectrum was averaged over 1000 individual measurements (shots).

From the spectra in fig. 9.3 it is seen that the dynamic range of the secondary ion signal only warrants the observation of monomers and dimers under Au_3^- and Au_1^- ion bombardment. Under Au_2^- bombardment only the sputtered indium monomers were detected.

A particular feature of the spectra is the significant decrease of the signal intensity for the dimer in comparison with signal of monomer. This finding is in good agreement with data measured under different experimental conditions when larger values of the primary ion current density and better vacuum was used [St02]. It is interesting to note that the ionization probability of sputtered indium dimers measured in this work is much lower in comparison with the indium monomer.

In the range of low masses, the secondary ion spectra contain prominent peaks of sodium and potassium. These ions represent trace contaminants contained in most metals and are usually always observed due to their high ionization probability for positive charging.

On the basis of the signal levels in the spectra of fig. 9.3, the conclusion is evident that ToF spectra in fig. 9.1 practically exclusively consist of postionized neutral clusters of

indium. In particular, the intensity of secondary monomer ions may be neglected in comparison to the signal of postionized sputtered indium monomers.
The mass resolution visible in the SIMS spectra is similar to that observed in SNMS ($m/\Delta m \approx 200$).
Due to the limited dynamic range induced by the small magnitude of the SIMS signal (or ionization probability) in contrast to the SNMS spectra (fig. 9.1), no large secondary cluster ions are observed under polyatomic ion bombardment. The intensity of the SIMS signal under Au_3^- ion bombardment is higher in comparison with Au_2^- sputtering at the same kinetic energy and nearly equal primary ion currents.
No indication of multiply charged atomic or cluster secondary ions was found in the spectra.

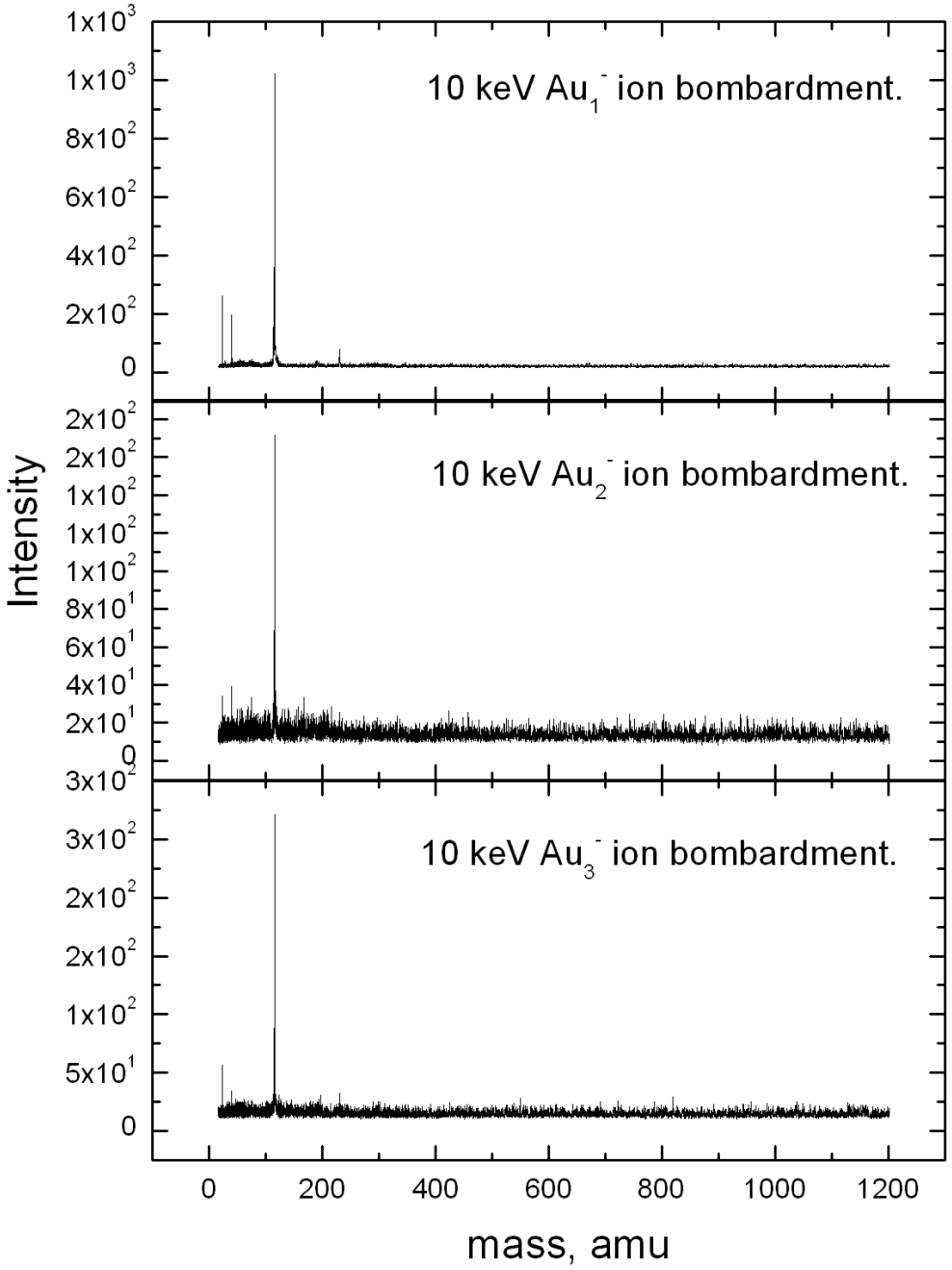

Fig. 9.3. Time-of-flight spectra of sputtered secondary indium ions under polyatomic ion bombardment with 10 keV kinetic energy per projectile.

10 Non- additivity of the sputtering

10.1 Integrated mass –spectra

The ToF mass spectra shown in fig. 10.1 can be peak integrated in order to calculate the precise contribution of clusters with a certain number of atoms in the total sputtered flux. Integrated mass-spectra of indium clusters sputtered by $Au_1^-, Au_2^-, AuCs^-, Au_3^-, Au_5^-$ projectile ions, normalized to the respective ion current and to the signal of indium monomer sputtered by Au_{11}^- projectile with 5 keV, are shown in fig. 10.1.

First feature which can be noted in the spectra on the fig. 10.1 is that partial sputtering yields of indium clusters for all bombardment conditions are higher for 10 keV kinetic energy than for 5 keV. This finding is due to the higher total sputtering rate. Considering the intensity for different projectiles in both cases of 5 and 10 keV it is seen that total intensity of the signal is gradually increasing with the mass/nuclearity of primary cluster reaching some kind of saturation. The most drastic yield increase is always observed when changing from monoatomic to diatomic projectiles.

In fig. 10.1, all data were plotted in double logarithmic scale to illustrate a power law dependence of the relative yield distributions of neutral indium clusters for all cases of bombarding conditions. The best fit line corresponding to

$$Y(n) \propto n^{-\delta}$$

results in exponent δ depending on the energy and mass or nuclearity of the projectile which are displayed in table 10.1. For both kinetic impact energies of the primary ions, the exponent δ is largest for to monoatomic bombardment, and gradually decreases with increasing nuclearity of the projectile. Similar to the sputtering yields, also the exponent δ is found to increase most significantly going upon switching from monoatomic to diatomic ion bombardment.

	10 keV	5 keV
Au_1^-	-5.62 ± 0.19	-5.69 ± 0.15
Au_2^-	-4.46 ± 0.2	-5.28 ± 0.15
$AuCs_2^-$	-4.16 ± 0.15	-4.96 ± 0.11
Au_3^-	-4.32 ± 0.24	-4.67 ± 0.14
Au_5^-	-4.35 ± 0.16	-4.41 ± 0.07

Table 10.1. Exponent values δ for power law fitting of mass distributions for different energies and projectiles.

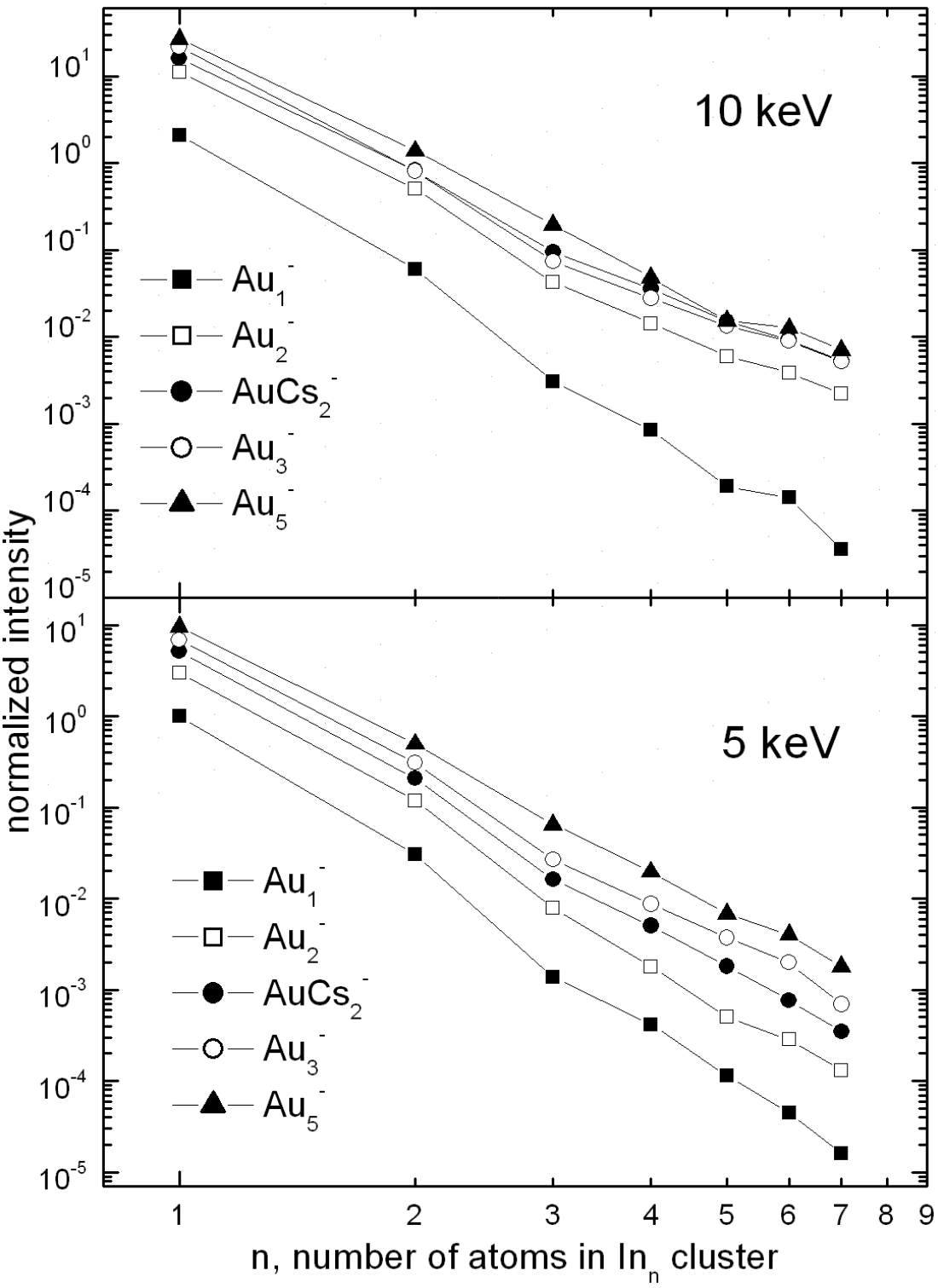

Fig. 10.1 Integrated mass-spectra of postionized indium clusters sputtered by polyatomic ions at energies 5 and 10 keV.

If we want to determine the respective total sputtering yields, it is important to note that the laser postionization experiment is sensitive to the number density (see section 7) of sputtered neutral particles that are present in the ionization volume. Sputter yields, on the other hand, represents the flux of sputtered particles rather their number density. In order to determine the yields, which is properly determined by the yield of monomers, the experimental data must be therefore converted from density to flux. For that purpose the velocity distributions of sputtered atoms must be known and measured signal must be divided by an average inverse velocity. The average inverse velocities of sputtered indium monomers corresponding to mono-, di-, and triatomic projectiles at the 5 and 10 keV impact energy are determined in chapter 11.1. In chapter 11.1 it is shown that in the case of Au^- projectile with impact energy of 5 keV the indium monomers are sputtered mostly from linear collision cascades. Therefore corresponding sputtering yield may be estimated from computer simulations by SRIM 2003 which performs the simulation of the sputtering in the mode of binary (linear) collisions. The computer simulation predicts that the sputtering yield in this case is about 11.9. Using data on inverse velocities from chapter from chapter 11.1 and measured monomer signal normalized to the respective ion current we can obtain the sputtering yields produced by different projectiles. Since we do not have values of the inverse velocities of sputtered indium atoms emitted under Au_5^- bombardment, the inverse velocity for triatomic Au_3^- projectile was used. On the following figure the respective sputtering yields are presented.

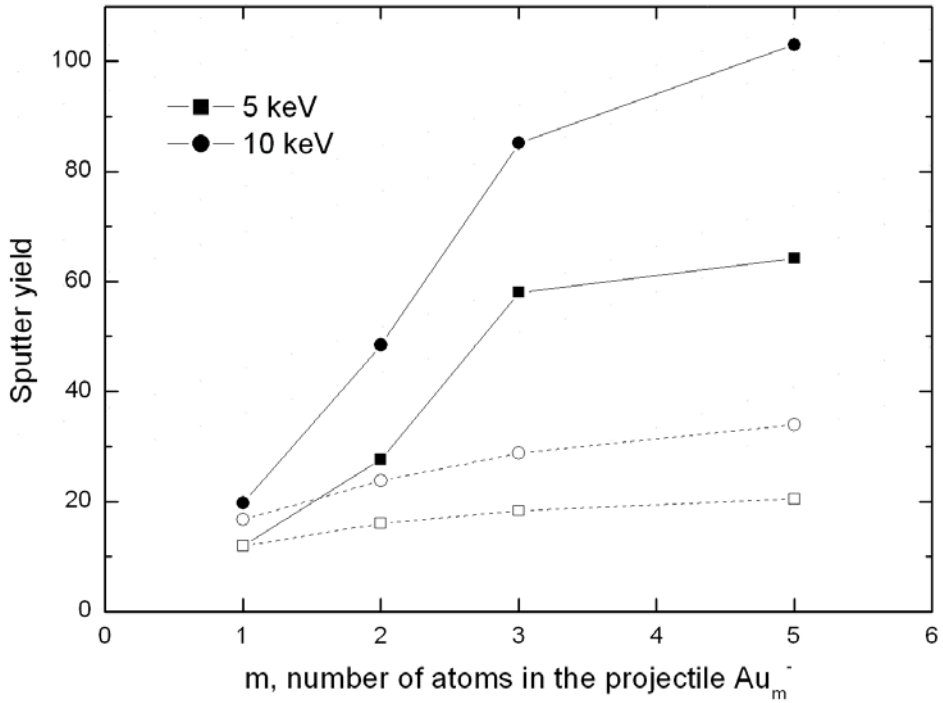

Fig.10.2 Relative yields of In atoms in dependence on the nuclearity of the particle for different energies of projectiles.

In fig. 10.2 the data on the sputter yields for corresponding projectiles obtained from SRIM 2003 calculations is shown with hollow symbols and dotted lines. From fig. 10.2 we can see that the SRIM calculation predicts significantly lower yields for polyatomic projectiles. The data obtained from SRIM show similar behavior of the yield in dependence on the nuclearity of the projectile. Both experimental data and data obtained by SRIM show that the sputter yield is linearly increase with increasing projectile

nuclearity up to triatomic projectile and then saturation of the yield occurs. But the slope is much smaller for the SRIM calculation, characterising strong non-linear contribution to the yield for polyatomic projectiles.
It would be very interesting to compare these results with MD simulations performed for gold ion impact onto indium. At the moment there is no such data available for indium due to the lack of a good many-body interaction potential for this target material. There are, however, recent MD investigations of the sputtering of an Au (111) surface induced by 16 keV Au_m polyatomic bombardment (m = 1, 2, 4, 8, 12) performed by Urbassek et al. [Ur00]. The results, which are listed in table 9.2 show a qualitatively similar behavior of the total sputter yields on the nuclearity of the projectile at constant total kinetic impact energy as observed here. The sputter yield linearly increase with increasing projectile nuclearity up to m=4 where it level-off and even decrease.
It should be noted that the yield of indium atoms sputtered by Au_5^- projectiles, shown in fig 10.2, may be overestimated since we do not have the values of the average inverse velocity for such projectile and data for triatomic projectile Au_3^- was used.

n	Y
1	65
2	164
4	350
8	304
12	296

Table 10.2 sputtering of Au (111) surface induced by 16-keV Au_n cluster impact: average sputter yield Y [Ur00].

10.2 Enhancement factor

Experimentally non-linearity of the sputtering process manifest itself in the non-additive enhancement of the partial sputter yield. In order to determine the non-additivity of partial yields under polyatomic ion bombardment the yield distributions of sputtered neutrals must be compared at constant impact velocity of the projectiles. In fig 10.3 mass-spectra of indium clusters sputtered by gold mono and diatomic ion bombardment with 5 keV per atom are shown. The signal of indium monomer under Au_2^- ion bombardment was corrected to the average inverse velocity. The higher sputter efficiency and larger relative cluster contribution induced by diatomic projectiles is clearly visible. The spectra are plotted in double logarithmic scale and are fitted by power law functions. The value of the exponent σ is lower under polyatomic projectile irradiation.
Quantitatively, a non-additive enhancement factor is calculated as ratio of the yields of In_n clusters per atom sputtered by different projectiles impinging with the same velocity.

$$K_{m,m'} = \frac{Y_m(n) \cdot m'}{Y_{m'}(n) \cdot m}$$

where m and m‘ devote to the different nuclearities of the projectiles. To calculate $K_{2,1}$ from the yields distributions shown in fig. 10.3, the data produced under 10 keV Au_2^- bombardment must be divided by two times the data obtained under Au_1^- bombardment

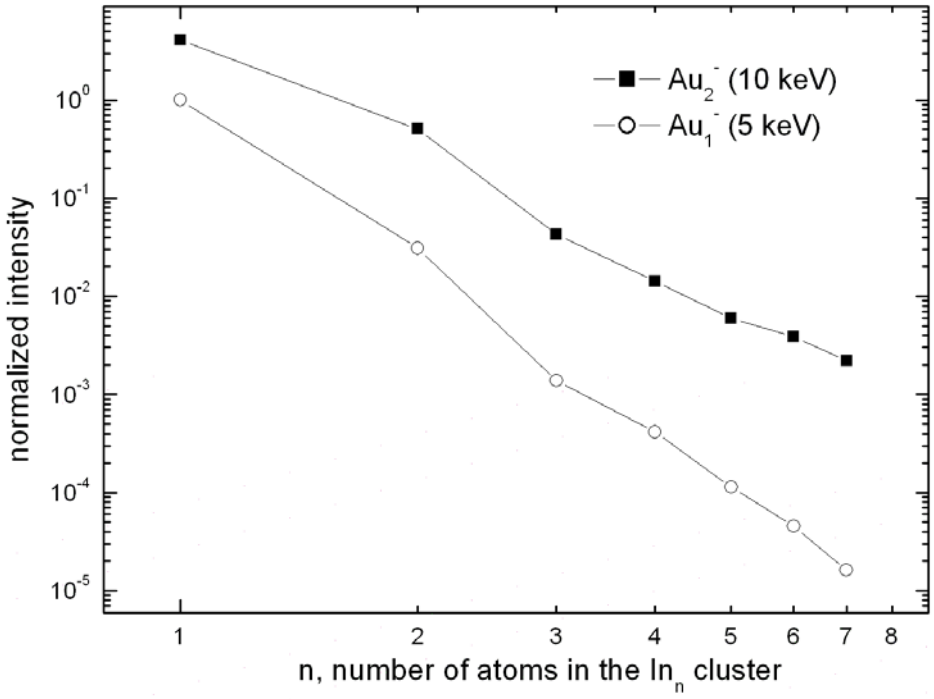

Fig. 10.3 Spectra of indium clusters sputtered by gold atomic diatomic ions with 5 keV per atom kinetic energy.

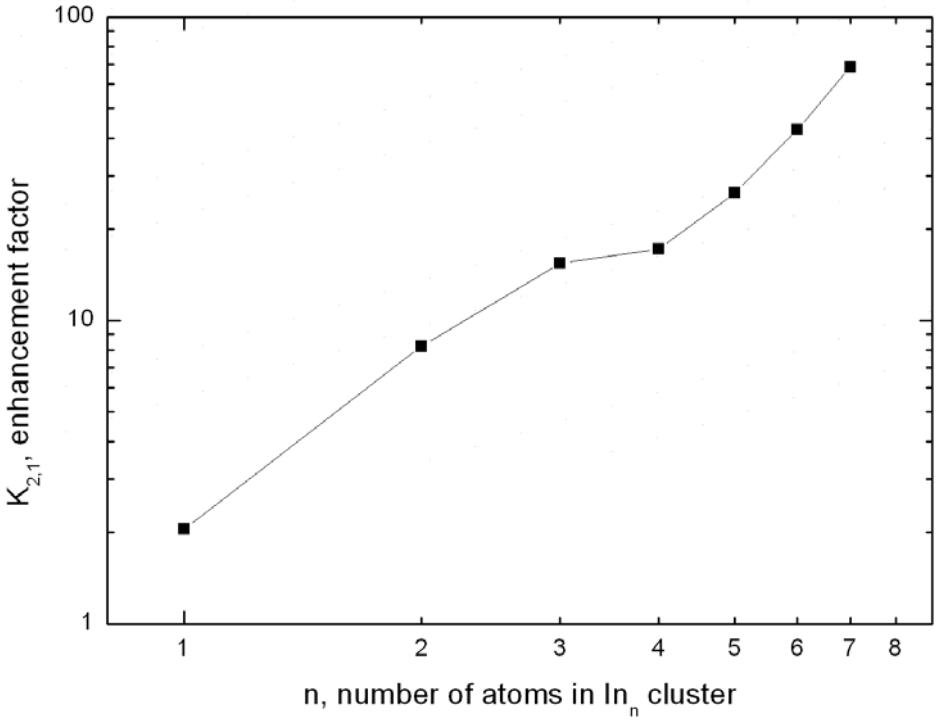

Fig. 10.4 Enhancement factor of the yield of indium clusters $K_{2,1}$ sputtered by gold atomic and dimer ions with 5 keV per atom.

with energy of 5 keV. The enhancement factor $K_{2,1}$ calculated that way shown as a function of the nuclearity *n* of sputtered cluster In_n in fig. 10.4.
The enhancement of the total sputtering yield, which is predominantly determined by the yields of indium atoms is at a factor of 2.1. This means that the non-linear contribution to the total sputter yield already exceeds the contribution from linear cascade sputtering. More specifically, if we assume the particle emission under bombardment with 5 keV Au^- projectiles to be entirely due to linear cascade sputtering, the contribution of spikes amounts to 54% of the total sputter flux under bombardment with 10 keV Au_2^-.
Enhancement factor is rather gradually increasing with cluster size reaching values of about 70 for the large ones.

11 Kinetic energy distributions of In atoms

11.1 Experimental data

Latest results on the kinetic energy distributions of sputtered indium neutral monomers under atomic and polyatomic ion bombardment have been taken using second version of the source.
The resulting kinetic energy distributions (KED) of sputtered indium atoms induced by atomic and polyatomic ion bombardment are shown in fig. 11.1. The kinetic energy distributions of neutral indium atoms sputtered by the same projectiles (Au_1^-, Au_2^- and Au_3^-) with a kinetic energy of 10 keV are shown in fig 10.2. The method of the measurements is described in chapter 7. The experimental dependencies show two contributions in the sputtering yield of atoms from collision cascades and spikes. Atoms sputtered from a spike are significantly less energetic in comparison with atoms sputtered from a cascade.
It is clearly seen that the low energy contribution from the spike increases with increasing kinetic energy and projectile nuclearity.
In the linear collision cascade theory the kinetic energy energy distributions of sputtered atoms is described by the Thompson formula [Th68]:

$$\frac{dY}{dE} \propto \frac{E}{(E+E_b)^3} \qquad (11.1)$$

In figures 11.1 and 11.2 a fit of the experimental data with Eq. (11.1) is shown as a dotted line. The surface binding energy E_b was used as the fitting parameter. The KED of monomers well fits the prediction of linear cascade theory for $E_b = 2.4\,\text{eV}$. The surface binding energy of atom to a surface is known only for a few materials, but it is common to use the heat of sublimation as an estimate. The sublimation energy of Indium is 2.6 eV, which is in good agreement with the E_b energy used in the fit.

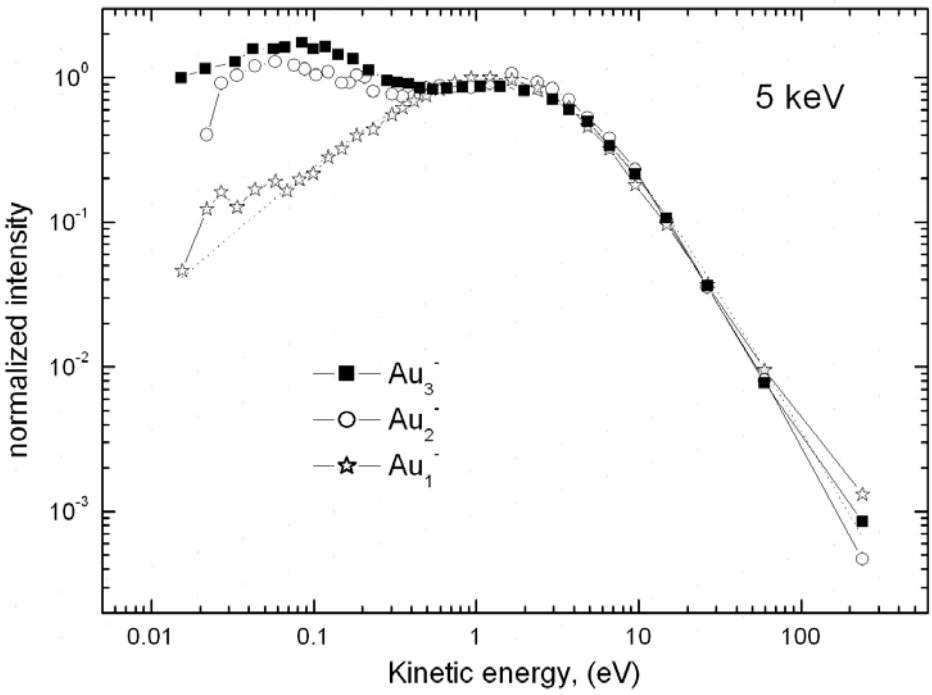

Fig. 11.1 Kinetic energy distributions of indium atoms sputtered by Au_1^-, Au_2^- and Au_3^- impinging particles with 5 keV kinetic energy. Dotted line: theoretical distribution of indium atoms calculated from Eq. (11.1) .

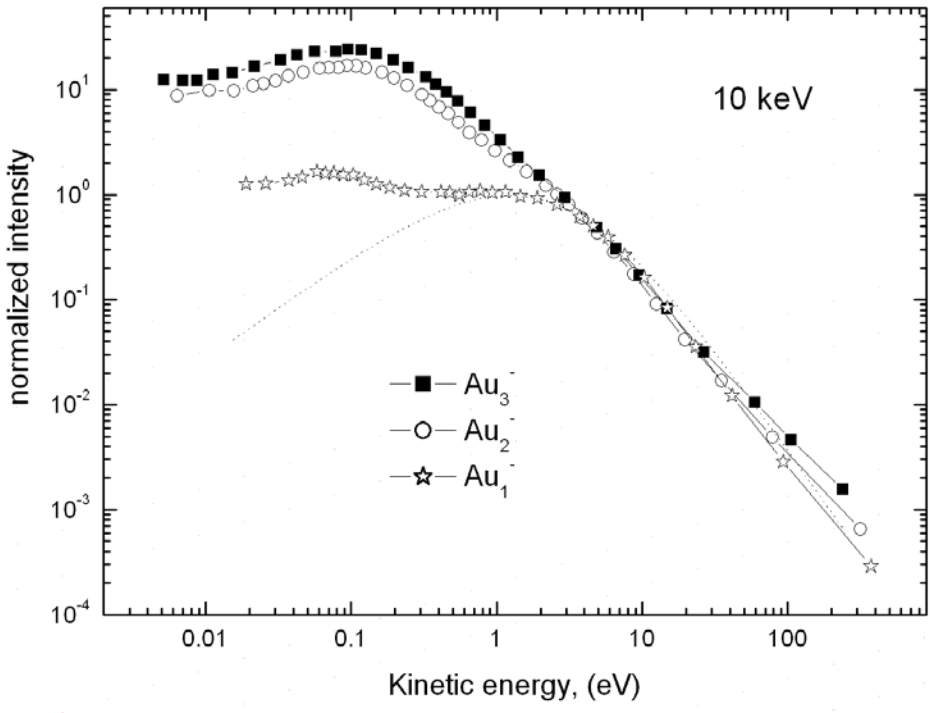

Fig. 11.2 Kinetic energy distributions of indium atoms sputtered by Au_1^-, Au_2^- and Au_3^- impinging particles with 10 keV kinetic energy. Dotted line: theoretical distribution of indium atoms calculated from Eq. (11.1).

For 5 keV kinetic energy ion bombardment (fig. 11.1) it is clearly seen that contributions from spikes are observed under polyatomic ion bombardment, and even under atomic irradiation with 5 keV there can be discerned a deviation of the KED in low energy range from the prediction of linear cascade theory. This deviation may be considered as a trace of atoms sputtered from the spike. For all types of projectiles high energy tails of KED of sputtered monomers exhibit an E^{-2} decay law which is, actually, the asymptotic dependence of Eq. (11.1) at large kinetic energies E. The same decay E^{-2} law of high energy tails is observed in KED's of indium monomers emitted under bombardment by all projectiles with impact energy 10 keV, indicating that there is always a contribution of atoms emitted in collision cascade mode of sputtering process.

In fig. 11.1, the KED of indium monomers have been normalized. Normalization is made using high energy tails of KED to coincide with Thompson distribution (Eq. 11.1) having the most probable kinetic energy at unity. The same procedure of normalization is made for the KED's of indium monomers produced under ion bombardment with 10 keV impact energy shown in fig. 11.2.

From fig. 11.2 it can be clearly observed that in the case of 10 keV projectile impact energy a considerable fraction of indium atoms are sputtered from spikes even under monoatomic ion bombardment. For polyatomic primary ions, it appears that the indium atoms are sputtered mostly from the spike. Like in the case of 5 keV impact energy, polyatomic ion bombardment produces significantly higher yields of atoms sputtered from the spike in comparison with monoatomic ion irradiation. On the other hand, the difference in the relative fraction of atoms emitted from the spike under di- and triatomic projectile bombardment is much less pronounced in comparison with the respective 5 keV data.

The data in fig. 11.1 and 11.2 therefore demonstrate the transition from a linear cascade sputtering mechanism (5 keV Au_1^-) to a spike dominated mechanism (10 keV Au_2^-, Au_3^-). Apparently the energy distributions in the latter case become independent of the projectile nuclearity. These observations are similar to those for the total yield data in the preceding chapter.

The data on the kinetic energy distributions of indium monomers may be utilized also for the sputtering yields determination. The laser postionization experiment is sensitive to the number density of sputtered neutral particles that are present in the ionization volume. Sputter yields, on the other hand, represent the flux of sputtered particles rather than their number density (chapter 8). In order to determine the yield distributions of sputtered clusters, the experimental data must therefore be converted from density to flux. The measured signal must be divided by an average inverse velocity defined by

$$< v^{-1} >= \frac{\int_0^\infty v^{-1} f(v) dv}{\int_0^\infty f(v) dv} \qquad (11.2)$$

for correction, where $f(v)$ denotes the velocity distribution of the emitted particles.

Using Eq. (11.2) the following mean values of inverse velocity of indium monomers sputtered by different projectiles are obtained from the measured KED and shown in Table 11.1.

	10 keV	5 keV
Au_1^-	$5.1\times10^{-4}\ (m/s)^{-1}$	$4\times10^{-4}\ (m/s)^{-1}$
Au_2^-	$1.1\times10^{-3}\ (m/s)^{-1}$	$5.2\times10^{-4}\ (m/s)^{-1}$
Au_3^-	$1.2\times10^{-3}\ (m/s)^{-1}$	$5.6\times10^{-4}\ (m/s)^{-1}$

Table 11.1. Inverse velocities of indium monomers sputtered by different projectiles with total impact energies of 10 and 5 keV.

Data in the table 11.1 was used in chapter 10 for correction of the signal to determine the sputtering yields under bombardment by atomic and polyatomic projectiles.

11.2 KED of atoms sputtered from the spike.

From fig. 11.1 it seen that the normalized KED of atoms sputtered from linear collision cascades look very similar for different projectiles. It is also seen that the distribution measured for 5 keV Au^- projectiles practically coincides with the prediction of linear cascade theory. Therefore, in order to determine the pure KED contribution of atoms originating from the collisional spikes, we can simply subtract the normalized KED corresponding to linear collision cascades from our experimental KED. Energy distributions of atoms sputtered from the spike produced in this way are shown on the fig. 11.3.

The same procedure can be applied to the KED of indium atoms measured under 10 keV ion bombardment. The corresponding experimental dependencies are shown in fig. 11.4.

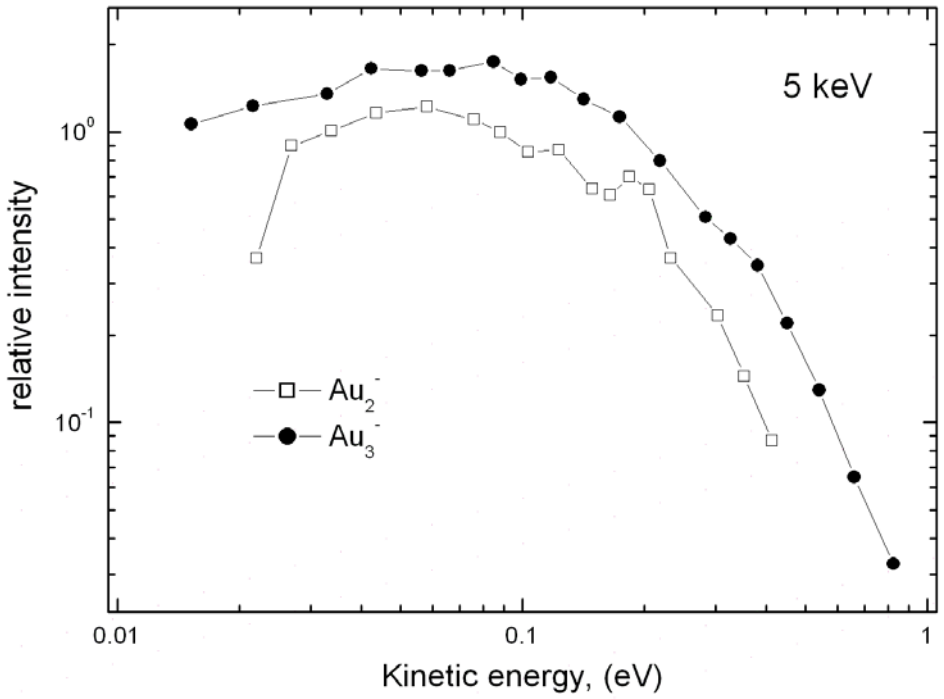

Fig. 11.3. Kinetic energy distributions of indium atoms sputtered from spike under polyatomic ion bombardment by Au_2^- and Au_3^- with 5 keV impact energy.

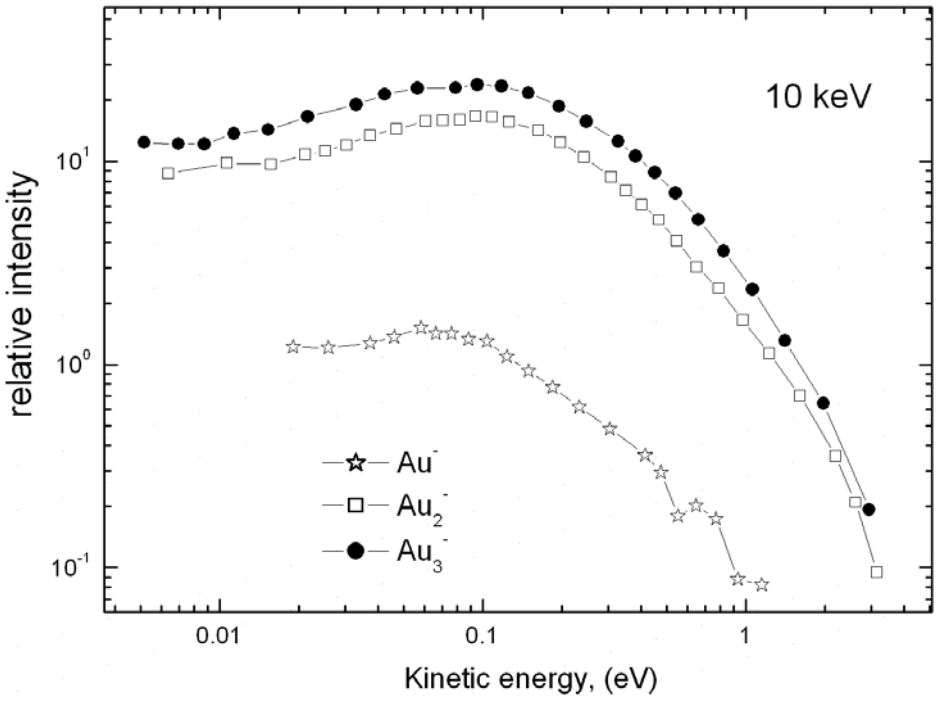

Fig. 11.4. Kinetic energy distributions of indium atoms sputtered from spike under polyatomic ion bombardment by Au_1^-, Au_2^- and Au_3^- with 10 keV impinging energy.

The fraction of atoms sputtered from the spike may be integrated and compared with the corresponding fraction of atoms sputtered from the linear collision cascade.
The following table shows the resulting ratio between total spike and cascade contributions for different impact energy and nuclearity of the projectile.

	5 keV	10 keV
Au_1^-	–	0.05
Au_2^-	0.03	0.96
Au_3^-	0.05	1.48

Table 11.2. Ratio between total integrated yield contributions for collisional spike to those sputtered from linear collision cascade.

From table 11.2 it is clearly observable that the fraction of atoms sputtered from collisional spikes increases with the increase of the mass and kinetic energy of the primary projectile. For the largest value of 1.48 observed for 10-keV Au_3^- ion bombardment, it is obvious that the majority of all sputtered atoms are emitted from spikes.
It is interesting to compare the yield enhancement factor measured during acquisition of the mass-spectra with the corresponding fraction of atoms sputtered from the spike determined here. When we assume that the non-additivity in the sputter yield is completely originating from the fraction of atoms sputtered from spikes, then, using the data in Table 11.2, we can calculate the enhancement factor $K_{2,1}$ at an impact energy of 5 keV per atom in the projectile to be:

$$K_{2,1} = \frac{Y_{lin} + Y_{spike}}{Y_{lin}} = \frac{1 + 0.96}{1} = 1.96$$

From mass-spectra measurements (chapter 9.2) $K_{2,1}$ = 2.1. Two different experimental techniques and data have lead to two values of $K_{2,1}$ which differ only by 10%. This finding constitutes a good agreement. The remaining difference can be caused by statistical errors.

11.3 Comparison with theories of sputtering from spikes

One of the first experimental evidence of an enhanced low energy part in the kinetic energy of sputtered atoms was detected by Szymonski & de Vries, who used electron impact post-ionization for detection of neutral sputtered atoms. In these experiments, Ag and Au surfaces were bombarded with 6 keV Xe. Later they also used an AgAu alloy as a target. Fig. 11.4 shows one of their energy spectra decomposed into a cascade part and a low energy Maxwell-Boltzmann-like part. Decomposition was performed after extrapolation of linear cascade part using Thompson formula [Th68] in the same way as done here. Experimental data of kinetic energy distributions of Ag and Au atoms sputtered from pure metal and alloy surfaces was treated in the frame of thermal spike model [Sz82].

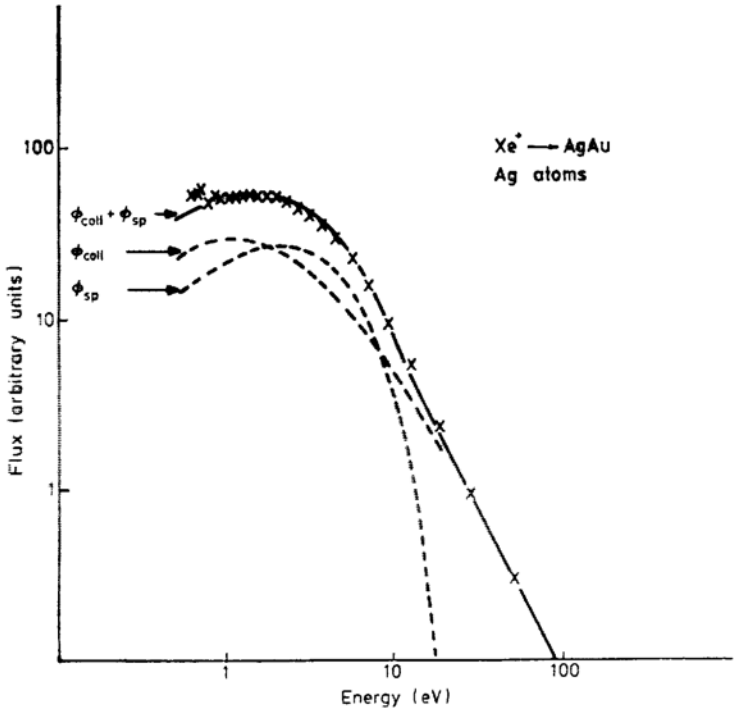

Fig.11.4 Energy spectra of silver atoms sputtered from an AgAu alloy by 6 keV Xe bombardment. (From Szymonski et al., 1978)

The spectra show the E^{-2} asymptotic behavior, at high emission energies which is typical for sputtering by momentum transfer in linear collision cascade. The kinetic energy distribution of particles sputtered from the spike was described by a Maxwell-Boltzmann distribution:

$$f(E) \propto E \cdot \exp\left(-3 \cdot E / 2 \cdot kT_{sp}\right) \qquad (11.3)$$

where T_{sp} is the temperature within a spike in quasi equilibrium conditions. The same procedure had been applied for analysis of the data from AgAu alloy.
The parameters extracted from their corresponding fits to the experimental data are displayed in table 11.3

Target	Measured particles	E_b (eV)	kT_{sp} (exp) (eV)
Ag		3.1	3
Au		3.8	3.65
AgAu	Ag Au	2.1 3.3	3.24 2.97

Table 11.3 Experimental and theoretical parameters of mean energy of the spike particles kT_{sp} [Sz78].

The KED data measured here fitted using Eq. (11.3) is presented in fig. 11.5 and 11.6. The resulting least square fits are included in the figures as dotted red lines. It is seen that the resulting thermal energy is always more than an order of magnitude lower in comparison with the maximum of the linear collision cascade part of the distributions – i.e. the halved value of indium surface binding energy. In contrast, the experimental values of kT_{sp} displayed in table 11.3 are of the same order or even exceed the surface binding energy E_b of metal surface in the case of $AgAu$ alloy.
It would be very interesting to compare these kinetic energy distributions of Ag atoms with ones measured by laser postionization technique, but existing data [Wu02b] was received under Ar^+ ion bombardment where spike effects may be reduced.
Basically, at the moment several models exist to explain the existence of an excess of low energy particles in the sputtered flux and a related enhancement in the yield. These theories consider the concept of collisional spikes. Some of these models treat the spike as a thermally overheated volume where evaporation from high temperature regions enhances the sputtering yield [Vi76],[Sz78], [Sz82], [Cl80]. Later, a gas-flow mechanism has been proposed [Mi83a], [Mi86], [Mi86] , [Ur87b], [Ke90], which describes the particle emission in terms of quasi-free expansion of a superheated, gasified volume.
In the following, we will discuss the published models based on these concepts particularly with respect to their prediction of the emission energy distribution of released atoms and compare these predictions with our experimental KED data displayed in fig. 11.3 and 11.4.
Thermal spike models have been used to describe the sputtering of metals and insulators for many years. In particular, this model has been also applied to the sputtering of weakly bound condensed gas solids [Ha85], [Ha85].
All thermal spike models in the more or less simplified way consider an energy transport from a region of the highest energy density into the surrounding solid. Thus, the corresponding temperature evolution in space and time during the duration of the spike should be described by the general heat conduction equation:

$$dT/dt = div\left[K(T) \cdot grad(T)\right] \qquad (11.4)$$

where t denotes the time variable, T is the temperature and $K(T)$ is the temperature dependent thermal diffusivity inside the spike.
Kelly [Ke90] has used an initial temperature distribution within the spike volume equivalent to a three dimensional Gaussian distribution of deposited energy with parameters obtained from linear cascade theory. He has used a constant thermal diffusivity coefficient K. Sigmund and Claussen [Cl80] have used a solution for cylindrical spike geometry in combination with a temperature dependent thermal diffusivity coefficient which was taken as for an ideal gas.
The number of particles sputtered from the spike surface, characterized by a temperature profile $T_{surf}(\rho,t)$ (ρ is the radius of the cylindrical spike) was obtained by integration of the evaporation rate

$$S_{sp} = \int_0^\infty dt \int_0^\infty \Phi\left(T_{surf}(\rho,t)\right) 2\pi\rho d\rho \qquad (11.5)$$

where

$$\Phi'(E,T,\theta) = \frac{N}{\sqrt{2\cdot M}(\pi kT)^{3/2}} E\cdot\exp\left[-(E+E_b)/kT\right]\cdot\cos(\theta) \qquad (11.6)$$

is the differential evaporation rate per unit energy and solid angle.
In following we will discuss the application of Sigmund-Claussen theory [Cl80] of thermal spikes to interpret the results.
Sigmund and Clausen, using the solution of Eq. (11.4) for cylindrical symmetry, after insertion of Eq. (11.6) into Eq. (11.5) have derived the differential sputtering yield:

$$Y_{th}(E,\theta)dEd^2\Omega = 0.0688\cdot\lambda_0\cdot\alpha^2\cdot F_{Dth}^2\cdot\frac{EdE}{(E+U)^4}\times f\left(\frac{E+U}{kT_0}\right)\cdot\cos(\theta)\cdot d^2\Omega \qquad (11.7)$$

where f is the function: $f(\xi) = \left(1+\xi+1/2\cdot\xi^2\right)\cdot\exp(-\xi)$, F_{Dth} - is a density of deposited energy in spike, U is surface binding energy, $\lambda_0 \cong 24$ and $\alpha \cong 0.219$ Å are Born-Meyer constants, k is a Boltzmann constant and T_0 is a core temperature at initial time.
Basically, kT_0 is a mean energy within a spike, which is related to F_{Dth} by:

$$kT_0 = F_{Dth}/2\pi N\left\langle\rho_0^2\right\rangle \qquad (11.8)$$

where N is a number density of material.
In the following figures 11.5 and 11.6 measured KED of atoms sputtered from spikes are fitted using Eq. (11.7) and Maxwell-Boltzmann distributions. From the figures we can observe that both Maxwell-Boltzmann distributions and kinetic energy distributions from Sigmund-Claussen model does not fit the experimental KED by showing a significantly different behavior of high energy "tails". The thermal spike models inevitably produce exponential high energy tails which are clearly by orders of magnitude at variance with our KED data.
In all cases the best fitting in the frame of model of Sigmund-Claussen using Eq. (11.7) was achieved when parameter kT_o was about 70-90 meV.

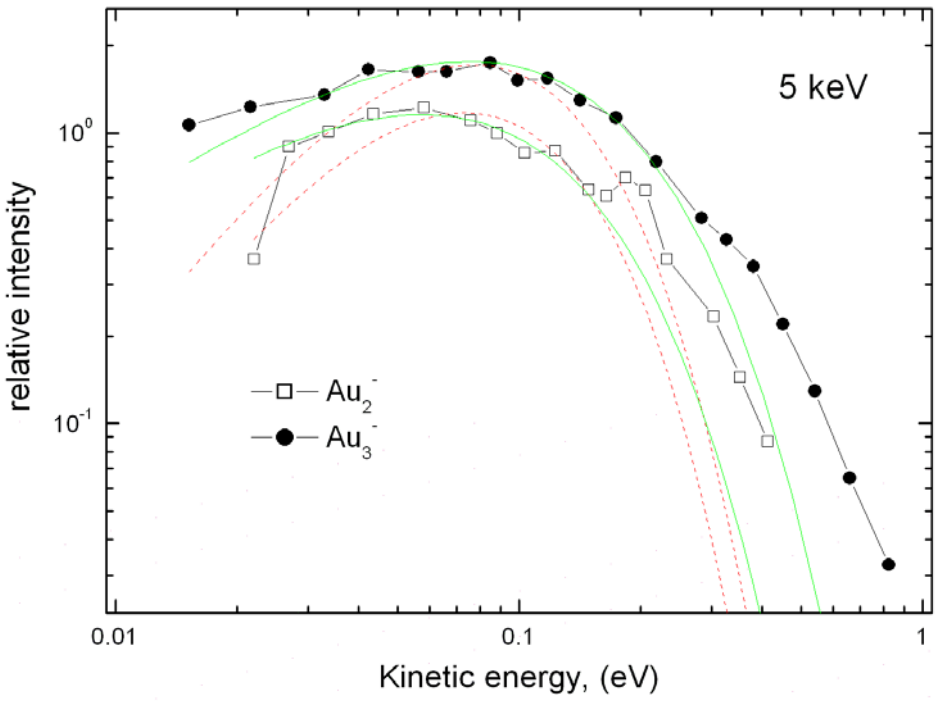

Fig. 11.5. Kinetic energy distributions of indium atoms sputtered from spike under polyatomic ion bombardment by Au_2^- and Au_3^- with 5 keV impinging energy with theoretical fitting of KED using Sigmund-Claussen model calculated from Eq. (11.7) (green solid line) and Maxwell-Boltzmann distribution (red dash line).

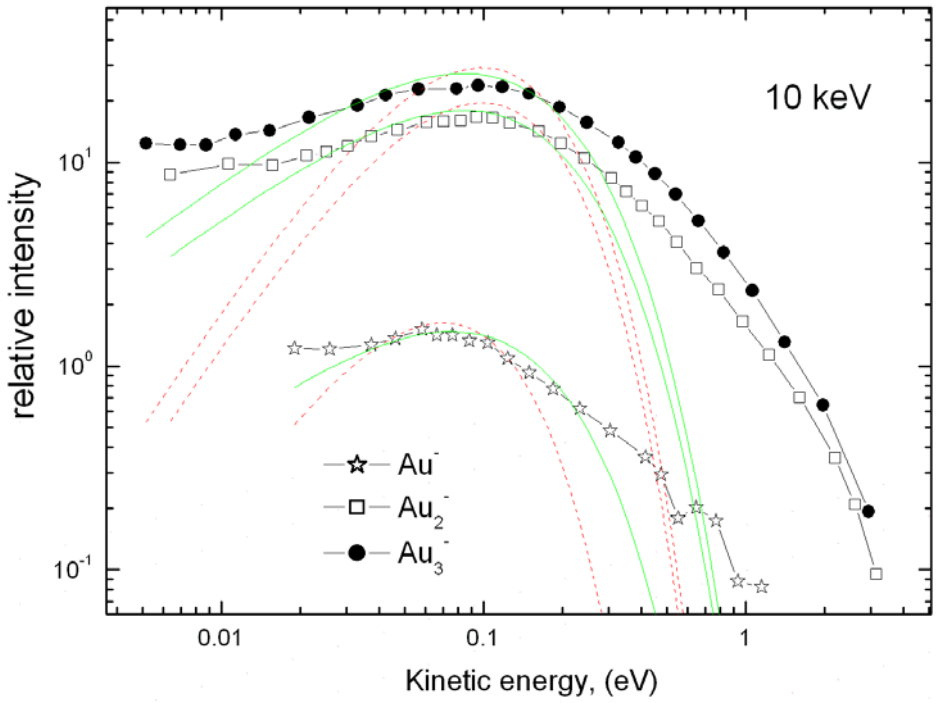

Fig. 11.6. Kinetic energy distributions of indium atoms sputtered from spike under polyatomic ion bombardment by Au_1^-, Au_2^- and Au_3^- with 10 keV impinging energy with theoretical fitting of KED using Sigmund-Claussen model calculated from Eq. (11.7) (green solid line) and Maxwell-Boltzmann distribution (red dash line).

In the theory, the total sputtering yield is considered as the sum of two contributions from thermal spike Y_{th} and from linear collision cascades Y_{lin}. The ratio of the thermal spikes yield, Y_{th}, and the linear yield Y_{lin} is written in the form:

$$\frac{Y_{th}}{Y_{lin}} = 15.37 \cdot N^2 \cdot \left(\lambda_0 \cdot \alpha^2\right)^3 \left(\frac{F_{Dth}}{F_{Dlin}}\right)^2 g\left(\frac{U}{kT_0}\right) \cdot Y_{lin} \quad (11.9)$$

where F_{Dlin} is a density of deposited energy in linear cascade mode of sputtering and g is a function $g(\xi) = \left(1 + \xi - \xi^2\right) \cdot \exp(-\xi) + \xi^2 \int_{\xi}^{\infty} dt \cdot e^{-t}/t$. Taking $N \approx 0.04$ Å^{-3} for indium and $F_{Dth} \cong F_{Dlin}$, Eq. (11.9) reads:

$$Y_{th}/Y_{lin} \cong 0.04 \cdot Y_{lin} \cdot g\left(U/kT_0\right) \qquad (11.10)$$

Using Eq. (11.10) one can compare the ratio between the spike and linear cascade sputtering contributions in the yield predicted by Sigmund-Claussen theory and experimental ratios in table 11.2. For instance, we perform the comparison for Au_3^- bombardment with 10 keV impact energy.

The sputtering yield from linear cascades must be equal to triple the yield produced by monoatomic Au^- ions with energy 3.3 keV, which can be obtained from TRIM calculations. TRIM shows that Y_{lin} in this case is $9.5 \times 3 = 28.5$ atoms/projectile. The core temperature kT_0 obtained from the fitting is 90 meV. As surface binding energy we can take the sublimation energy of indium equal to 2.6 eV. Inserting all these parameters into Eq. (11.10) we obtain the prediction from the theory for $Y_{th}/Y_{lin} = 6 \cdot 10^{-11}$, while we get $Y_{th}/Y_{lin} = 1.48$ in the experiment.

Such drastic disagreement between Sigmund-Claussen theory and experimental data may be qualitatively explained by the fact that the mean energy kT_0 within spike obtained from fitting the experimental KED is significantly lower in comparison with the binding energy of the material. In order to produce a substantial contribution of the sputtering yield from thermal spike, this energy, in the frame of the theory, must be comparable with the surface binding energy. Moreover, the experimental ratios Y_{th}/Y_{lin} from table 11.2 obtained for Au_2^- and Au_3^- with 5 keV and 10 keV impact energies are different from each other by a factor of about 50. From Eq. (11.9), in this case, the mean energy kT_0 within spike under bombardment by Au_2^- projectile with 5 keV impact energy must be lower by the factor about 2.5 from the one obtained under bombardment by Au_3^- projectile with 10 keV. The fittings of experimental KED by Eq. (11.7) show that these parameters differ from each by factor of ≈ 1.3.

In the gas-flow models it is assumed that after spreading of the bombarding energy by the collision cascade, and after some amount of collisional sputtering occurred, a part of solid has received enough energy to bring it above the critical point. In that gaseous state, the volume is free to flow into the vacuum, until the energy dissipation to the surroundings and the subsequent recondensation at the crater walls stop the expansion. Such a gas-flow mechanism is the natural extension of the evaporative spike concept towards high initial energy densities. It acknowledges the fact that the material is not in thermal equilibrium at the high temperature, since such equilibrium would require extremely high pressure to

keep the gas compressed at the large number density typical for the solid phase. As a consequence of the huge pressure in the cascade volume, the material therefore expands into the vacuum.
Numerical simulation of the thermodynamics and hydrodynamics of the process, together with appropriate boundary conditions at the moving solid-gas interface, poses a nontrivial problem.
H.M. Urbassek developed a simplified gas flow model based on the description of the expansion process as a *collision-free molecular flow* (cmf) in which the gas particles are modeled to move without collisions. This model was successfully applied to the description of yields and energy spectra of atoms sputtered from the surface of condensed rare gases [Ur87b]. Basically, sputtering of condensed gases provides appropriate conditions for the application of this model, since these materials have extremely low boiling point and the mean energy per atom can easily be high enough to bring the cascade volume above the critical point, where this mechanism of sputtering is supposed to be dominant. In [Ur87b], the cmf model was extended to a full three dimensional description, including the effects of energy dissipation and recondensation at the crater walls.
The final equation for the kinetic energy distribution of atoms sputtered in the gas flow model is as: [Ur87b]

$$F(E) \propto \frac{1}{\sqrt{\pi \cdot \varepsilon \cdot \varepsilon^*}\,\varepsilon} \cdot \left[\gamma\left(\tfrac{5}{2}, \varepsilon\left(1 + t_c/t_0\right)\right) - \gamma\left(\tfrac{5}{2}, \varepsilon\right)\right] \qquad (11.11)$$

for small values of $\varepsilon < \varepsilon^*$. In Eq. (11.11) $\varepsilon = E/kT$ is the reduced energy, k is Boltzmann constant and

$$\gamma(5/2, x) = \int_0^x d\xi \cdot \xi^{3/2} \cdot \exp(-\xi) = 3/4 \cdot \sqrt{\pi} \cdot erf\left(\sqrt{x}\right) - \sqrt{x} \cdot \exp(-x) \cdot (x + 3/2)$$

is the incomplete gamma function. The reduced critical energy

$$\varepsilon^* = \frac{M\left(l/t_0\right)^2}{2kT_0}$$

corresponds to a particle moving with critical speed $v^* = l/t_0$, travelling the cascade depth in the "quenching time" t_0. The physical meaning of t_0 is a time constant describing the dissipation of energy out of cascade volume into the bulk of the crystal by a power law: $E = E_0 \cdot \left(\frac{t + t_0}{t_0}\right)^{-\nu}$. For cylindrical initial energy dissipation the parameter $\nu = 1$.
The quantity $1 + t_c/t_0 = \left(T_0/T_{con}\right)^{1/\nu}$ approximately determines the time t_c at which freezing (recondensation) starts. Here T_0 is the initial temperature of the energized volume and T_{con} is the temperature of condensation.
Results on the kinetic energy distributions of neutral atoms sputtered from condensed rare gases under Ar^+, Xe^+ and Kr^+ ion bombardment from [Ha85] showed that an excess of particles emitted with kinetic energies significantly below the target sublimation energy is responsible for the high sputter yield. In [Ur87b], the gas flow model was applied to fit these results. The model produced rather good agreement for both the yields and energy

distributions. In particular, it was demonstrated, that this model reproduces the correct shape of the energy distribution, thereby bringing its maximum to low energies.
The spike contribution of kinetic energy distributions of indium atoms sputtered by the projectiles Au_1^-, Au_2^-, Au_3^- with impact energy 10 keV shown in fig. 11.6 are fitted using Eq. (11.11). As variable parameters, the initial temperature of the gasified volume of the spike T_0 and the temperature of recondensation T_{con} were used. The corresponding fits are shown in fig. 11.7. In the case of di- and triatomic Au_2^-, Au_3^- projectiles the best fitting is performed when initial temperature T_0 is chosen as 18000 K and the recondensation temperature T_{con} = 700 K. For monoatomic Au_1^- projectiles the parameters T_0 and T_{con} were set to 9000 and 650 respectively.
From the fits it is seen that our experimental data is in much better agreement with the theoretical prediction from equation 11.4 in comparison with the Maxwellian energy distribution.
The magnitude of the initial temperature T_0 of the spike volume obtained from the fits in all cases is larger than the critical temperature of indium which is equal to 6323 K. According to [Ur87b] the initial temperature in the volume of cascade may be estimated by:

$$T_0 = \frac{S}{\pi \cdot C \cdot \rho_\perp^2} \qquad (11.12)$$

where S is the stopping power, $C = 3/2 \cdot N_0 \cdot k$ is the heat capacity of material, and $\rho_\perp$ is lateral width of the energized volume. The width $\rho_\perp$ we will take equal 30 $\mathring{A}$ which is about the mean dimension of emission area obtained from MD simulations [Li01]. The stopping power S values may be obtained from SRIM 2003 calculations. At the impact energy of 10 keV and 45 degree incident angle the stopping power S is equal to 97, 246, and 297 eV/$\mathring{A}$ for Au_1^-, Au_2^-, Au_3^- projectiles respectively. Inserting these values into Eq. (11.12) we obtain T_0 to be equal to 6800, 17000, and 20400 K for Au_1^-, Au_2^-, Au_3^- projectiles respectively. These temperatures are in agreement in the range of order of magnitude with those values obtained from fittings.
In [Ur87b] the parameter T_{con} was estimated to be equal to the boiling temperature of material. In our fittings this parameter is within the range in between the boiling temperature of indium (2345 K) and its melting temperature (430 K).
As it stated earlier the gas flow model was developed for description of sputtering process of frozen noble gases. The condensed noble gases have low values of the critical temperatures and projectile having impact kinetic energy in the range of few keV after initial collisions can easily bring the cascade volume in the gaseous state which is free to flow in the vacuum. For other materials, for instance for metals, which have large binding energy and critical temperature of several thousand Kelvin it was supposed that emission from the spike must have evaporational nature and material is assumed to remain in the condensed phase. The experimental data presented here manifest that at least in the case of indium the emission from a spike can be explained by a model considering the emission from gasified volume.

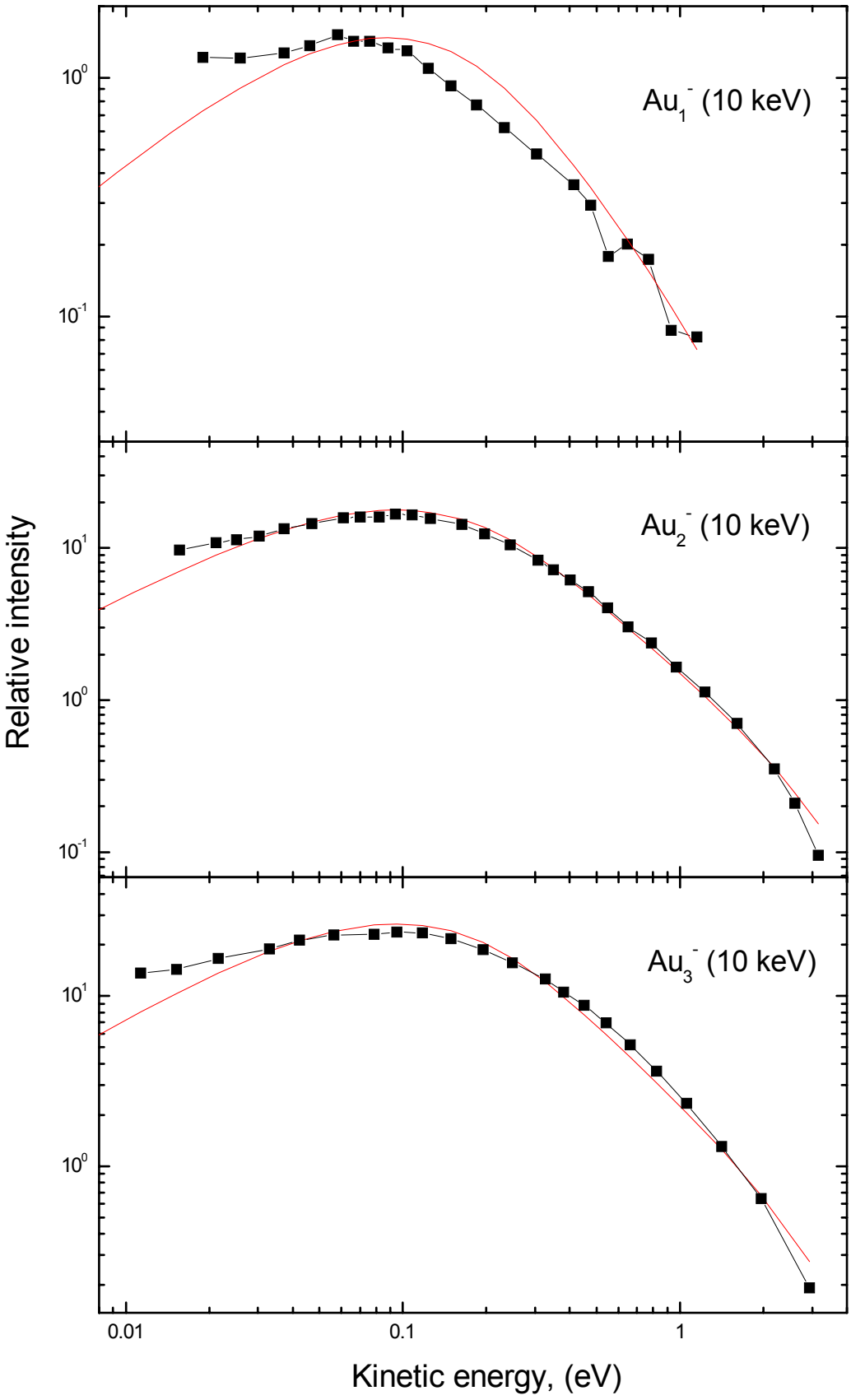

Fig. 11.7 Energy spectra in arbitrary units: measured and calculated (equation 11.11)

12 Ionization Probabilities

As outlined in section 7, the secondary ion formation or ionization probability of sputtered particles is determined from a direct comparison of secondary ion and neutral signals. Details of the experimental method used to measure the ionization probabilities α^+ are described in chapter 7.2. These experiments are performed under saturation postionization conditions using long primary ion pulses. The resulting α^+ therefore represent mean values of the – in general energy dependent – ionization probability averaged over all emission energies. A direct determination of the differential ionization probability:

$$\alpha^+(E) = \frac{f_{X^+}(E)}{f_{X^0}(E) + f_{X^-}(E) + f_{X^+}(E)}$$

is difficult since the method usually employed to determine the neutral energy distribution $f_{X^0}(E)$ relies on tuning the delay between projectile and postionization laser pulse and therefore does not work for secondary ions.

The resulting energy averaged ionization probabilities α^+ of sputtered Indium atoms sputtered by mono and polyatomic projectiles Au_1^-, Au_2^-, Au_3^- with total kinetic energies of 5 and 10 keV are shown in fig. 12.2.

It is assumed in this experiment that the surface concentration of gold atoms, which is induced by the projectiles and will in general depend on the projectile nuclearity, does not influence the ionization probability of indium atoms significantly under bombardment by projectiles with different nuclearity. This assumption is supported by the fact that no dynamic changes of the secondary ion signal have been observed in time after changing the projectile type.

The main conclusion from the data depicted in fig. 12.2 is that the ionization probability of sputtered In monomers is lower for polyatomic ion bombardment with Au_2^-, Au_3^- in comparison with monoatomic projectiles Au_1^-. Moreover, comparing the ionization probabilities of indium atoms sputtered by poly- and monoatomic projectiles having the same impact velocity (Au_2^- with 10 keV and Au_1^- with 5 keV), it is seen that in the case of diatomic ion bombardment the ionization probability is lower by a factor ≥ 2. Therefore, in contrast to the overlinear enhancement observed for the sputtering yields, we observe a sublinear decrease of the ionization probability with increasing projectile nuclearity.

At the moment there is no systematic information in the literature about the expected dependence of the ionization probability on projectile parameters such as mass and nuclearity.

In general, ionization probabilities of adatoms and target atoms sputtered from a metal surface have revealed a strong dependence on several parameters. Experimentally [Yu78], [Yu79], [Yu82] it was found that the measured ionization probability is exponentially depending on a work function change $\Delta\phi$ of the surface. As a result, a simple exponential relation is frequently found according to:

$$\alpha^+ \propto \exp(\Delta\phi/\varepsilon_p) \qquad (12.1)$$

for positive and

$$\alpha^- \propto \exp(-\Delta\phi/\varepsilon_n) \qquad (12.2)$$

for negative ionization. Here, ε_p and ε_n are parameters specific to the system and can be functions of the emission velocity or energy and angle. Investigations of the ionization probability in dependence on the emission energy and angle [No78], [Yu81] revealed an exponential dependence of α^+ on the inverse normal emission velocity for the higher-energy part of the ion energy spectrum as:

$$\alpha^+ \propto \exp(-v_0/v_\perp) \qquad (12.3)$$

with $v_0 \approx 10^7$ cm/s. At low emission velocities, deviations from this simple relation were observed [Wu87b], [Ur95].
Several theoretical models of the ion formation have been developed up to now.
The electron-tunneling model is the most known and comprehensive secondary ion emission model developed so far. In this model charge transfer between atomic level ε_a and delocalized states of valence band of the metal is considered (see fig. 12.1).

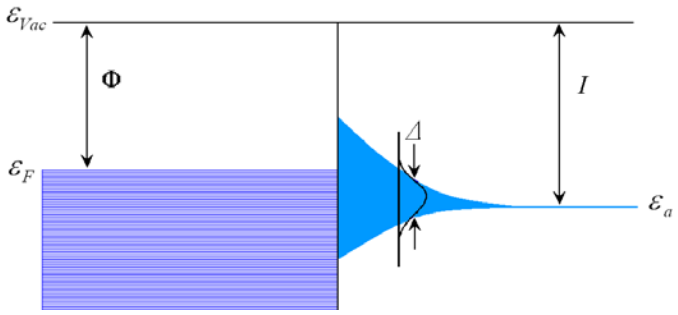

Fig. 12.1 Energy diagram of metal surface and emitted atom.

In its simplest form, the metal is represented by a nearly-free-electron valence band with constant density of states and a work function ϕ at zero temperature. The theory successfully explains several features such as the work function and, within restrictions, emission velocity dependence in the sputtering of atomic species from a metal surface [Yu78], [Yu79], [La83]. An analytical expression of the ionization probability in the electron-tunneling model may be derived for a few limiting cases. According to Blandin et al. [Bl76], for a constant valence energy level ε_a of the emitted atom and large $v_\perp$ the ionization probability is given by:

$$\alpha^+ \cong \frac{1}{2} + \frac{|\varepsilon_a - \varepsilon_F|}{\hbar \cdot \gamma \cdot v_\perp} \qquad (12.4)$$

for large $v_\perp$, and

$$\alpha^+ \cong \frac{2}{\pi} \exp\left(- \frac{\pi \cdot |\varepsilon_a - \varepsilon_F|}{\hbar \cdot \gamma \cdot v_\perp} \right) \qquad (12.5)$$

where γ is a denotes a characteristic length scale of the interaction range above the surface, and ε_F is the Fermi level.

Eq. (12.4) is valid for $\frac{|\varepsilon_a - \varepsilon_F|}{\hbar \cdot \gamma \cdot v_\perp} << 1$ and relates to very large emission energies which are not applicable for sputtered particles. Therefore, we are left with Eq. (12.5), where $\varepsilon_F < \varepsilon_a$ (as valid for In atoms sputtered from an indium metal surface). This derives again the exponential dependence of Eq. (12.3) with $v_0 = \frac{\pi |\varepsilon_a - \varepsilon_F|}{\hbar \cdot \gamma}$.

In the electron-tunneling model, the ionization step is completely decoupled from the mechanics of sputtering. The function of the incident ion in this case is to provide the energy for the ejection of a surface atom. Wittmaack [Wi75] found only a weak dependence of the ionization probabilities on the kinetic energy of the impinging projectile in the keV range for secondary ions emitted from a metallic target. The result in fig. 12.2 shows a similarly weak dependence on the impact energy.

In general, the valence energy level ε_a is dependent on the distance normal z of the outgoing particle to the surface (fig. 12.1). This valence level is broadened because of its interaction with the metal states. If $\Delta(z)$ denotes the corresponding half width (cf. Fig.12.1), then $\Delta(z)$ is usually taken to decay exponentially as:

$$\Delta(z) = \Delta_0 \cdot \exp(-\lambda \cdot z) \qquad (12.6)$$

where Δ_0 and λ are characteristic parameters. When the sputtered atom is far from surface, that energy level ε_a is located at the ionization potential *I* below the vacuum level. For atom positions closer to the surface, ε_a is higher because of the image charge an ion feels above a metal surface. Therefore, if ε_a varies rapidly with *z* and crosses ε_F at the distance z_c, α^+ can exhibit an exponential dependence on both $\Delta(z_c)$ and $v_\perp$:

$$\alpha^+ \propto \exp\left(\frac{-2 \cdot \Delta(z_c)}{\hbar \cdot \gamma \cdot v_\perp(z_c)}\right) \qquad (12.7)$$

It should be noted that for the specific case of metal atom sputtered from the same metal surface, the concept behind Eq. (12.7) (ε_a crossing the Fermi level) is questionable, since z_c is ill defined.

It should be noted that published quantum mechanical models describing the ionization as a result of the non-adiabatic passage of the sputtered particle across the surface from the solid to a vacuum environment yield similar exponential expressions as Eq. (12.7) for α^+ [Sr99]. This is due to the fact that the energy deficit for ionization ΔE, which can be expressed as the difference between the ionization energy of the particle and the Fermi energy ($|\varepsilon_a - \varepsilon_F|$) or the necessary broadening of the atomic level (Δ), must be compared to the energy uncertainty ($\hbar \cdot \gamma \cdot v_\perp$) induced by the dynamics of the process. As a common feature of all published models, the pre-exponential factor in Eq. (12.1)-(12.7) is fixed and of the order of unity and the parameter γ describing the typical length scale for the electronic interaction between the outgoing particle and the of the order of 1 Å^{-1}.

For the present case of *I*=5.6 eV and ϕ=4.1 eV we can estimate the parameter v_0 as $v_0 \cong 7 \times 10^7$ cm/s. Inserting this into Eq. (12.5), from our experimental data on the

velocity distributions $f(v)$ of indium monomers we can calculate the prediction of the theory of the mean ionization probability averaged over all emission velocities by:

$$\left\langle \alpha^{+} \right\rangle = \frac{\int f(v) \cdot \alpha(v) \cdot dv}{\int f(v) \cdot dv} \qquad (12.7)$$

The mean ionization probabilities calculated this way are presented in following table.

	5 keV	10 keV
Au^-	2.4×10^{-18}	2×10^{-15}
Au_2^-	4.1×10^{-19}	1.6×10^{-16}
Au_3^-	8.1×10^{-33}	1.5×10^{-18}

Table 12.1. The mean ionization probabilities predicted by electron tunneling model.

In table 12.1 we can observe that the ionization probabilities predicted by theory are by more than ten orders of magnitude lower than the experimental data. Moreover, the predicted values vary in the range of several orders of magnitude, while the experimentally determined ionization probabilities for different projectiles are within one order of magnitude.
Therefore, quantum mechanical models leading to expressions like Eq. (12.5) cannot explain our data. A non-adiabatic approach of these models considering an unperturbed solid state surface cannot fully explain many experimental observations on ion formation in sputtering [Sr99]. The exponential term of Eq. (12.5) leads to the fact that for systems with a large value v_0 and for particles ejected with very low velocities, i.e. for large $v_0/v_\perp$, the value of α^+ becomes very small and much more sensitive to the relative changes of the emission velocities than observed experimentally. Therefore, changes in the emission velocity spectrum under polyatomic Au_3^- bombardment with impact energy of 10 keV lead to changes in the ionization probabilities by a factor of 10^3 (table 12.1). In addition, the strong $v_\perp$ - dependence (or kinetic energy dependence) for particles with very low ionization probabilities would lead to a significant broadening and a large shift of the secondary ion energy distribution with respect to that of the sputtered neutrals, a prediction which is not observed experimentally. Therefore the ionization of particles emitted with low velocities (kinetic energies) is strongly underestimated by these theories.
In the non-adiabatic approaches it is assumed that the solid is electronically unperturbed due to the fact that all electronic excitations created in the collision cascade are rapidly relaxed and do not influence the ionization process. As has been pointed out by Shroubek and collaborators [Sr99], [Sr89a] this assumption is probably unrealistic in a sputtering event. As a consequence, a different class of models has been developed, in which the electronic excitation of the solid is taken into account. The model relies on the following two assumptions:

- In the volume of collision cascade the solid is strongly amorphized, leading to a corresponding disturbed band structure.
- Electronic excitation occurs via the kinetic excitation of electrons due to the particle dynamics within the collision cascade.

A proper theoretical analysis of electronic excitations require an analysis of many – electron interaction processes and the mechanism of localization of the excitation in a highly disordered and amorphous solid. This precise analysis is not firmly developed yet. Sroubek et al. [Sr99], [Sr89a] have studied the influence of electronic excitation on the ionization process. To describe the substrate excitations they introduces a simplifying concept of a temporarily raised electron temperature T_e. Assuming that Eq. (12.7) is obtained for $T_e = 0$, then to obtain an analogue expression for $T_e \neq 0$ the ionization process is described by a semiclassical rate equation for the occupation number $n_a(t)$ of the atomic level ε_a:

$$\frac{dn_a}{dt} = -\left[n_a(t) - n_0(t)\right]/\tau(t) \qquad (12.8)$$

where $\tau(t) = \hbar/2\Delta(t) = (\hbar/2\Delta_0)\cdot\exp(-\gamma\cdot v\cdot t)$ and $n_0(t)$ is the equilibrium Fermi-Dirac distribution at the energy ε_a and temperature T_e.

The analytical solution of Eq. (12.8) in the approximation that the ionization energy ε_a remains below the Fermi energy (which is fulfilled in our case) is the following:

$$\alpha^+ = \exp\left(-\frac{2\Delta_0}{\hbar\cdot\gamma\cdot v_\perp}\right) + \exp\left(-\frac{\varepsilon_a(z^*) - \phi}{k\cdot T_e}\right) \qquad (12.9)$$

where $z^* = \frac{1}{\gamma}\lg\left(\frac{2\cdot\Delta_0}{\hbar\cdot\gamma\cdot v_\perp}\right)$.

The first term of Eq. (12.9) is the same as Eq. (12.7). It decreases rapidly with decreasing $v_\perp$, and thus the second term in Eq. (12.9) can dominate at low $v_\perp$.

An evaluation of T_e by analyzing the measured work function dependence of ionization probabilities in various systems reveals temperatures of several thousand Kelvin [Sr82]. Moreover, crude theoretical estimations have shown that transient electron temperatures of this magnitude appear reasonable in atomic collision cascades [Sr89b].

In the frame of this model, the characteristic influence of polyatomic ion bombardment on the ionization process must correspond to a change in the electron temperature T_e. From our experimental data in fig. 12.2, the observed sublinear decrease of the ionization probability under polyatomic ion bombardment means that the electronic excitation characterized by T_e must be lower. Qualitatively this result is in accordance with the experimental data on ion induced electron emission under polyatomic Au_m^- $(1 \le m \le 4)$ ion bombardment in a wide range of impact energies between 30 keV/atom and 6000 keV/atom from a *CsI* surface [Le98]. It was shown in these experiments, that in the whole range of impact energies the ratio $\frac{\delta_m}{\delta_1\cdot m}$ of secondary electron yields under monoatomic ion bombardment (δ_1) and polyatomic ion bombardment (δ_m) is always lower than unity. Moreover, this ratio decreases with increasing projectile nuclearity m reaching 0.5 for $m = 4$.

Kinetic electron emission phenomena may occur in a solid by direct transfer of kinetic energy from the impinging projectiles to the electrons in the target material (kinetic excitation). Therefore, lower secondary electron yields under polyatomic projectile

impact must reflect a quantitatively lower energy transfer from projectile and fast recoils into the electronic subsystem. In agreement with the electron emission data collected by the Orsay group, our data on ionization probabilities therefore indicate a decrease of the electron temperature T_e with increasing projectile nuclearity. It should be noted that this finding is in contradiction with [Be01b], [Be02], [Be03a], [Be03b] publications.

This approach to study ionization probabilities under polyatomic ion bombardment was based on the analysis of experimental kinetic energy distributions of secondary ions sputtered from various surfaces (Si, Ta, Nb). In the analysis it was assumed that the KED of neutral atoms does not change under polyatomic ion irradiation and described by the Thompson Eq. (11.1). The ionization process of atomic species was then considered in the frame of the electron tunneling model. Using the prediction from the Thompson equation on the KED of neutrals under polyatomic ion bombardment and taking the same equation as Eq. (12.3) the parameters v_0 have been obtained for various samples and projectiles. It was shown that v_0 is decreasing with increasing projectile nuclearity and, therefore, it was inferred that the ionization probability must increase. Note that the values v_0 obtained this way are even for monoatomic ion bombardment by a factor of about one order of magnitude lower than predicted by theory (see above).

This approach is questionable, since the KED of neutral atoms are not described well by the prediction of linear cascade theory (cf. section 11.1), moreover, the direct measurements made here show that the ionization probability of atoms sputtered from indium metal surface does not increase with increasing nuclearity of projectile. The new experimental data collected in this thesis, therefore, provide direct evidence against the conclusion of an enhanced electronic excitation of the solid under polyatomic projectile bombardment, which was drawn in these publications.

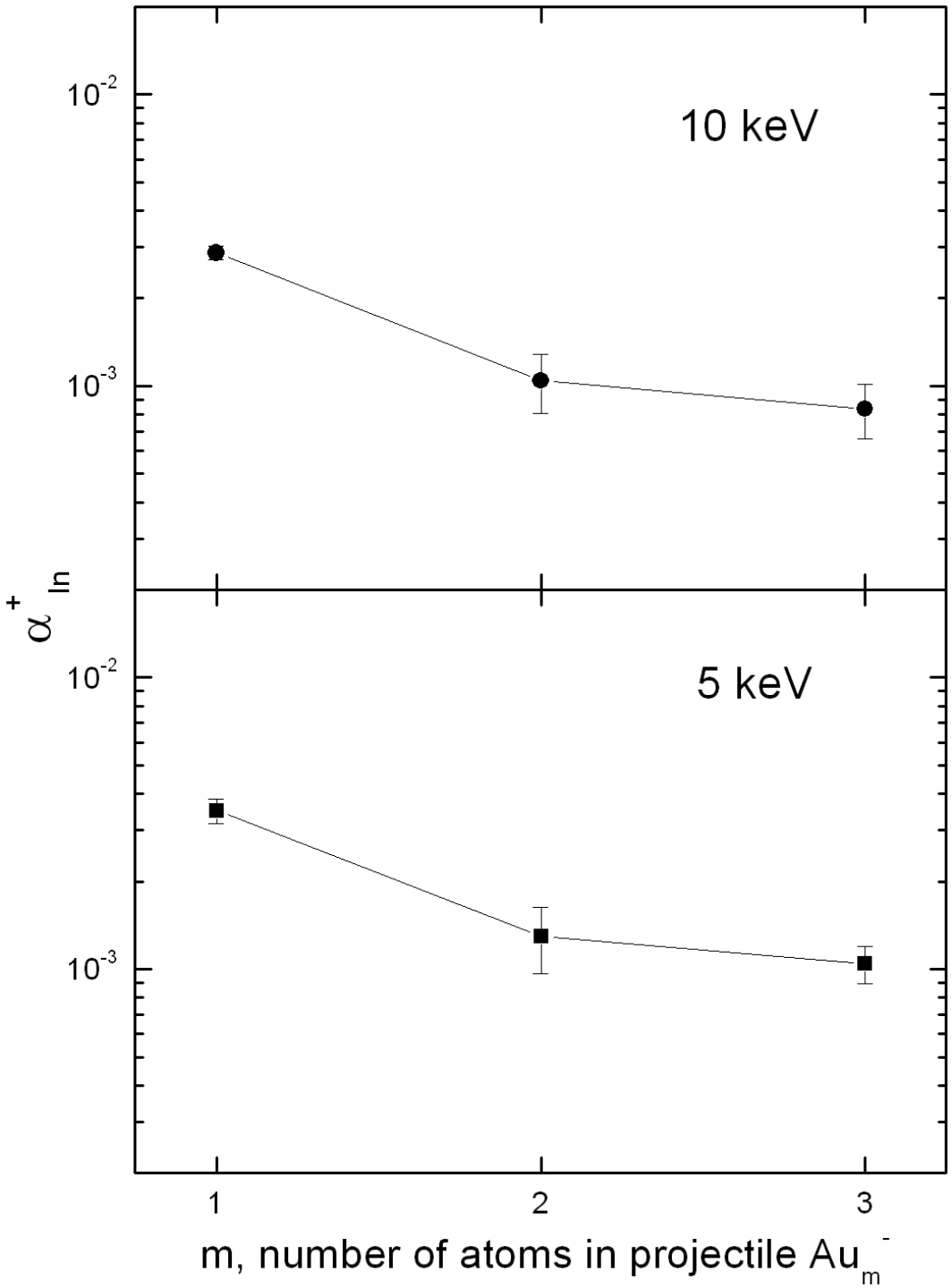

Fig. 12.2 Ionization probabilities of Indium atoms sputtered by different projectiles Au_1^-, Au_2^-, Au_3^- with kinetic energies 5 and 10 keV.

SUMMARY

The main goal of the present study is the investigation of the sputtering of neutral particles from a metal surface under atomic and polyatomic ion bombardment using secondary neutral time-of-flight mass spectrometry (ToF SNMS). For postionization of neutral species, UV laser irradiation with wavelength 193 nm was utilized. For generation of polyatomic projectiles, a negative sputter cesium ion source suitable for ToF SNMS setup was developed and built. The ion source delivers negatively charged Au_m^- (m=1÷5) and $AuCs_2$ polyatomic ions produced from a gold sputter target bombarded by positive Cs^+ ions. Mass separation of primary projectiles in the ion source is performed by a built-in compact Wien filter allowing to separate heavy ions in the energy range of several keV. In the experiment, an indium surface was bombarded by Au_m^- (m=1÷5) projectiles with total impact energy of 5 and 10 keV. The obtained mass distributions of sputtered indium species reveal that the partial yields of sputtered clusters increase under polyatomic ion bombardment. It is shown that the enhancement in total sputtering yield per constituent atom of the projectile ion is non-additively enhanced in the case of diatomic ion bombardment in comparison with monoatomic projectile ions impinging at the same velocity. The enhancement of partial yields observed for sputtered clusters is found to increase with increasing cluster size, reaching a factor of several ten for the largest detected cluster.

Apart from sputtering yields, kinetic energy distributions (KED) of sputtered neutral indium atoms ejected under mono- and polyatomic projectile ion bombardment were measured. It is shown that In monomers sputtered by monoatomic Au_1^- projectiles with an impact energy of 5 keV are emitted mostly from linear collision cascades. At higher kinetic energy, or polyatomic projectile impact, it is revealed that in addition to the atoms sputtered from the linear cascade, a low energetic contribution of atoms sputtered from a collisional spike appears. This contribution in the KED increases with increasing impact energy and nuclearity of projectile. In the case of 10-keV Au_3^- projectiles, the sputtering process is shown to be dominated by the spike contribution. By subtracting the linear cascade contribution from the measured KED, the pure emission energy spectrum produced by the collisional spike is identified. It is found that the most probable emission energy of atoms emitted from the spike is more than one order of magnitude lower in comparison with the surface binding energy of indium. The obtained KED of indium monomers emitted from the spike were interpreted in terms of published theoretical models of the sputtering process from a spike. It is shown that the obtained data cannot be explained in terms of a thermal spike model. The obtained results are shown to agree more favorably with a thermodynamic gas flow model describing the particle emission process as a quasi-free expansion of a superheated near-surface volume.

By comparing the partial sputtering yields of emitted secondary ions and their neutral counterparts, the ionization probabilities of indium atoms sputtered by atomic and polyatomic projectiles were measured. It is revealed that ionization probabilities of sputtered In monomers decrease when polyatomic projectiles are utilized. Data of this kind are of great interest both from a fundamental perspective and for practical applications of Secondary Ion Mass Spectrometry (SIMS) in surface analysis. The measured data are interpreted in terms of published theories of secondary ion formation. Our results indicate that the electronic excitation of the solid induced by the projectile impact decrease with increasing projectile nuclearity, a finding which reveals an opposite trend to that observed for the sputter yields. This surprising result cannot be understood in

terms of published theory and has therefore motivated an ongoing study in our group to model excitation and ionization processes in the frame of a molecular dynamics computer simulation of sputtering process.

Literature references

[An73] H.H. Andresen and H.L. Bay: *Sputtering-Yield Studies on Silicon and Silver Targets*. Rad. Eff. 19, 139 (1973)

[An74] H.H. Andersen and H.L. Bay: *Nonlinear Effects in Heavy-Ion Sputtering*. J.Appl. Phys. 45, 953 (1974)

[An75] H.H. Andersen and H.L. Bay: *Heavy-Ion Sputtering Yields on Gold: Futher evidence of Nonlinear Effects*. J.Appl.Phys. 46, 2416 (1975)

[An81] H.H. Andersen and H.L. Bay : *Sputtering by Ion Bombardment*. I. ed. R. Behrish (Springer Berlin) 145, (1981)

[An87] H.H. Andersen: *Computer Simulations of Atomic Collisions in Solids with Special Emphasis on Sputtering*. Nucl. Instr. Meth. B18, 321 (1987)

[Ay69] A.K. Ayukhanov and M.K. Abdullaeva, Izv. AN Zu SSR, Ser. Phys. Mat. Nauk. 4,60, (1969)

[Be76] F. Bernhardt, H. Oechsner, E. Stumpe, Nucl. Instr. Meth. 132 (1976)

[Be81] Topics in Applied Physics, Vol. 47, *Sputtering by Particle Bombardment I*, Editor: R.Behrisch, Springer-Verlag Berlin, (1981)

[Be84] C.H. Becker and K.T.Gillen: *Surface Analysis by Nonresonant Multiphoton Ionization of Desorbed or Sputtered Species*. Anal. Chem. 56, 1671 (1984)

[Be87] M. Bernheim, F. Le Bourse: *On the Velocity Dependence For Negative Ionization of Atoms From Cesiated Surfaces: An Experimantal Study*, Nucl. Instr. Meth. B27, 94-103, (1987)

[Be91] Topics in Applied Physics, Vol. 64, *Sputtering by Particle Bombardment II*, Editors: R. Behrish and K. Witmaack, Springer Verlag Berlin, (1991)

[Be92] S. F. Belykh, R. N. Evtukhov, Ju. N. Lysenko, and U. Kh. Rasulev: Negative metal ion and cluster source, Rev. Sci. Instr. 63, 4, (1992)

[Be98a] S.F. Belykh, U.Kh. Rasulev, A.V.Samartsev, S.V. Verkhoturov, and I.V. Veriovkin, Mikrochim. Acta 15 379 (1998).

[Be98b] S.F. Belykh, U.Kh. Rasulev, A.V. Samartsev, I.V. Veriovkin, Nucl. Instrum. Methods Phys. Res. B 136-138, 773 (1998)

[Be98c] Y. Le Beyec: *Cluster Impact at keV and MeV energies: Secondary Emission Phenomena*, Int. J. of Mass Spect. And Ion Processes, 174 (1998)

[Be99a] D. Stapel, M. Thieman, B. Hagenhoff, A. Benninghoven: *Secondary Ion Emission From LB-Layers Under Molecular Primary Ion Bombardment*, Proceedings of the 12th International Conference on Secondary Ion Mass Spectrometry, Brussels, Belgium, 5-11 September 1999.

[Be99b] A. Benninghoven, D. Stapel, O. Brox, B. Burkhardt, C. Crone, M. Thiemann, H.A. Arlinghaus: *Static SIMS With Molecular Primary Ions*, Proceedings of the 12th International Conference on Secondary Ion Mass Spectrometry, Brussels, Belgium, 5-11 September 1999.

[Be00] S.F. Belykh, B . Habets ,U.Kh. Rasulev, A.V. Samartsev, L.V. Stroev and I.V. Veriovkin: *Relative yields, mass distributions and energy spectra of cluster ions sputtered from niobium under keV atomic and polyatomic gold ion bombardment*, Nucl. Instrum. Meth. B 164-165, 809 (2000)

[Be01a] S.F. Belykh, V.V. Palitsin, A.P. Kovarsky, A.V. Zinoviev, A. Adriaens, *The development and the use of sputter cluster ion source for SIMS analysis*, Book

of abstracts on 14th Annual SIMS Workshop, May 13-16, Scottsdale, Arizona, p. 29-31, (2001)

[Be01b] 1. S.F. Belykh, I.A. Wojciehwski, V.V. Palitsin, A.V. Zinoviev, A. Adriaens and F. Adams: *Effect of the electronic subsystem excitation on the ionisation probability of atoms sputtered from metals by atomic and molecular projectiles*, Surf. Sci., 488 (2001) 141.

[Be02] S.F.Belykh, V.V.Palitsin, A.Adriaens, F. Adams: *Effect of the projectile parameters on the charge state formation of sputtered atoms*, Phys. Rev. B 66 (2002) 195309.

[Be03a] S.F.Belykh, V.V.Palitsin, A.Adriaens, F. Adams: *Effect of the projectile parameters on the charge state formation process in solid sputtering*, Appl. Surf. Sci. 203-204C (2003) 119.

[Be03b] S.F.Belykh, V.V.Palitsin, A.Adriaens, F. Adams: *Efect of the relaxation of the electron excitation in metals on the ionization probability of sputtered atoms*, NIM B (2003), in press.

[Bi78] I.S. Bitensky and E.S. Parilis, Sov. Phys. Tech. Phys. 23 (1978) 1104

[Bi87] I.S. Bitensky and E.S. Parilis, Nucl. Instr. Meth. Phys. Res. B 21 26 (1987)

[Bi80] I.S. Bitensky and E.S. Parilis, in: Proc. Symp. On Sputtering, Eds. P. Varga, G.Betz and F.P. Viehböck (TU Wien, Vienna, 1980) p. 688.

[Bl68] G. Blaise and G. Slodzian: C. R. Acad. Sci. B 266, 1525 (1968)

[Bl76] A. Blandin, A. Nourtier; D.W. Hone: *Localized time-dependent perturbations in metals*. *Formalism and simple examples*, J. Phys. 37, 4, (1976)

[Br89] R.A. Brizzolara, C.B. Cooper, Nucl. Instr. Meth. B 43 (1989)

[Ch92] V.T. Cherepin: *Ionniy Zond*, Kiev, Izdatelstvo "Naukova Dumka", (1992)

[Cl80] P. Sigmund and C. Clausen: *Sputtering from elastic-collision spikes in heavy-ion-bombrdment metals*. J. Appl. Phys. 52, (1980)

[Cl81] P.Sigmund, and C. Clausen: L. Appl. Phys. 52, 990, (1981)

[Co91] S.R. Coon, W.F. Calaway, J.W. Burnet, M.J. Pellin, D.M. Gruen, D.R. Spiegel and J.M. White: *Yields and Kinetic Energy Distributions of Sputtered Neutral Copper Clusters*. Surf. Sci. 259, 275 (1991)

[Co93] S.R. Coon, W.F. Calaway, M.J. Pellin, and J.M. White: *New findings on the Sputtering of Neutral Metal Clusters*. Surf. Sci. 298, 161 (1993)

[Co94] S.R. Coon, W.F. Calaway and M.J. Pellin: *Neutral Copper Cluster Sputtering Yields: Ne^+, Ar^+ and Xe^+ Bombardment*. Nucl. Instr. Meth. B90, 518 (1994)

[Cr99] C. Crone, R. Ostendorf, M.Thiemann, H.F. Arlinghaus, and A. Benninghoven : *Static Sims of Matrix Isolated Molecules under Polyatomic Primary Ion Bombardment. Proceedings of the 12th International Conference on Secondary Ion Mass Spectrometry*, Brussels, Belgium, (1999).

[Cy68] F. Cyrot-Lackmann: J.Phys. Chem. Solids 29, 6443 (1968)

[Da84] M.S. Daw and M.I. Baskes, 1984: Phys. Rev. 29, 6443, (1984)

[De89] A.D. Appelhans, J.C. Ingram, J.E. Delmore: *Comparison of polyatomic and atomic primary beams for secondary ion mass spectrometry of organics*, Analytical Chemistry 61(10), (1989).

[[Dz87] N.Kh. Dzemilev, S.V. Verkhoturov, U. Kh. Rasulev: *The fragmentation of sputtered cluster ions and their contribution to secondary ion mass spectra*. Nucl. Instrum. Methods B, 29, 531-536, (1987).

[Dz96a] N. Kh. Dzhemilev, A. M. Goldenberg, I. V. Veriovkin**,** and S. V. Verkhoturov: *Fragmentation of Cluster Ions in SIMS: Cluster distributions over Lifetime, Excitation Energy and Kinetic Energy Release*. Nucl.Instr.and Meth.B, 1996, V.114. P.245-251

[Dz96b] A. D. Bekkerman, N. Kh. Dzhemilev, S. E. Maksimov, V. V. Solomko, S. V. Verkhoturov, and I. V. Veryovkin, *C_n and Cs $_mC_n$ Clusters Sputtered from Fullerite Compared With Those for Graphite*, Vacuum, 1996, V.47, №9, P.1073-1075

[Dz96c] A. D. Bekkerman, N. Kh. Dzhemilev, S. V. Verkhoturov, and I. V. Veryovkin : *The Unimolecular Decays of Al_n^+ and Cu $_n^+$ Sputtered Clusters: a Comparison Between Competitive Decay Modes*, Vacuum, 1996, V.47, №5, P.405-407 A.

[Dz96d] D. Bekkerman, I. V. Veryovkin, S. V. Verkhoturov, O. V. Guliamova, N. Kh. Dzhemilev, S. E. Maksimov, and V. V. Solomko: *Fullerite Sputtering by Cesium Ions: Experiment and Model Concepts*. Izv.Akad.Nauk ser.fiz., 1996, V.60, №7, P.121-127. (In Russian) and Bull.Russ.Acad.Sci.-Physics, 1996, V.60, №7, P.1112-1116 (English translation)

[Dz97] A. D. Bekkerman, N. Kh. Dzhemilev, S. V. Verkhoturov, and I. V. Veryovkin: *The fragmentation of excited sputtered clusters: the kinetic energy release distributions of Al and Cu cluster ions sputtered by Xe^+ and Cs^+ ions*, in: "Secondary Ion Mass Spectrometry. SIMS X. Proceedings of the 10-th International Conference", 1997, John Wiley & Sons, - P.403-406

[Do61] E.Dörnenburg, H.Hintenberger, J.Franzen: Z.Naturforsch. 16a, 532 (1961)

[Du04a] A. Duvenbeck, M. Lindenblatt, and A. Wucher: *Self Sputtering Yields of Silver under Bombardment with polyatomic Projectiles*, in press.

[Du04b] A. Duvenbeck, Z. Sroubek and A. Wucher: *Electronic Excitation in Atomic Collisions Cascades,* Conference Proceeding OF the COSIRES Helsinki (2004)

[En83] W. Ens, R. Beavis, and K. G. Standing: *Time-of-Flight Measurements of Cesium-Iodide Cluster Ions*, Phys. Rev. Lett. 50, 27–30 (1983)

[Ge75] W. Gerhard, Z. Phys. B 22 31 (1975)

[Gi00] G. Gillen, L. King, B. Freibaum, R. Lareau and J. Bennet*: A Negative Cesium Sputter Ion Source for Generating Cluster Primary Ion Beams For SIMS Analisys*, Proc. Of the 12th Intern. Conference on SIMS, Brussels, Belgium

[Gn89] H.Gnaser and W.O.Hofer: *The Emission of Neutral Clusters in Sputtering*, Appl.Phys A48, 261 (1989)

[Gn93] H. Gnasser: *Low-Energy Ion Irradiation of Solid Surfaces,* Springer-Verlag Berlin Heidenberg New York, (1993)

[Ha42] Hahn O, Strassmann F, Mattauch J and Ewald H: Naturwissenshaften 30, 541 (1942).

[Ha81] D.E. Harrison Jr.: J.Appl. Phys. 52, 1499, (1981)

[Ha84] R.A. Haring, R. Pedrys, A. Haring and A.E. de Vries, Nucl. Instrum. Methods B, 4 (1984)

[Ha85] R.A. Haring, R. Pedrys, A. Haring and A.E. de Vries, Nucl. Instrum. Methods B, 6 (1985)

[He96] R. Heinrich, A. Wucher : *Untersuchung zur Bildung zerstaubter Germanium-Cluster,* Diplomarbeit, Universitaet Kaiserslautern (1998)

[He98] R. Heinrich, A. Wucher: *Yields and Energy Distributions of Sputtered Semiconductor Clusters,* Nucl. Instr. Meth. B 140, 27 (1998)

[He99] R.Heinrich, C.Staudt, M.Wahl and A.Wucher: *Ionization Probability of Sputtered Clusters,* Proceedings of the 12th International Conference on Secondary Ion Mass Spectrometry (SIMS XII), Louvrain-la-Neuve, Belgium, 1999

[He00] R. Heinrich, A. Wucher: *Cluster Formation Under Bombardment with Polyatomic Projectiles,* Nucl. Instr. and Meth. B 164-165 (2000) 720-726

[He02] R. Heinrich, A. Wucher: *Self-sputtering of Silver Using Polyatomic Projectiles*, Nucl. Instr. and Meth. B 193 (2002) 781-786
[Ho53] R.E. Honig: J. Chem. Phys. 21, 573 (1953)
[Ho58] R.E. Honig: J. Appl. Phys. 29,549 (1958)
[Ho69] G. Hortig and M. Mueller: Z. Phys. D22, 517 (1992)
[Ka86] I.Katakuse, T. Ichinara, Y.Fujita, T.Matsuo, T.Sakurai, H.Matsuda: Int. J. Mass Spectrom. Ion Proc. 67, 229 (1985); 69, 109 (1986)
[Ke84] R. Kelly: *The Varieties of Surface Alteration: Structural, Topographical, Electronic and Compositional* // Ion bombardment modification of the surfaces. – Amsterdam :Elsevier, 1984. – 468 p.
[Ke90] R. Kelly: *Thermal Sputtering As A Gas-Dynamic Process*, Nucl. Instrum. Methods B, 46, (1990)
[Ko02] V.Kohlschütter: Verh. Dtch. Phys. Ges. 4, 228 and 237 (1902)
[Ko94] D. Koch: *Anwendung eines VUV-Lasers zur Nachionisation gesputterter Neutralteilchen*, Diplomarbeit, Universitaet Kaiserslautern (1994)
[Kr62] V.E. Krohn: *Emission of Negative Ions from Metal Surfaces Bombarded by Positive Cesium Ions* ,J. Appl. Phys. 33, 3523 (1962)
[Ki81] Y.Kitazoe, N.Hiraoka and Y.Yamamura, Surf. Sci. 111 (1981) 381
[Kr62] V.E. Krohn: J. Appl. Phys. 33, 3523 (1962)
[Ku93] M.Kumada, Y.Iwashiba, M.Aoki, E. Sugiyama : *The Strongest Permanent Dipole Magnet,* Proceedings of the 2003 Particle Accelerator Conference. (1993)
[La33] J.B. Taylor, and I. Langmuir, Phys. Rev. 44. No. 6. p. 423, (1933)
[La83] N. D. Lang: *Ionization probability of sputtered atoms*, Phys. Rev. B 27, 2019–2029 (1983)
[Le89a] M. G. Blain, S. Della–Negra, H. Joret, Y. Le Beyec, and E. A. Schweikert: *Secondary-ion yields from surfaces bombarded with keV molecular and cluster ions,* Phys. Rev. Lett. 63, 1625–1628 (1989)
[Le89b] M. G. Blain, S. Della–Negra, H. Joret, Y. Le Beyec, and E. A. Schweikert: *Secondary-Ion Yields from Surfaces Bombarded with keV Molecular and Cluster Ions*, Phys. Rev. Lett. 63, 1625–1628 (1989)
[Le91] M. Benguerba, A. Brunelle, S. Della-Negra, J. Depauw, H. Joret, Y. Le Beyec, M. G. Blain, E. A. Schweikert, G. Ben Assayag and P. Sudraud: *Impact of slow gold clusters on various solids: nonlinear effects in secondary ion emission*, Nucl. Instrum. Methods B, 61, 1 (1991)
[Le98a] 3831. Le Beyec: *Cluster Impacts at keV and MeV Energies: Secondary Emission Phenomena,* - Orsay,- 22p.;13p.il. (IPNO-DRE 97-32), (1997)
[Le98b] H. H. Andersen, A. Brunelle, S. Della-Negra, J. Depauw, D. Jacquet, and Y. Le Beyec: *Giant Metal Sputtering Yields Induced by 20–5000 keV/atom Gold Clusters*, Phys. Rev. Lett. 80, 5433–5436 (1998)
[Le99] Y. Le Beyec, K. Baudin, A. Brunelle, S. Della-Negra, D. Jackuet, M. Pautrat: *Desorption and Sputtering from Solids Induced by Polyatomic Projectiles*, Brazilian Journal of Physics, 29, 3, (1999)
[Li83] S.H.Lin, I.S.T. Tsong, A.R. Ziv, M. Szymonski and C.M. Loxton, Phys. Scr. T6 (1083) 106.
[Li01] M. Lindeblatt, R. Heinrich, and A. Wucher: *Self-Sputtering of Silver by a Mono- and Polyatomic projectiles: A Molecular Dynamic Investigation*, Journal of Chemical Physics, 115, 18, (2001)
[Lu78] B.T. Lundvist, Y.K. Norskov: *Secondary ion emission probability in sputtering*, Phys. Rev. B. – 19 , 11, (1978)
[Ma43] J.Matauch, H. Ewald, O. Hahn and Strassmann F: Z.Phys. 120, 598 (1943)

[Mi73] R. Middleton: *The UNIS Ion Source*, SNEAP, Brookhaven National Laboratory, Upton, N.Y., U.S.A. September 12-14, (1973)
[Mi77] R. Middleton, Nucl. Instr. and Meth. 144 373-399 (1977)
[Mi83] R. Middleton, Nucl. Instrum. Methods, 214, 139 (1983)
[Mi83a] J. Michl, Int. J. Mass Spec. Ion Phys. 53, 255, (1983)
[Mi86] D.E. David, T.F. Magnera, R. Tian and J. Michl, Radiat. Eff. 99, 247 (1986)
[Mi86] D.E. David, T.F. Magnera, R. Tian, D. Stulik and J. Michl, Nucl. Instr. and Meth. B14, 378 (1986)
[Mo03] Sh.Akhunov, S.N. Morozov, U.Kh. Rasulev : *Features of polyatomic ion emission under sputtering of a silicon single crystal by Au_m^- cluster ions*, pp. 146-150 (2003).
[Mu97] S.F. Belykh, I.S. Bitensky, D.Mullajanov, U.Kh. Rasulev: *Nonlinear effects in cluster emission from solids induced by molecular ion impact*, Nucl. Instrum. Methods B, 129, 4, (1997).
[N078] J.K. Norskov, B.I. Lundqvist: *Secondary-ion emission probability in sputtering*, Phys. Rev. B , 19, 11, (1978)
[No87] A. Nortier*: Expression of the ionization probability for sputtering from a metal with an arbitrary electronic structure*, Surface Sci. – 191, ½, (1987)
[Oe74] H. Oechsner and W. Gerhard: *Mass Spectroscopy of Sputtered Neutrals and its Application for Surface Analysis,* Surf. Sci. 44, 480 (1974)
[Oe90] K. Franzreb, A. Wucher and H.Oechsner*: Electron Impact Ionization of Small Silver and Copper Clusters*, Z. Phys. D, 17, (1990)
[Pe03] B.V. King, M.J. Pellin, J.F. Moore, I.V. Veryovkin, M.R. Savina and C.E. Tripa: *Estimation of Useful Yield in Surface Analysis Using Single Photon Ionization*, Appl. Surf. Sci. 203-204, (2003)
[Oe75] W. Gerhard and H. Oechsner : Z. Phys. A48, 261 (1975)
[Oe78] H. Oechsner, H. Schoof and E. Stumpe: *Sputtering of Ta_2O_5 by Ar^+ Ions at Energies below 1 keV,* Surf. Sci. 76, 343 (1978)
[Pa88] J.B. Pallix, K.T. Gillen, and C.H.Becker: *Surface And Interface Analisys by Nonresonant Multiphoton Ionization of Sputtered Neutrals,* Nucl. Instr. Meth. B33, 912 (1988)
[Pe93] Z. Ma, S.R. Coon, W.F. Calaway, M.J. Pellin, D.M.Gruen, and E.I. von Nagy-Felsobuki: *Sputtering Neutral and Ionic Indium Clusters,* J.Vac. Sci. Technol. A12(4), Jul/Aug (1994)
[Jo71] P.Joyes, J.Phys. B4 (1971) L15.
[Jo79] S.S. Johar and D.A. Thompson: *Spike Effects in Heavy-Ion Sputtering of Ag, Au and Pt Thin Films,* Surf. Sci. 90, 319 (1979)
[Ra85] J. Wayne Rabalais and Jie-Nan Chen: *Inelastic Processes in Ion/Surface Collisions: Direct Recoil Ion Fractions as a Function of Kinetic Energy*, J. of Chem. Phys. 85, 3612-3622, (1986)
[Sa00] S.F. Belykh, U.Kh. Rasulev, A.V. Samartsev, L.V. Stroev and A.V.Zinoviev: *High non-additive sputtering of silicon as large positive cluster ions under polyatomic ion bombardment*, Vacuum 56, 4, (2000).
[Si69] P.Sigmund : *Theory of sputtering. Sputtering yield of amorphous and polycrystalline targets*, Phys. Rev. 184 , N 2 , 383-416, (1969)
[Si75] P.Sigmund: *Energy Density and Time Constant of Heavy-Ion-Induced Elastic-Collision Spikes in Solids*, Phys. Lett. 27, 52 (1975)
[Si81] P.Sigmund, in: *Sputtering by Particle Bombardment I*, Ed. R. Behrisch, Vol. 47 of Topics in Applied Physics (Springer, Berlin, 1981) p. 9.
[Sn87] K.J. Snowdown and R.A. Haring, Nucl. Instr. Meth. Phys. Res. B 18 596 (1987)

[Sr82] Z. Sroubek: *Theory of Charge States in Sputtering*, Nucl. Instr. Meth. 194, (1982)
[Sr89a] Z. Sroubek: *Formation of Ions in Sputtering*, Spect. Acta, V 44, N 3, 317.328, (1989)
[Sr89b] G. Falcone, and Z. Sroubek: *Energy spectra of electronic excitations in collision cascades*, Rad.Eff., V. 109, 253-258, (1989)
[Sr99] Z. Sroubek, J. Loerinchik: *Ionization and Excitation Processes in Sputtering in the Light of the Experimental Evidence*, Surf. Rev. And Let., V.6, N 2 (1999)
[St77] H.A. Storms, K.F. Brown and J.D. Stein, Anal. Chem., 49, 2023 (1977)
[St93] H. Stolz, M. Hoefer and H.W. Wassmuth: *TPD, AES, $\Delta\varphi$ and LEED investigation of cesium adsorbed on Ag(100),* Surf. Sci. 287/288, 564-567, (1993)
[St02] C.Staudt and A. Wucher: *Generation of Large Indium Clusters by Sputtering,* Physical Review B 66, 075419 (2002)
[Sz78] M. Szymonski, R.S. Bhattacharya, H. Overeijnder and A.E. Vries: *Sputtering of an AgAu alloy by bombardment with 6 keV Xe^+ ions*, J. Phy. D: Appl. Phys., Vol. 11, (1978)
[Sz82] M.Szymonsky and A. Poradzisz: *A Model of Sputtering from Spikes*, Appl. Phys. A28, 175-178 (1982)#
[Th68] M.W. Thompson: *Random Cascade Sputtering Model*, Phil. Mag. 18 (1968)
[Th79] D.A. Thompson and S.S. Johar*: Nonlinear Sputtering Effects in Thin Metals Films,* Appl. Phys. Lett. 34, 342 (1979)
[Th80] D.A. Thompson and S.S. Johar: *Sputtering of Silver by Heavy Atomic and Molecular Ion Bombardment*, Nucl. Instr. Meth. 170, 281 (1980)
[Th81] D.A. Thompson: *High density cascade effects -invited review*, Rad. Effects 56, 105-150 (1981.).
[Ur87] H.M. Urbassek, Nucl. Instr. Meth. Phys. Res. B18 587 (1987)
[Ur87b] H.M. Urbassek and J. Michl: *A Gas-Flow Model For The Sputtering Of Condensed Gases*, Nucl. Instr. and Meth. B22, (1986)
[Ur88] H.M. Urbassek, Nucl. Instr. Meth. Phys. Res. B31 541 (1988)
[Ur89] H.M. Urbassek, Radiat. Eff. Def. Solids 109, 293, (1989)
[Ur95] D. Klushin, M. Gusev, I. Urazgil'din: *Velocity dependence of ionization probability of secondary ions emitted from metal surfaces,* Nucl. Instr. and Meth. B 100, 316 (1995).
[Ur96] H.M. Urbassek, T.J. Colla: *Effect of Energy Density on Cluster Formation From Energized Atoms*, Computational Material Science 6, (1996)
[Ur00] H.M. Urbassek, T.J. Colla, R.Aderjan and R. Kissel: *Sputtering of Au (111) Induced by 16-keV Au Cluster Bombardment: Spikes, Craters, Late Emission, And Fluctuations*, Phys. Rev, 62, 12 (2000)
[Wa95] M. Wahl: *Experimentelle Untersuchungen zur Zerstaeubung von Metall Clustern unter Vervendung der UV/VUV-Photoionization*. Dissertation, Universitaet Kaiserslautern (1995).
[Wi75] K. Wittmaack: *Energy dependence of the secondary ion yield of metals and semiconductors*, Surf. Sci., 53, 1, (1975)
[Wo64] J.R. Woodyard and C.B Cooper: J.Appl. Phys.35, 1107 (1964)
[Wu87a] A. Wucher, and H. Oechsner: *Energy Distributions of Metal Atoms and Monoxide Molecules Sputtered From Oxidized Ta and Nb,* Nucl. Instr. Meth. B 18 458-463 (1987)
[Wu87b] A. Wucher, H. Oechsner: *Energy Dependent Ionization probabilities For Atomic Secondary Ions*, Proceedings of the 6th International Conference on SIMS, (1987)

[Wu92a] A. Wucher, and B.J Garrison: Sputtering of Silver Dimers: *A Molecular Dynamics Calculation Using a Many-Body Embedded-atom Potential*, Surf. Sci. 260, 257, (1992)
[Wu92b] A. Wucher, and B.J. Garrison*: Unimolecular Decomposition in the Sputterinng of Metal Clusters*, Phys. Rev. B64, 4855, (1992)
[Wu93a] A. Wucher, M. Wahl, and Oechsner: *The Mass Distribution of Sputtered Metal Clusters I. Experiment,* Nucl. Instr. Meth. B 83, 73 (1993)
[Wu93c] A.Wucher, M Wahl and H. Oechsner: *Sputtered Neutral Silver Clusters up to* Ag_{18}. Nucl. Instr. Meth. B82, 337 (1993)
[Wu94a] M. Wahl, A. Wucher, Nucl. Instr. Meth. B 94 36 (1994)
[Wu94b] A. Wucher, Z. Ma, W.F. Calaway, M.J. Pellin, Surf. Sci. Lett. 304 L439 (1994)
[Wu95] A.Wucher, and M. Wahl: *Cluster Emission in Sputtering*. Proceedings of the Tenth International Conference on Secondary Ion Mass Spectrometry (SIMS X). (1995)
[Wu96] A. Wucher, M.Wahl : Nucl. Instr. Meth. B 115, 581-589 (1996)
[Wu99] A. Wucher, R.Heinrich, C. Staudt and M. Wahl: *Ionization Probability Of Sputtered Clusters*, Proceedings of the 12th International Conference on Secondary Ion Mass Spectrometry, Brussels, Belgium, (1999)
[Wu01] A. Wucher: *Laser Post.Ionization: Fundamentals. ToF-SIMS: Surface analisys by Mass Spectrometry*, edited by John C. Vickerman and David Briggs. (2001)
[Wu02b] A. Wucher: *Formation Of Clusters In Sputtering*, Izvestia Akademii Nauk, 66, 4, (2002)
[Vi76] G.H. Vineyard, Rad. Eff. 29, 245 (1976)
[Yo87] C.E. Young, M.J. Pellin, W.F. Calaway, B. Jorgesen, E.L. Schweitzer and D.M. Gruen: *Laser-Based Secondary Neutral Mass Spectroscopy: Useful Yield and Sensitivity,* Nucl. Instr. Meth. B27, 119 (1987)
[Yu78] M. L. Yu : *Work-Function Dependence of Negative-Ion Production during Sputtering*, Phys. Rev. Lett. 40, 574-577 (1978)
[Yu79] M. L. Yu: *Observation of positive and negative oxygen ions during electron bombardment of oxygen-covered Mo (100) surfaces*, Phys. Rev. B 19, 5995-6000 (1979)
[Yu81] M. L. Yu: *Velocity Dependence of the Ionization Probability of Sputtered Atoms*, Phys. Rev. Lett. 47, 1325-1328 (1981)
[Yu82] M. L. Yu: *Matrix effects in the work-function dependence of negative-secondary-ion emission*, Phys. Rev. B 26, 4731-4734 (1982)

Acknowledgements

I am very grateful to Prof. Dr. A. Wucher for the invitation in the laboratory with the possibility to perform current study with interesting theme. Also, for stimulating discussions, and leading hints.
Special thanks to Prof. Dr. Marika Schleberger for evaluation of the current thesis.
I, also, would like to thank Herr W. Saure for his development of electronic power supplies for the ion source.
I would like to express my gratitude to the working group of laboratory for enthusiastic and friendly atmosphere during all the time of the project.